U.S. DEPARTMENT OF COMMERCE
National Technical Information Service

AD-A026 479

RCS (RADAR CROSS-SECTION) OF A FINITE LENGTH PERFECTLY-CONDUCTING CYLINDER ON A PLANAR, UNIFORM IMPEDANCE SURFACE

OHIO STATE UNIVERSITY

PREPARED FOR

NAVAL REGIONAL PROCUREMENT OFFICE

DECEMBER 1975

RCS OF A FINITE LENGTH, PERFECTLY-CONDUCTING CIRCULAR CYLINDER ON A PLANAR, UNIFORM IMPEDANCE SURFACE

P. H. Pathak

The Ohio State University
ElectroScience Laboratory
Department of Electrical Engineering
Columbus, Ohio 43212

TECHNICAL REPORT 4111-2

December 1975

Contract N00140-75-C-6116

Naval Regional Procurement Office
Philadelphia, Newport Division Building No. 132
Newport, Rhode Island 02840

NOTICES

When Government drawings, specifications, or other data are used for any purpose other than in connection with a definitely related Government procurement operation, the United States Government thereby incurs no responsibility nor any obligation whatsoever, and the fact that the Government may have formulated, furnished, or in any way supplied the said drawings, specifications, or other data, is not to be regarded by implication or otherwise as in any manner licensing the holder or any other person or corporation, or conveying any rights or permission to manufacture, use, or sell any patented invention that may in any way be related thereto.

UNCLASSIFIED

SECURITY CLASSIFICATION OF THIS PAGE (When Data Entered)

REPORT DOCUMENTATION PAGE

READ INSTRUCTIONS BEFORE COMPLETING FORM

1. REPORT NUMBER	2. GOVT ACCESSION NO.	3. RECIPIENT'S CATALOG NUMBER
4. TITLE (and Subtitle) RCS OF A FINITE LENGTH, PERFECTLY-CONDUCTING CYLINDER ON A PLANAR, UNIFORM IMPEDANCE SURFACE		5. TYPE OF REPORT & PERIOD COVERED Technical Report
		6. PERFORMING ORG. REPORT NUMBER ESL 4111-2
7. AUTHOR(s) P. H. Pathak		8. CONTRACT OR GRANT NUMBER(s) N00140-75-C-6116
9. PERFORMING ORGANIZATION NAME AND ADDRESS The Ohio State University ElectroScience Laboratory, Department of Electrical Engineering Columbus, Ohio 43212		10. PROGRAM ELEMENT, PROJECT, TASK AREA & WORK UNIT NUMBERS
11. CONTROLLING OFFICE NAME AND ADDRESS Naval Regional Procurement Office Philadelphia, Newport Division Building No. 132 Newport, Rhode Island 02840		12. REPORT DATE December 1975
		13. NUMBER OF PAGES 77
14. MONITORING AGENCY NAME & ADDRESS(if different from Controlling Office)		15. SECURITY CLASS. (of this report) UNCLASSIFIED
		15a. DECLASSIFICATION DOWNGRADING SCHEDULE

16. DISTRIBUTION STATEMENT (of this Report)

DISTRIBUTION STATEMENT A

Approved for public release;
Distribution Unlimited

17. DISTRIBUTION STATEMENT (of the abstract entered in Block 20, if different from Report)

18. SUPPLEMENTARY NOTES

19. KEY WORDS (Continue on reverse side if necessary and identify by block number)

Radar cross section
Finite cylinder
Impedance surface
Geometrical theory of diffraction

20. ABSTRACT (Continue on reverse side if necessary and identify by block number)

The radar cross-section (RCS) of a finite length, perfectly-conducting circular cylinder on a uniform impedance surface is calculated via the geometrical theory of diffraction (GTD). The cylinder is oriented such that its axis is normal to the surface impedance plane. It is found that the effect of the surface impedance is, in general, to enhance the RCS over that without the surface impedance. Both these calculations are presented for comparison. The RCS is, of course, dependent on the angle of incidence, polarization and the frequency of the incident wave; these effects are also investigated.

DD FORM 1 JAN 73 1473 EDITION OF 1 NOV 65 IS OBSOLETE

UNCLASSIFIED

SECURITY CLASSIFICATION OF THIS PAGE (When Data Entered)

CONTENTS

I. INTRODUCTION

The far-field plane wave backscattering cross-section, or the radar cross-section (RCS) of a finite length, perfectly-conducting, solid, circular cylinder on a planar, uniform impedance surface of infinite extent is investigated in this report. The cylinder is oriented such that its axis is perpendicular to the impedance surface as shown in Fig. 1. An impedance surface at z=0 implies that the total electromagnetic field must satisfy the impedance boundary condition [1] there. The region corresponding to $z>0$ is free space, and the value of the surface impedance, Z_s at z=0, is taken to be a known complex function of the frequency of the incident plane wave.

In the present study, we are primarily interested in calculating the RCS of the cylinder in Fig. 1 for the range of aspects corresponding to $25°<\theta^i<88°$. It is assumed that the length, ℓ, of the cylinder is larger than its radius, a, and that ka is at least a wavelength or more; here k is the free space wave number ($k = \frac{2\pi}{\lambda}$, λ = wavelength). The method of analysis employed in this report for calculating the RCS is based on the geometrical theory of diffraction (GTD) [2]. Although the GTD is an asymptotic high frequency ray technique, it is known to be extremely accurate even for moderately high frequencies. Details of the GTD analysis for estimating the RCS are presented in Section II.

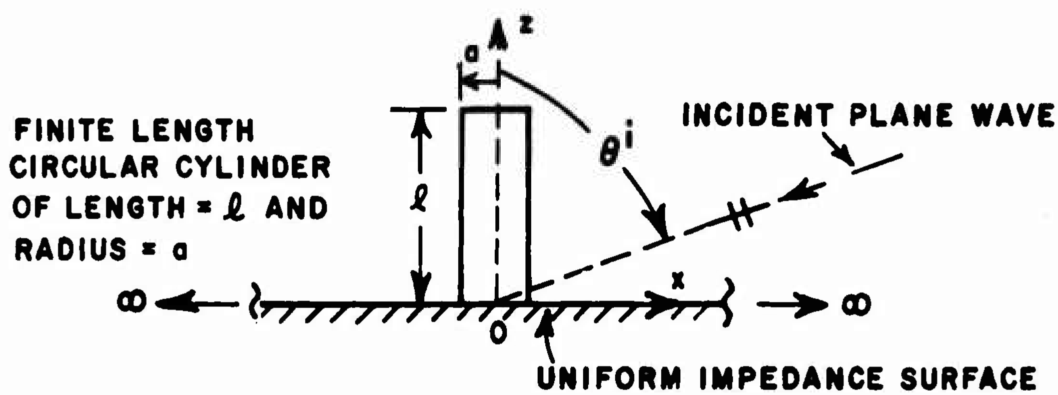

Fig. 1. Finite circular cylinder on an impedance surface.

Numerical results are presented in Section III, wherein the RCS of the cylinder in the presence of the impedance surface is compared with the RCS of an identical diameter cylinder in free space without the impedance surface; the length of the cylinder in free space is selected to be twice that of the cylinder on the impedance surface. The RCS of the cylinder in the presence of Z_s is much higher than that of the cylinder in free space. Also, the RCS increases rapidly with increase in frequency. In particular, numerical results for the RCS are presented as a function of the aspect $\theta^i (25° < \theta^i < 88°)$ for two types of polarization, and for a given set of frequencies. The two types of polarization correspond to the case when the incident electric field vector lies either in the plane of incidence or perpendicular to the plane of incidence, respectively. The former is commonly referred to as the parallel polarization case, whereas the latter is commonly referred to as the perpendicular polarization case. In the absence of Z_S, the RCS of the finite cylinder in free space is generally higher for the parallel polarization than for the perpendicular polarization case; in the presence of Z_S, the cylinder RCS for both polarizations is generally of comparable magnitude. In particular, the RCS of the cylinder on Z_S is very much governed by the reflection coefficient associated with the surface impedance Z_S. The behavior of the reflection coefficient associated with Z_S is illustrated in Section II over the range $25° < \theta^i < 88°$, for the selected frequencies of interest. A discussion on the behavior of the RCS of cylinders with and without Z_S is given in Section III. The RCS in the vicinity of end fire ($\theta^i \to 0$) is not presented as it is not of interest in the present study. The end fire RCS may, however, be readily estimated to a high degree of accuracy via the physical optics approximation [4].

II. ANALYSIS

As mentioned earlier, the polarization of the incident plane wave is assumed to be either in the plane of incidence or perpendicular to the plane of incidence. When the incident electric field vector lies in the plane of incidence (x-z plane), we will define this to correspond to the acoustic hard case (with respect to the edges Q_1 and Q_2 of the cylinder in the x-z plane); whereas, we will define the other polarization to correspond to the acoustic soft case (with respect to the edges Q_1 and Q_2). The acoustic hard case may also be viewed as one for which the incident magnetic field is polarized perpendicular to the plane of incidence. Let $U^i_{\substack{s\\h}}$ denote the incident field.*

$$(1) \qquad U^i_{\substack{s\\h}}(x,z) = A_{\substack{s\\h}}\, e^{i[kx \sin\theta^i + kz\cos\theta^i]} \quad .$$

The subscripts s and h refer to the acoustic soft and hard cases, respectively. Thus, U_s denotes a $\hat{y}$-directed electric field; whereas U_h denotes a $\hat{y}$-directed magnetic field. The superscript i refers to incident field quantities. $A_{\substack{s\\h}}$ stands for the known constant complex amplitude of the soft and hard type incident fields. For large ka, the dominant contributions to the backscattered field are those resulting

*An $e^{i\omega t}$ time dependence is assumed and suppressed throughout the analysis.

from the process of double-reflections, edge diffraction, and from the first few interactions between the edge diffracted fields and the surface at z=0. The contribution to the backscattered field from surface rays which propagate around the cylinder is negligible for large ka; these rays have been excluded in the present analysis. In the present case, the edge diffracted rays are produced via the diffraction of the incident plane wave by the circular rim of the end cap of the cylinder at $z=\ell$. The specific double reflections, single edge diffractions, and the orders of edge diffraction-surface reflection interactions which have been retained in the present analysis are illustrated via the pertinent rays that are associated with these interactions in Figs. 2(a), 2(b), 2(c), and 2(d), respectively. With no loss of generality, the RCS is calculated in the x-z plane for convenience; thus, the rays depicted in Fig. 2 must also lie in the x-z plane. Figure 2(a) indicates the doubly reflected rays which contribute to backscatter; these rays are analogous to those present in the corner reflector problem. Q_A and Q_B denote the points of reflection on the cylinder and the impedance surface, respectively. The incident ray at Q_A reflects energy along the ray path Q_AQ_B such that the second reflection at Q_B generates a reflected ray in the backscatter direction, and vice versa. Consequently, Fig. 2(a) illustrates the existence of two reciprocal (doubly reflected) ray systems; actually, there exist a doubly infinite set of the doubly reflected ray fields (corresponding to these two reciprocal ray systems) which contribute to the backscatter, because every point along the cylinder ($x=a$; $y=0$; $0<z<\ell$) constitutes a point of reflection. Figure 2(b) indicates the interaction between singly edge diffracted rays and the surface at z=0. In particular, the incident ray at the edge Q_1 produces a diffracted ray which strikes the impedance surface at Q_R to produce a reflected ray in the backscatter direction, and vice versa. Thus, Fig. 2(b) also describes two reciprocal ray systems, each of which yields identical field contributions in the backscatter direction via the reciprocity theorem for electromagnetic fields. One must include the effects of both reciprocal ray systems in Fig. 2(b) for evaluating the backscattered field, and since the fields associated with each of these reciprocal ray systems is identical in the far zone, the total far zone backscattered field corresponding to only these interactions is simply twice that given by either of the two reciprocal ray interactions. The field contributions corresponding to Figs. 2(a) and 2(b) are analyzed here by first picking a field (or observation) point in the near zone (so that the doubly reflected, the diffracted-reflected, and the reflected-diffracted fields propagate along slightly non-parallel or convergent ray paths to the field point), and by then taking the limit of this near field quantity as the field point recedes to infinity (or far zone); the limit now gives the backscattered field corresponding to Figs. 2(a) and 2(b). In the near zone, only one doubly reflected ray of Fig. 2(a) contributes to the field there; this simplifies the analysis. Figure 2(c) indicates the incident rays which strike the cylinder edges at Q_1 and Q_2 to produce singly edge diffracted rays which emanate from Q_1 and Q_2.

Multiple edge diffraction effects between Q_1 and Q_2 are neglected; these multiple interactions may be excluded for large ka. For moderately large values of ka, these interactions are still quite small in comparison with the singly diffracted fields. Finally, Fig. 2(d) illustrates the ray system in which the incident field at Q_R illuminates the edge Q_1 via reflection from Q_R; this in turn produces a diffracted ray from Q_1 which strikes the surface at Q_R to produce a reflected ray in the backscatter direction.

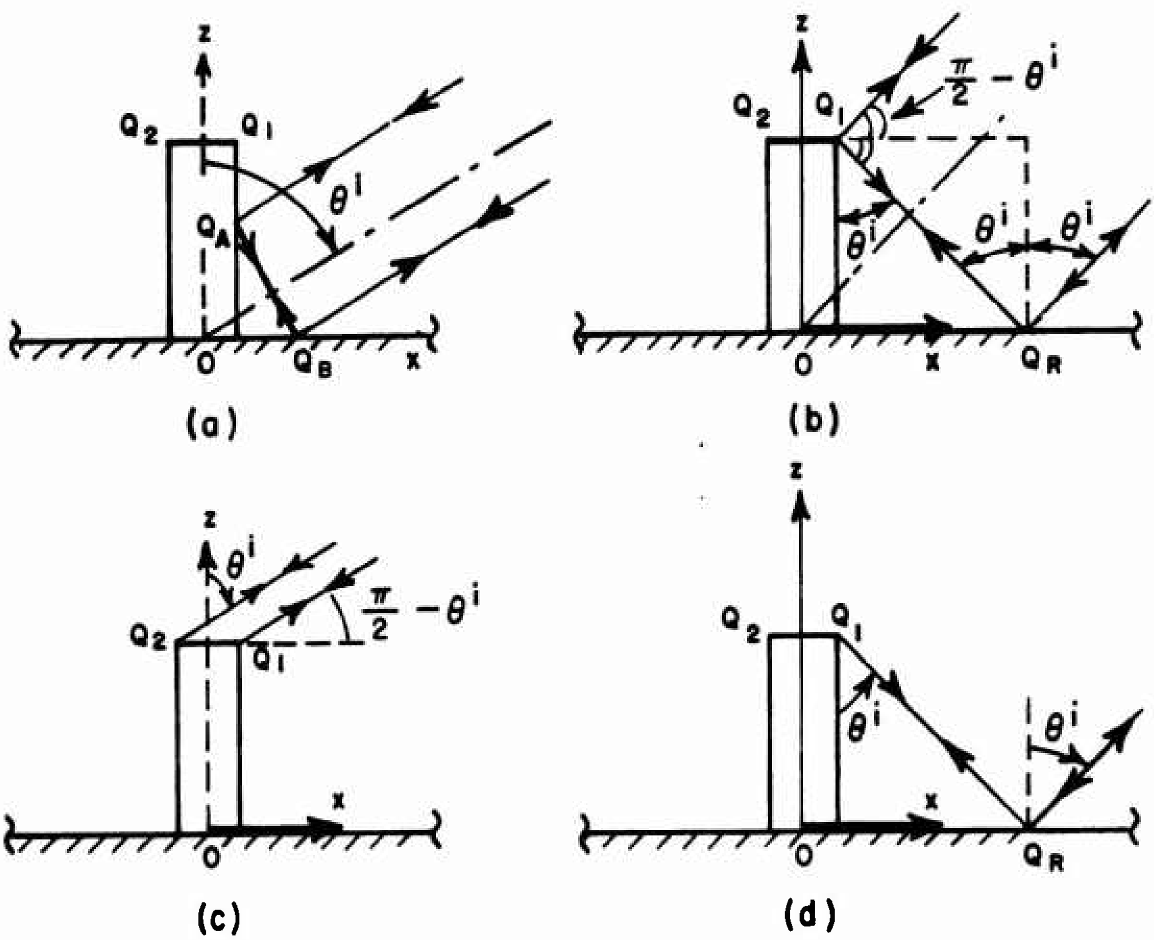

Fig. 2. Dominant rays for far-zone backscatter calculations.

The new uniform GTD curved edge diffraction coefficient of Kouyoumjian and Pathak [3] is employed to calculate the edge diffractions at Q_1 and Q_2. On the other hand, the Fresnel reflection coefficients associated with the impedance boundary at z=0 are employed to calculate the reflection at Q_R and Q_B. The reflection from Q_A on on the cylinder is calculated as usual in terms of the reflection coefficient for a perfectly-conducting flat surface which is locally tangent to the cylinder at Q_A. It is noted from Fig. 2(a) that $Q_A \to Q_1$ and $Q_B \to Q_R$ as the double reflection shadow boundaries are approached. Consequently, the edge diffraction-surface reflection interactions of Fig. 2(b) take place along the double reflection shadow boundaries in the far zone. In the far zone, the unshadowed region where double reflections are present shrinks to a thin line (dot-dashed reference line). As mentioned earlier, this far zone result (i.e., backscattered field corresponding to Figs. 2(a) and 2(b)) is obtained via a careful limiting operation on the corresponding near field quantity.

We will first analyze the interactions in Figs. 2(c) and 2(d) in a straightforward manner. The slightly more complicated analysis of the interactions in Figs. 2(a) and 2(b) will follow subsequently. Let $U^{d1}_{\substack{s\\h}}$ and $U^{d2}_{\substack{s\\h}}$ refer to the fields diffracted from the edges Q_1 and Q_2, respectively. Then, $U^{d1}_{\substack{s\\h}}$ and $U^{d2}_{\substack{s\\h}}$ are given in terms of GTD as:

$$(2) \qquad U^{d1}_{\substack{s\\h}} \sim U^{i}_{\substack{s\\h}}(Q_1)\, D_{\substack{s\\h}}(\phi_1,\phi_1) \sqrt{\frac{\rho_{e1}}{s_1(\rho_{e1}+s_1)}}\; e^{-iks_1}$$

and

$$(3) \qquad U^{d2}_{\substack{s\\h}} \sim U^{i}_{\substack{s\\h}}(Q_2)\, D_{\substack{s\\h}}(\phi_2,\phi_2) \sqrt{\frac{\rho_{e2}}{s_2(\rho_{e2}+s_2)}}\; e^{-iks_2}$$

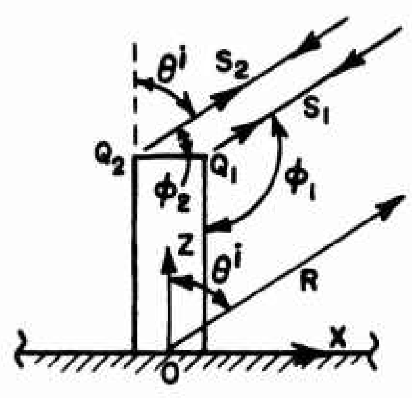

Fig. 3. Angles and distances associated with Fig. 2(c).

where $\phi_1 = \pi - \theta^i$ and $\phi_2 = \pi/2 - \theta^i$ as in Fig. 3. The far zone distances s_1 and s_2 measured from Q_1 and Q_2 are also shown in Fig. 3. The caustic distances ρ_{e1} and ρ_{e2} are

(4); (5) $$\rho_{e1} = \frac{a}{2\sin\theta^i} \quad ; \quad \rho_{e2} = -\frac{a}{2\sin\theta^i} \quad .$$

The $D_{\substack{s\\h}}(\psi,\psi')$ in (2) and (3) is the edge diffraction coefficient given in reference [3]; in the present case $D_{\substack{s\\h}}(\psi,\psi')$ of reference [3] reduces to the Keller form:

(6a) $$D_{\substack{s\\h}}(\psi,\psi') = \frac{e^{-i\frac{\pi}{4}}\left(\frac{1}{n}\sin\frac{\pi}{n}\right)}{\sqrt{2\pi k}}\left[\frac{1}{\cos\frac{\pi}{n} - \cos\frac{\beta^-}{n}} \mp \frac{1}{\cos\frac{\pi}{n} - \cos\frac{\beta^+}{n}}\right]$$

with

(6b); (6c) $$\beta^{\mp} = \psi \mp \psi' \quad ; \quad \text{and } n = \frac{3}{2} \text{ for a local right angle wedge at } Q_1 \text{ and } Q_2.$$

Next, we let $U^{rdr}_{\substack{s\\h}}$ denote the field associated with the reflected-diffracted-reflected ray in Fig. 2(d). It can be easily shown that

(7) $$U^{rdr}_{\substack{s\\h}} \sim \tilde{U}^i_{\substack{s\\h}}(Q_1) \cdot \left[R_{\substack{s\\h}}(Q_R)\right]^2 D_{\substack{s\\h}}(\theta^i,\theta^i)\sqrt{\frac{\rho_c}{s_3(\rho_c + s_3)}}\, e^{-iks_3}$$

where

(8) $$\tilde{U}^i_{\substack{s\\h}}(x,z) \doteq A_{\substack{s\\h}}\, e^{i[kx\sin\theta^i - kz\cos\theta^i]} = U^i_{\substack{s\\h}}(x,-z) \quad ,$$

and the distance s_3 is shown in Fig. 4.

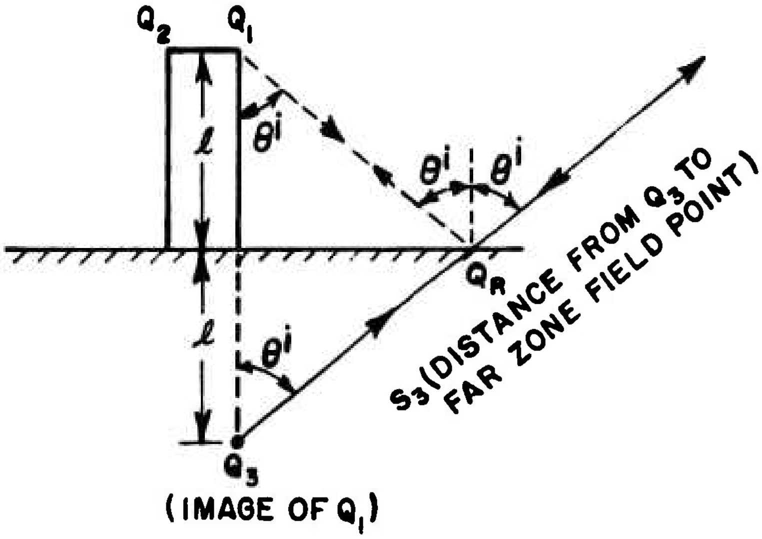

Fig. 4. Angles and distances associated with Fig. 2(d).

The caustic distance ρ_c is identical to ρ_{e1} of (4). $D_{\substack{s\\h}}(\theta^i,\theta^i)$ is given by (6a) with $\psi = \theta^i$ and $\psi' = \theta^i$; also n = 3/2 as before. Finally, the surface reflection coefficient at Q_R is given by:

$$(9) \qquad R_s(Q_R) = \frac{\cos\theta^i - \sqrt{\varepsilon_r(Z_s) - \sin^2\theta^i}}{\cos\theta^i + \sqrt{\varepsilon_r(Z_s) - \sin^2\theta^i}}$$

$$(10) \qquad R_h(Q_R) = \frac{\varepsilon_r(Z_s)\cos\theta^i - \sqrt{\varepsilon_r(Z_s) - \sin^2\theta^i}}{\varepsilon_r(Z_s)\cos\theta^i + \sqrt{\varepsilon_r(Z_s) - \sin^2\theta^i}}$$

wherein $\varepsilon_r(Z_S)$ is a given complex function of the surface impedance Z_S; since Z_S is dependent on the frequency, $\varepsilon_r(Z_S)$ would also be automatically frequency dependent. On the other hand, $R_{\substack{s\\h}}$ depends not only on the frequency, but on the angle of arrival θ^i as well. The behavior of $R_{\substack{s\\h}}$ as a function of θ^i for a given set of frequencies is presented in

Figs. 5-14; these values of $R_{\substack{s\\h}}$ are calculated via (9) and (10) by employing given values of $\epsilon_r(Z_s)$ at the appropriate frequencies. Both, the amplitude and phase of $R_{\substack{s\\h}}$ are illustrated in these figures.

Next, we analyze the interactions in Figs. 2(a) and 2(b) by first picking a near field point in which case only one doubly-reflected ray of Fig. 2(a) contributes to the field; let it's field be denoted as $U^{rr}_{\substack{s\\h}}$. For the sake of definiteness, let the near field point be above the dot-dashed line of Fig. 2(a). Thus,

$$(11);\ (12) \qquad U^{rr}_{\substack{s\\h}} \sim \mp R_{\substack{s\\h}}(Q_z)\, \tilde{U}^i_{\substack{s\\h}}(Q_c)\sqrt{\frac{\rho_r}{\rho_r + d}}\, e^{-ikd};\ \rho_r = a/2 \sin\theta^i.$$

The distance d is from Q_c to the near field point. Q_z and Q_c are points of reflection on the surface z=0 and the cylinder, respectively. The caustic distance ρ_r for the ray reflected from the cylinder (after reflection from z=0) turns out to be identical to ρ_{e1} of (4). In the far zone limit, $d \to s_1$.

Now, let $U^{dr}_{\substack{s\\h}}$ and $U^{rd}_{\substack{s\\h}}$ denote the diffracted-reflected, and the reflected-diffracted ray fields corresponding to Fig. 2(b), respectively. In the far zone, $U^{dr}_{\substack{s\\h}} = U^{rd}_{\substack{s\\h}}$. In the near zone (where (11) is evaluated):

$$(13) \qquad U^{rd}_{\substack{s\\h}} \sim \tilde{U}^i_{\substack{s\\h}}(Q_1)\, R_{\substack{s\\h}}(Q_R)\, D_{\substack{s\\h}}(\phi_1,\phi_1')\sqrt{\frac{\rho_c}{s_1'(\rho_c + s_1')}}\, e^{-iks_1'},$$

and $\rho_c = \rho_{e1}$ of (4). The distance s_1' is from Q_1 to the near field point. Also, $\phi_1' = \theta^i$ and $\phi_1 < \pi - \theta^i$ in the near zone; however, $\phi_1 \to \pi - \theta^i$, and $s_1' \to s_1$ (also $s_1 \to \infty$) in the far zone. When the far zone limit is taken, one may approximate the transverse spread factor $\sqrt{\frac{\rho}{\rho + s}}$ of the ray tubes by $\sqrt{\frac{\rho}{s}}$ in the field expressions (for the far zone condition $s \gg \rho$). s and

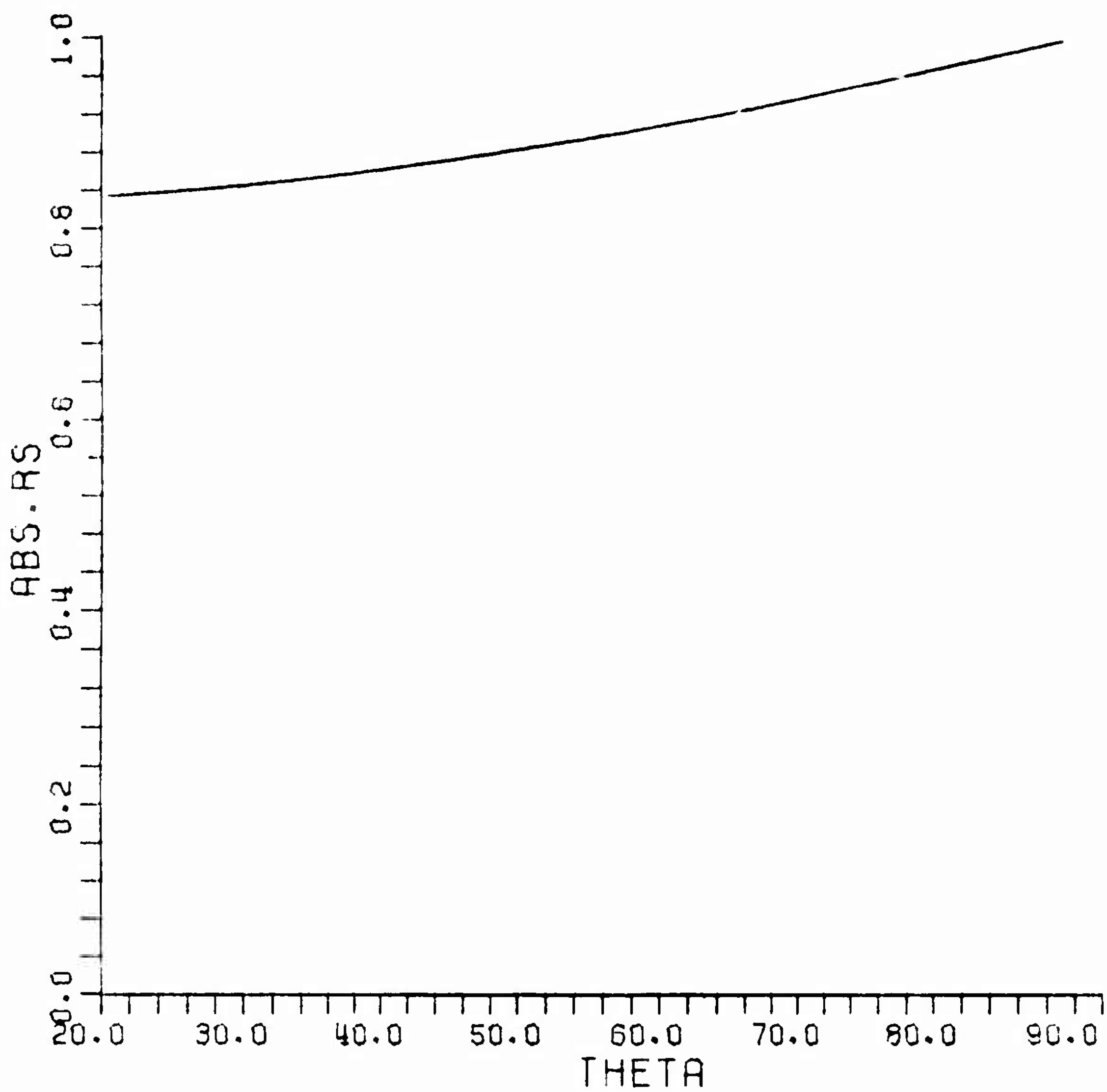

Fig. 5(a). $|R_s|$ vs θ^i at f = 1 GHz; $|R_s|$ = ABS.RS; θ^i = THETA in degrees.

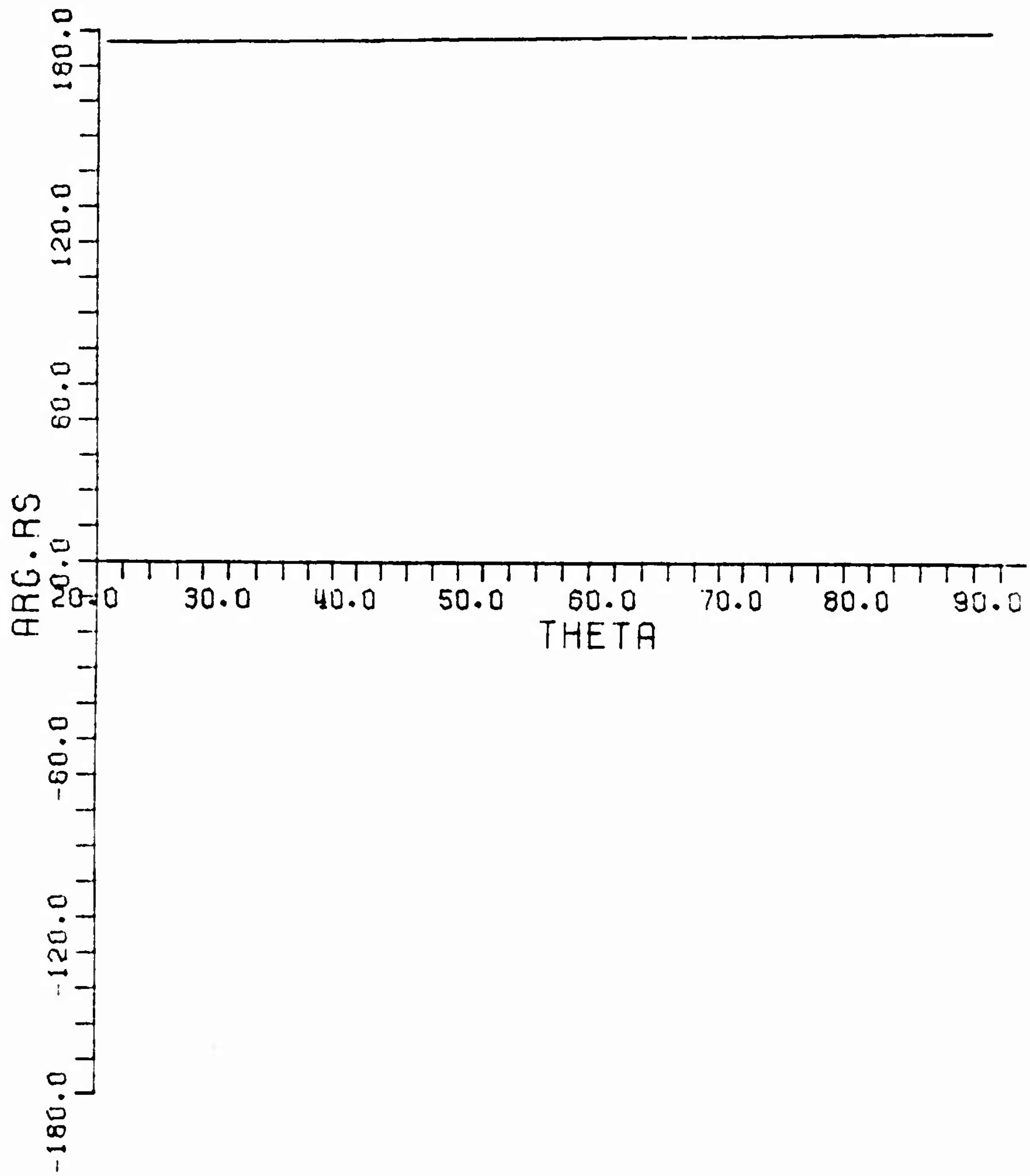

Fig. 5(b). Arg R_s vs θ^i at f = 1 GHz; Arg R_s = ARG.RS; θ^i = THETA in degrees.

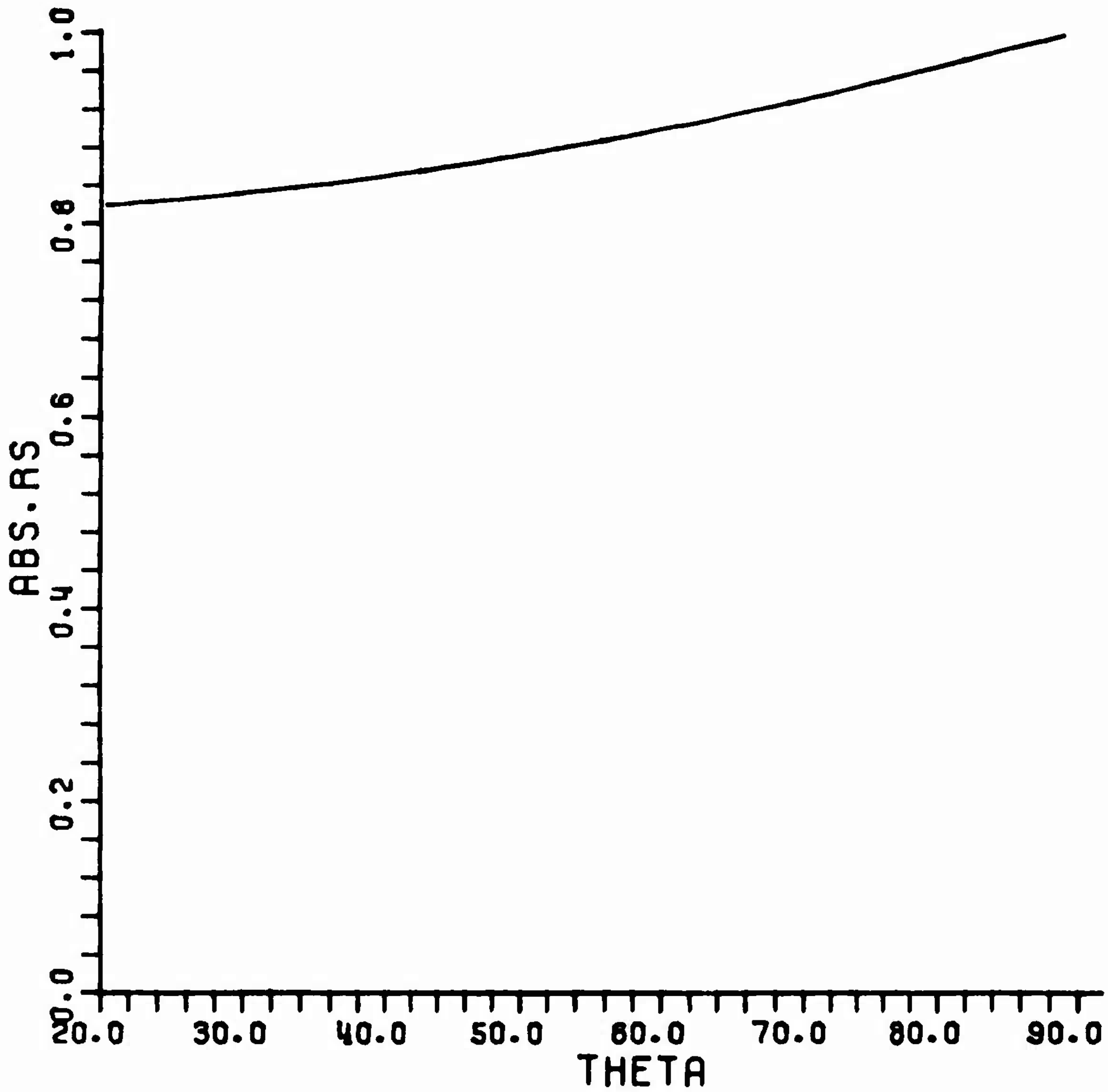

Fig. 6(a). $|R_s|$ vs θ^i at f = 2 GHz.

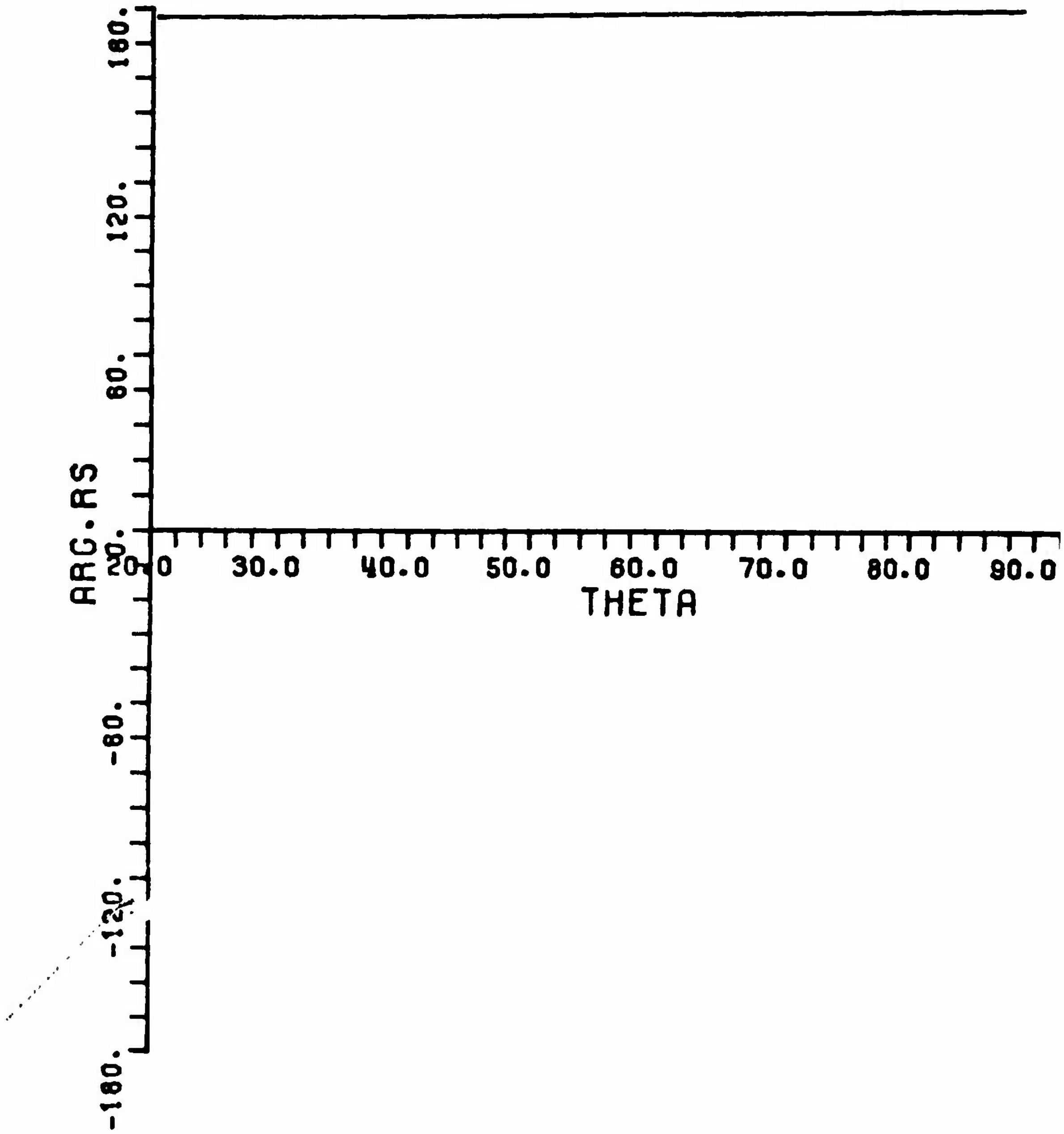

Fig. 6(b). Arg R_s vs θ^i at f = 2 GHz.

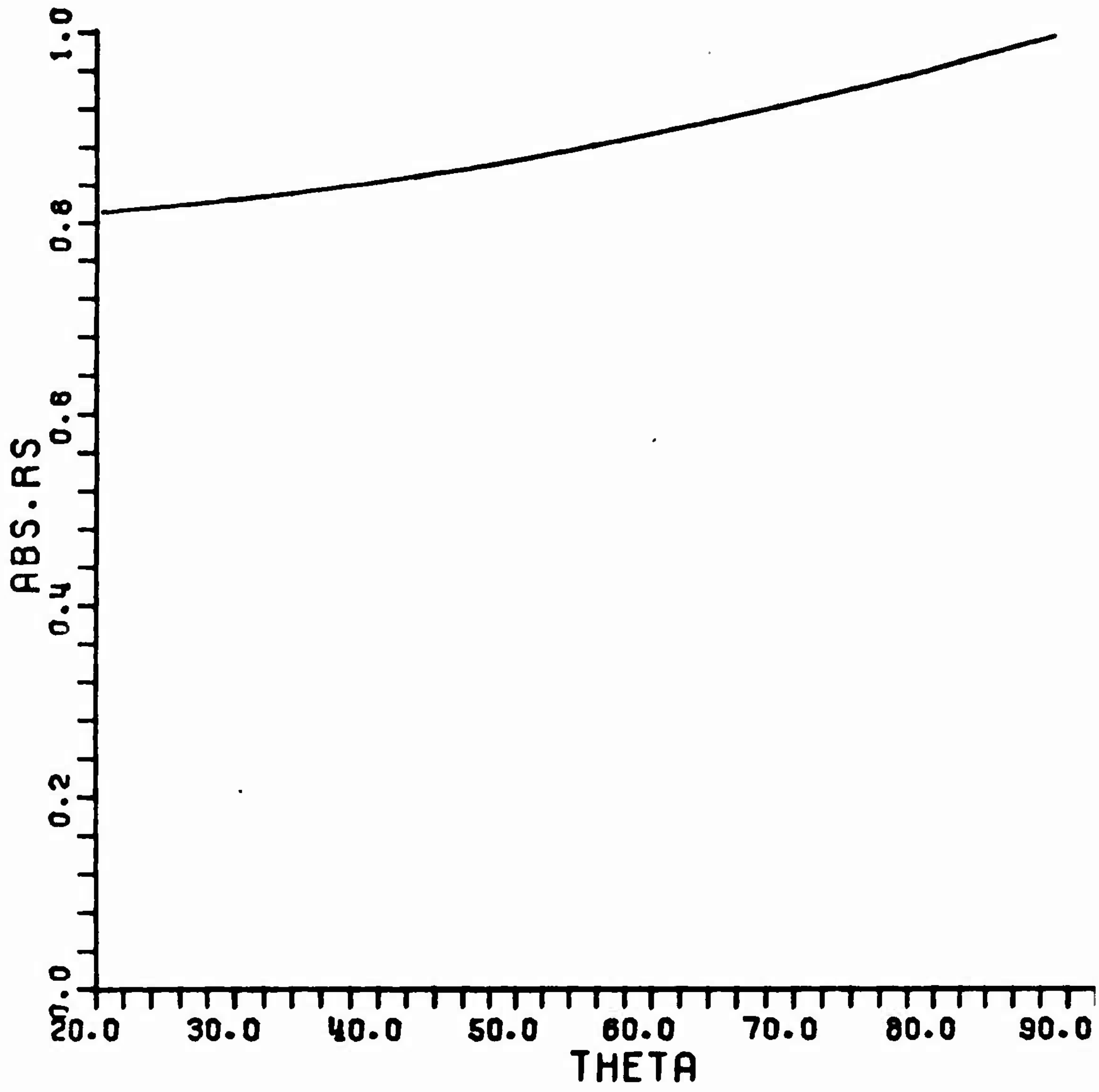

Fig. 7(a). $|R_s|$ vs θ^i at f = 4 GHz.

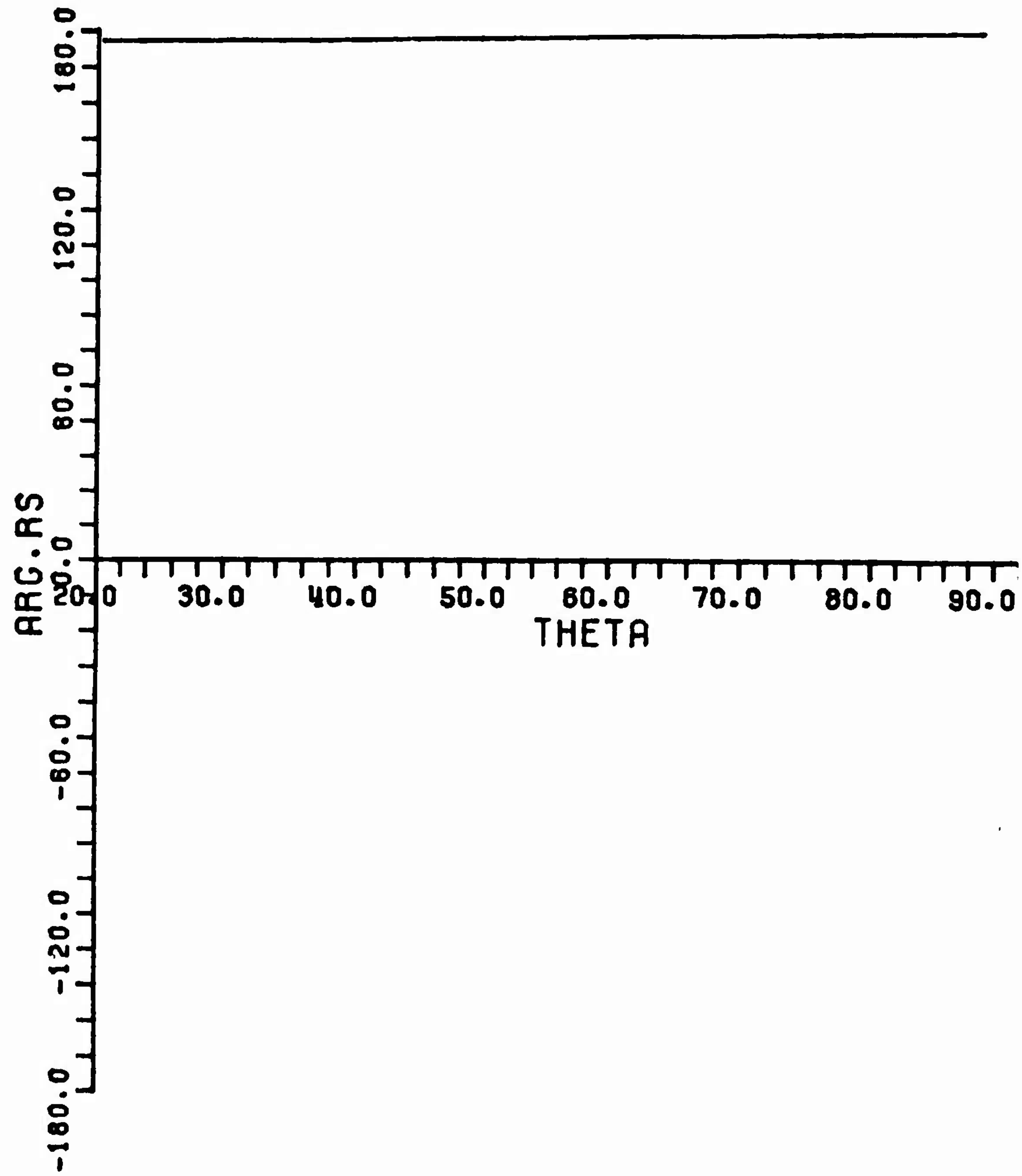

Fig. 7(b). Arg R_s vs θ^i at f = 4 GHz.

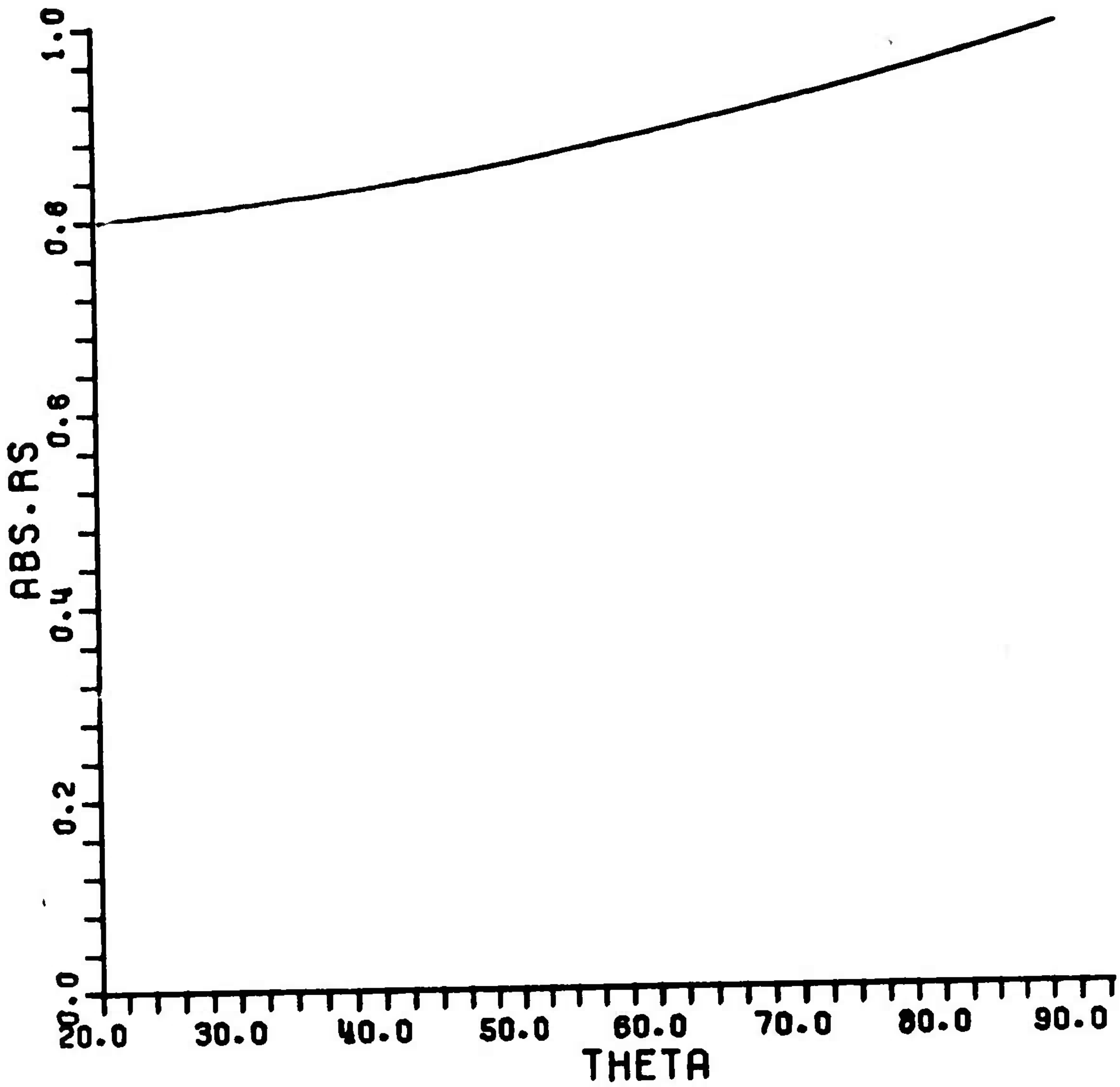

Fig. 8(a). $|R_s|$ vs θ^i at f = 8 GHz.

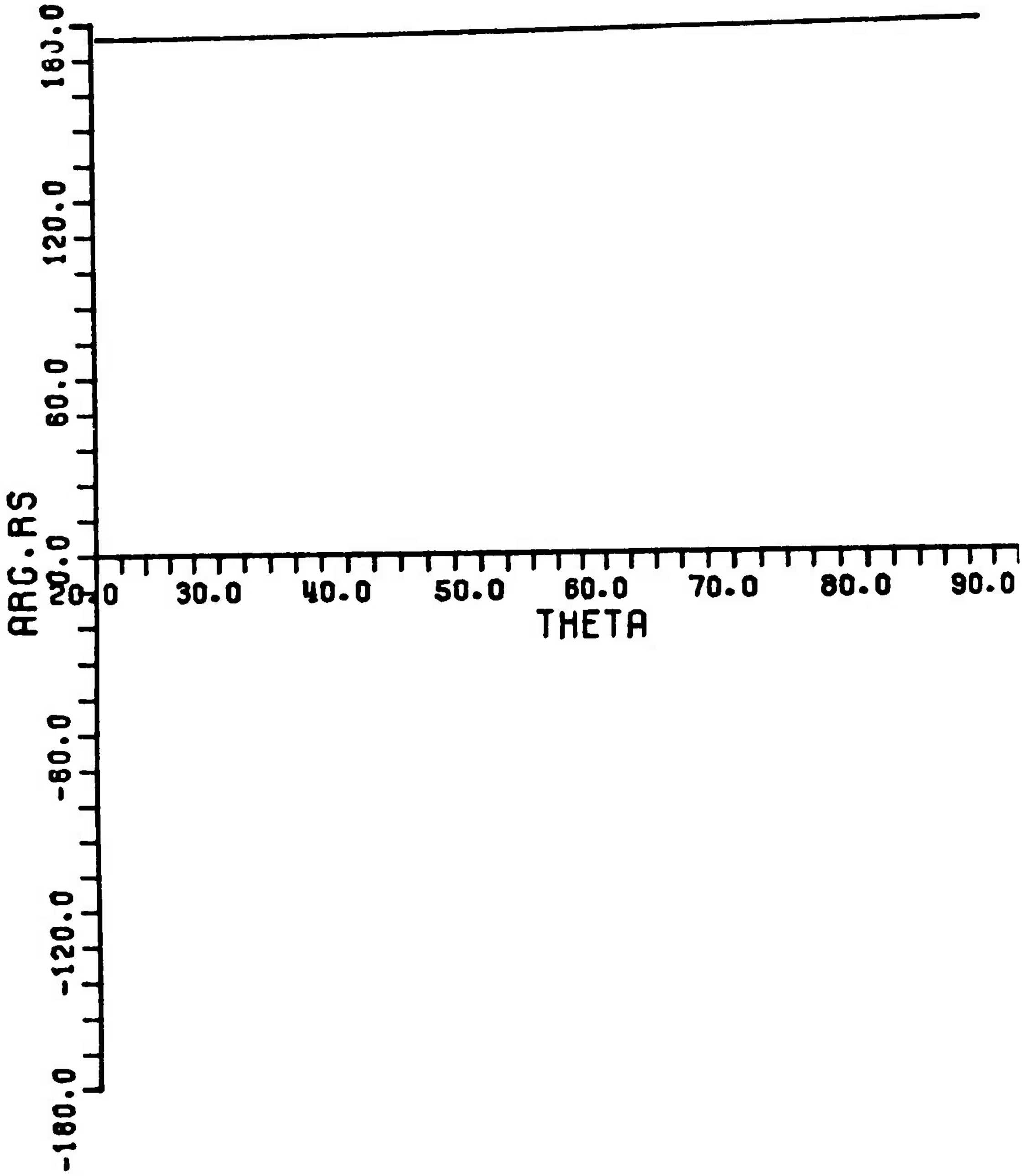

Fig. 8(b). Arg R_s vs θ^i at f = 8 GHz.

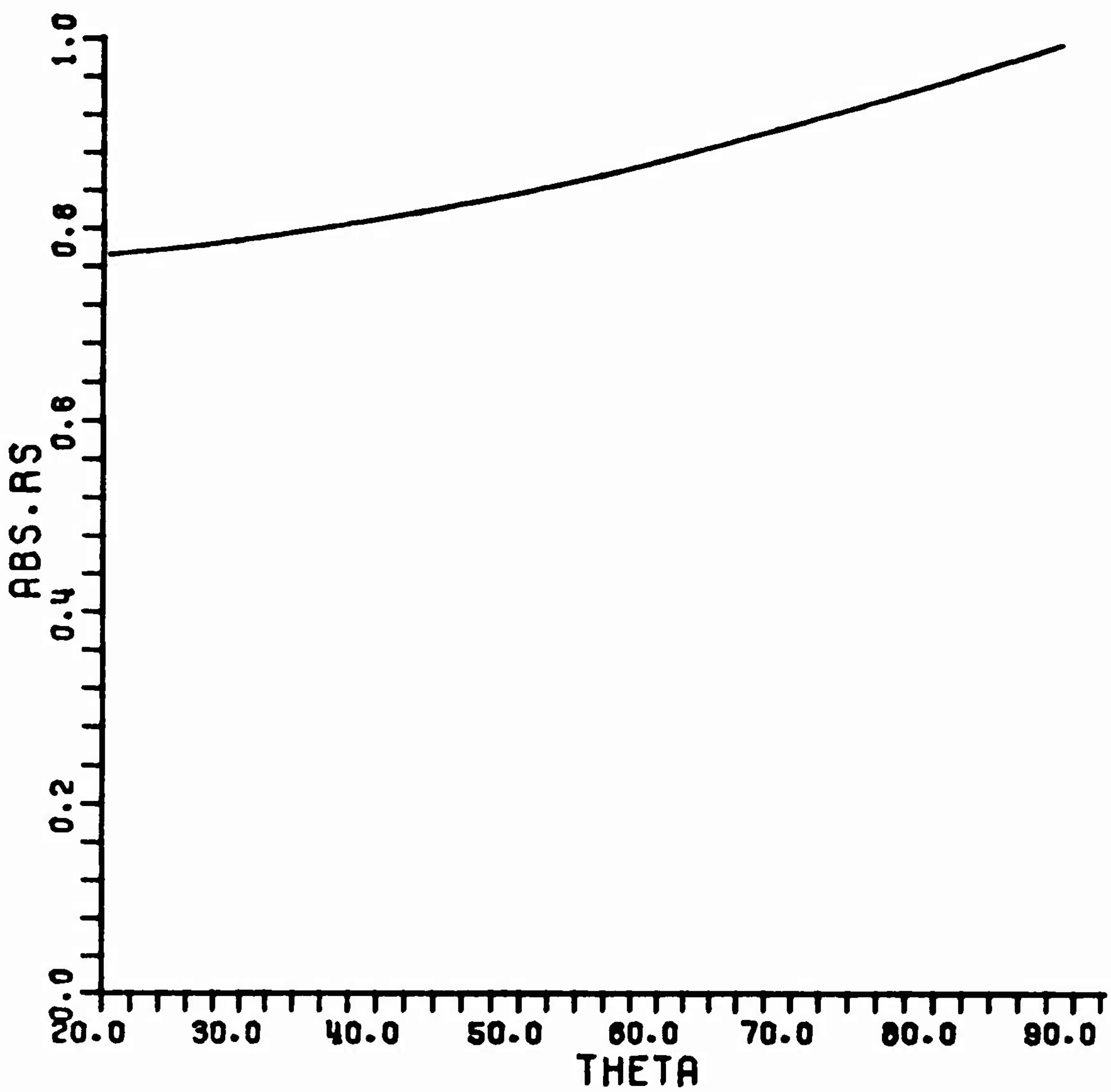

Fig. (9a). $|R_s|$ vs θ^i at f = 16 GHz.

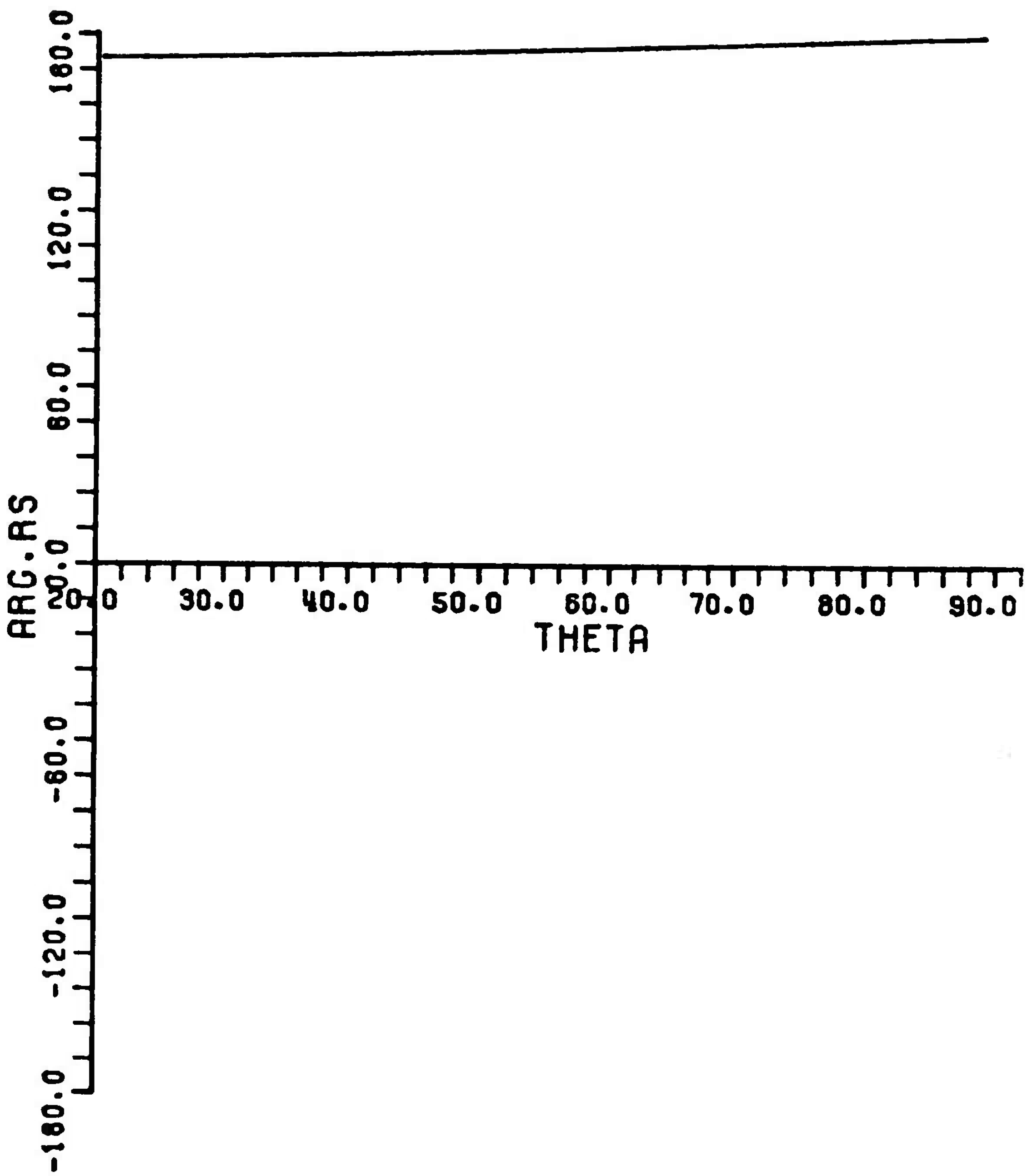

Fig. (9b). Arg R_s vs θ^i at f = 16 GHz.

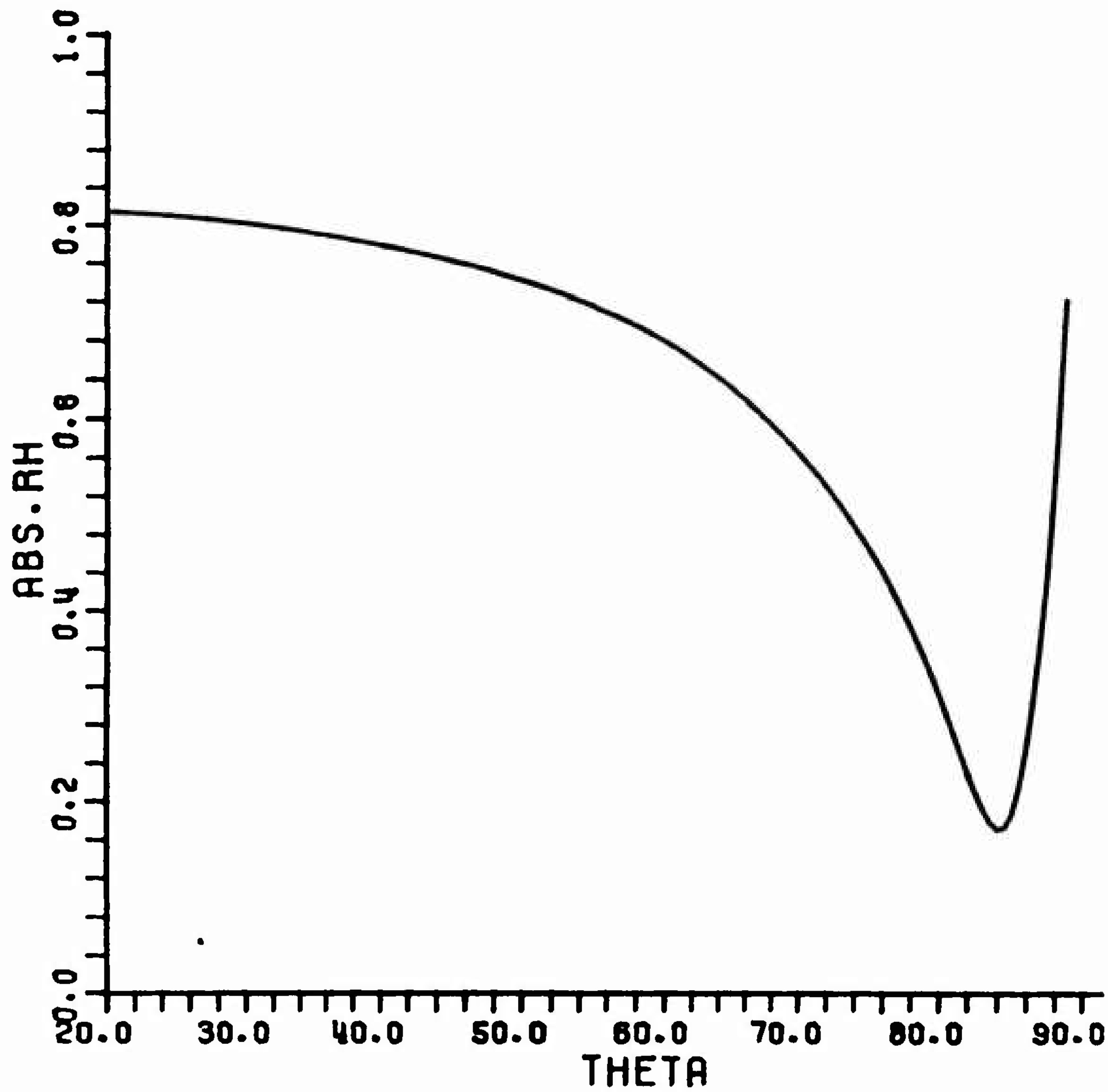

Fig. (10a). $|R_h|$ vs θ^i at f = 1 GHz; $|R_h|$ = ABS.RH; θ^i = THETA in degrees.

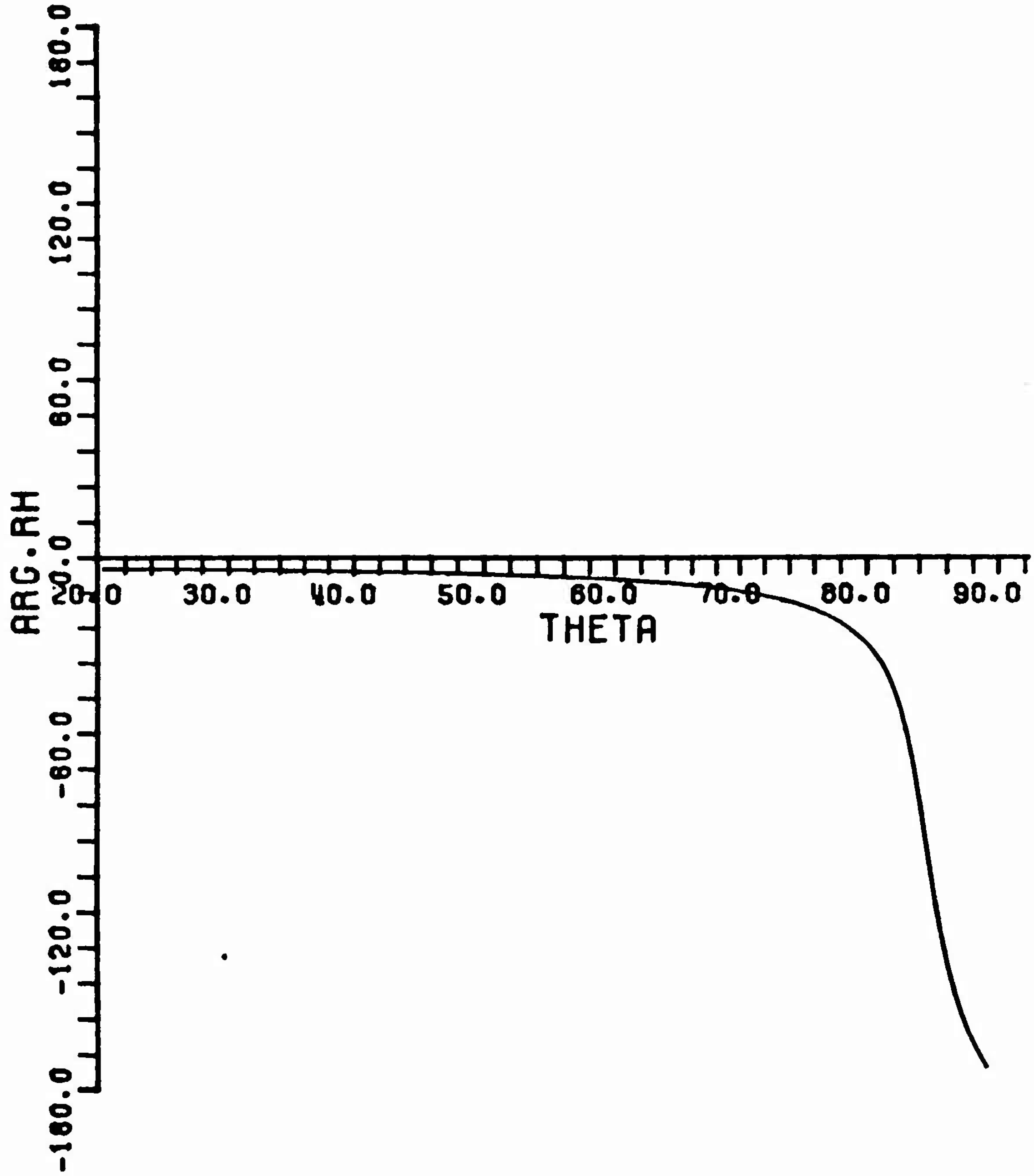

Fig. (10b). Arg R_h vs θ^i at f = .1 GHz.
Arg R_h = ARG.RH; θ^i = THETA in degrees.

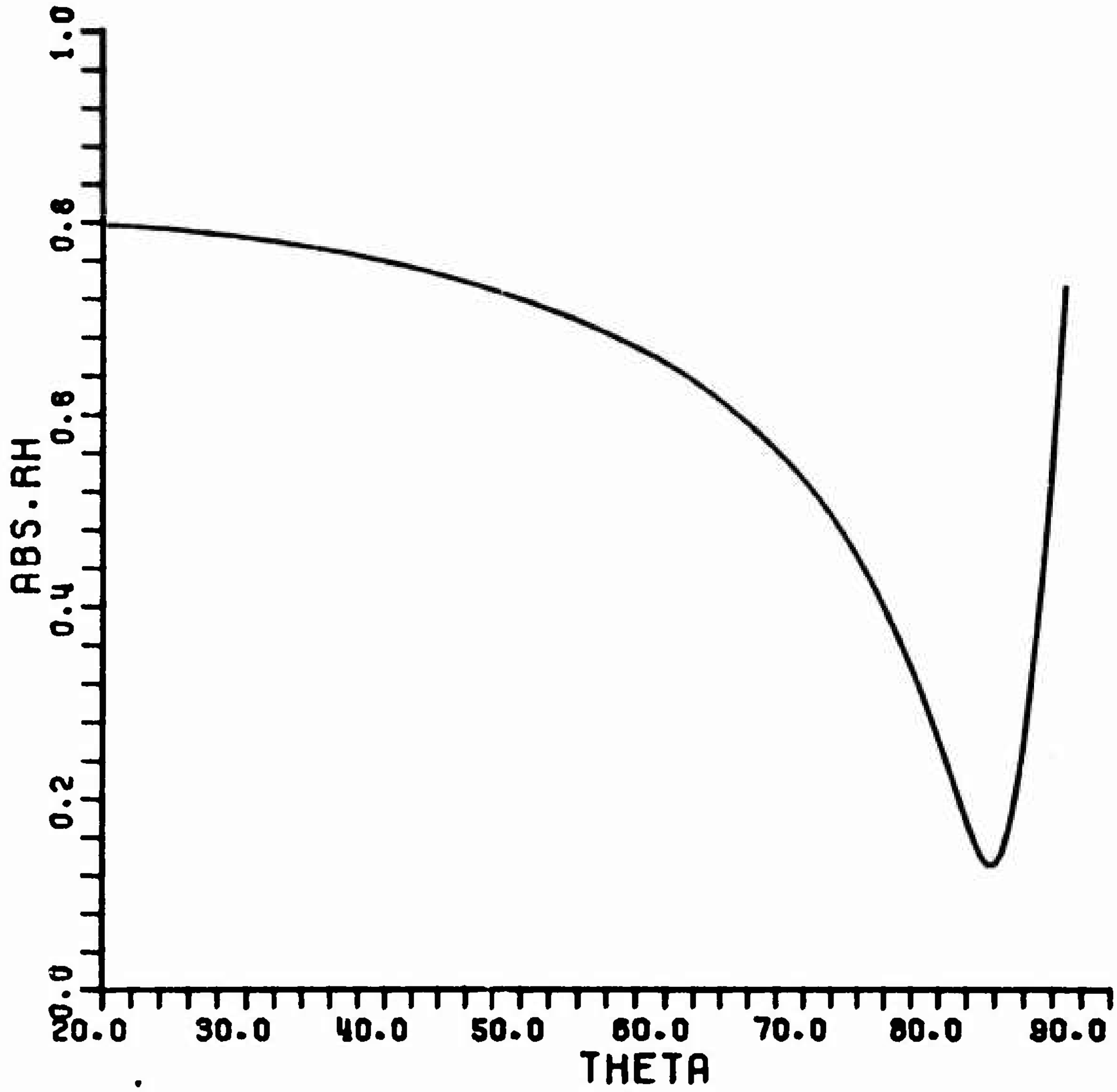

Fig. (11a). $|R_h|$ vs θ^i at f = 2 GHz.

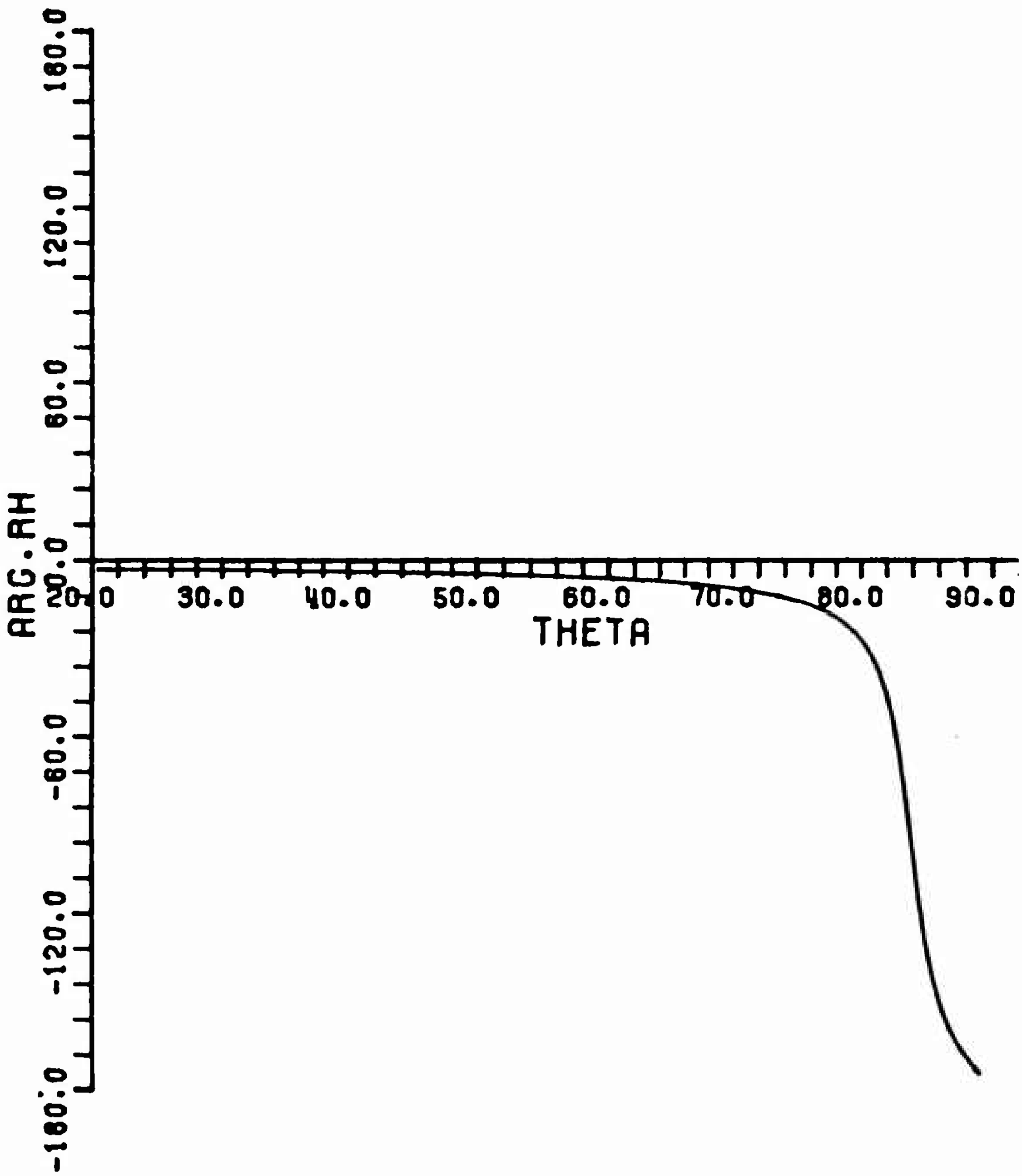

Fig. (11b). Arg R_h vs θ^i at f = 2 GHz.

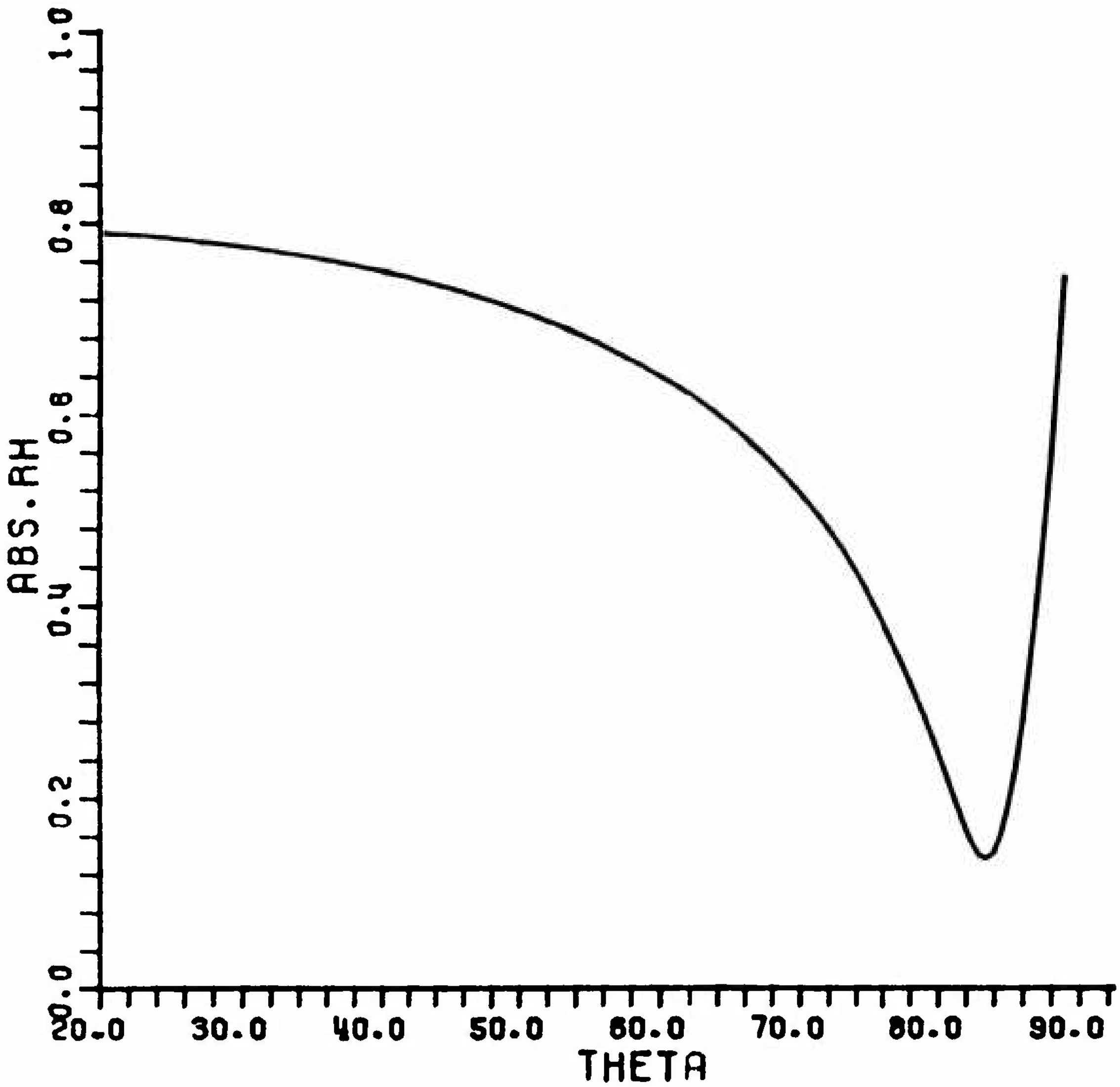

Fig. (12a). $|R_h|$ vs θ^i at f = 4 GHz.

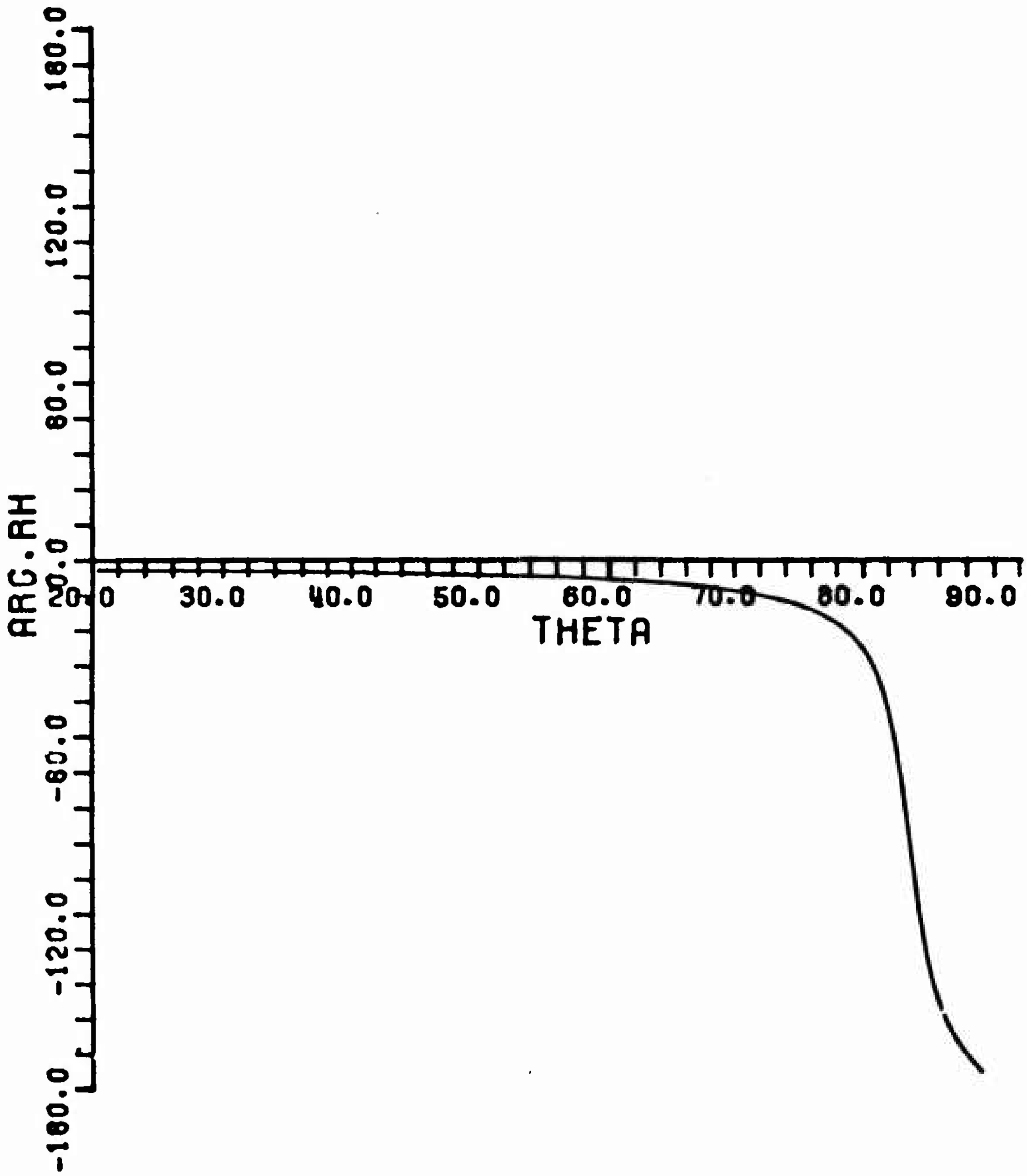

Fig. (12b). Arg R_h vs θ^i at f = 4 GHz.

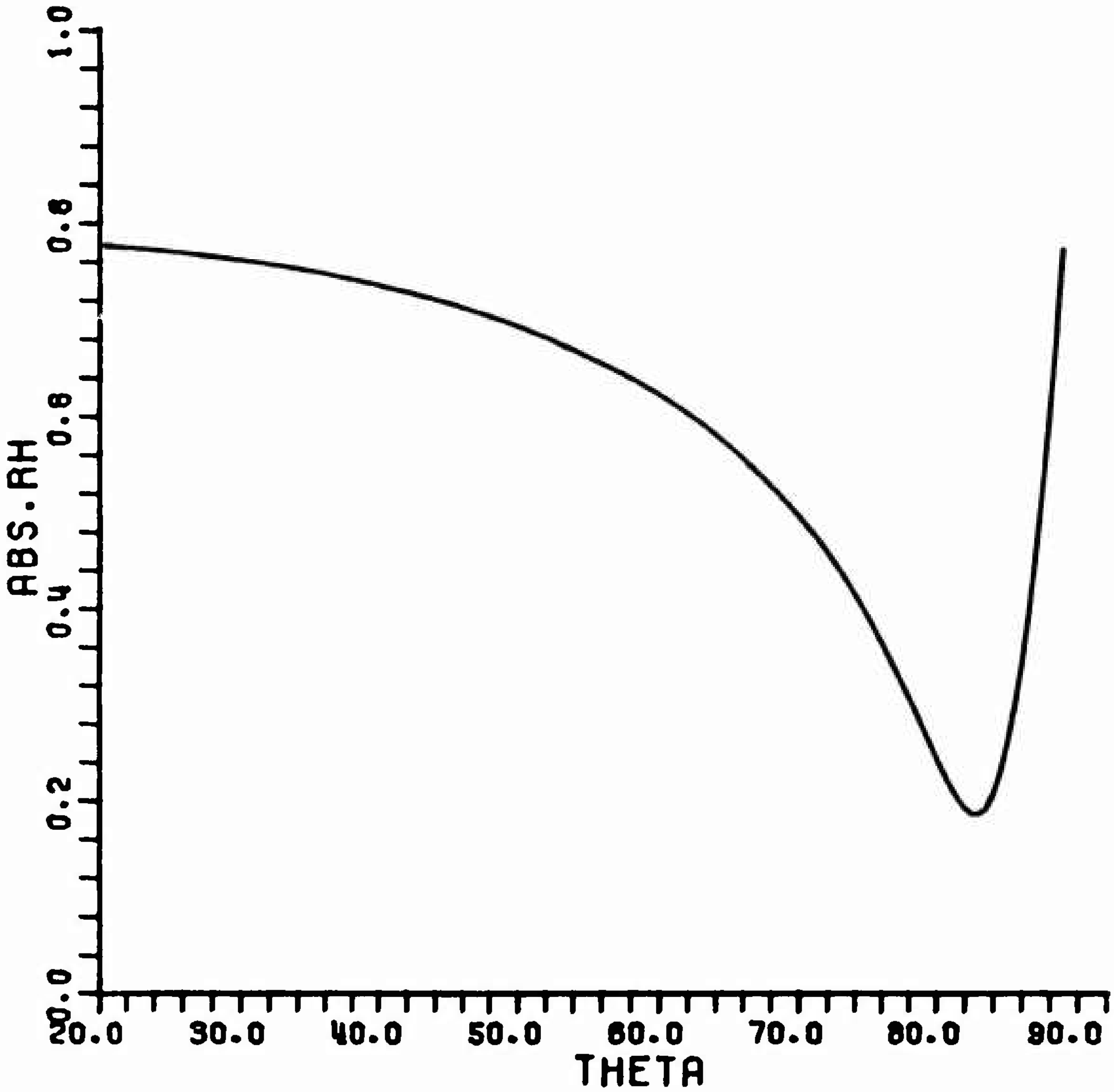

Fig. (13a). $|R_h|$ vs θ^i at f = 8 GHz.

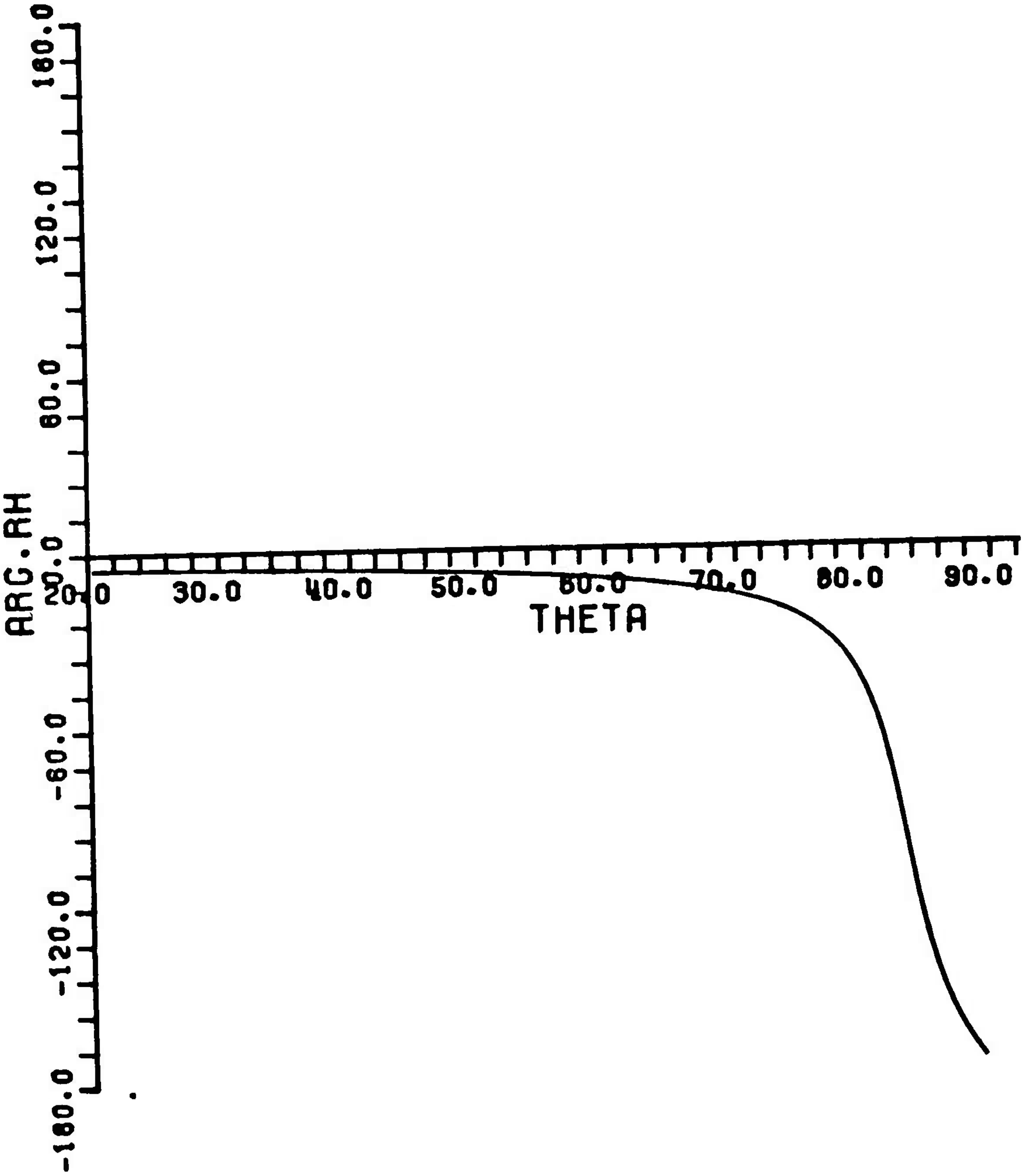

Fig. (13b). Arg R_h vs θ^i at f = 8 GHz.

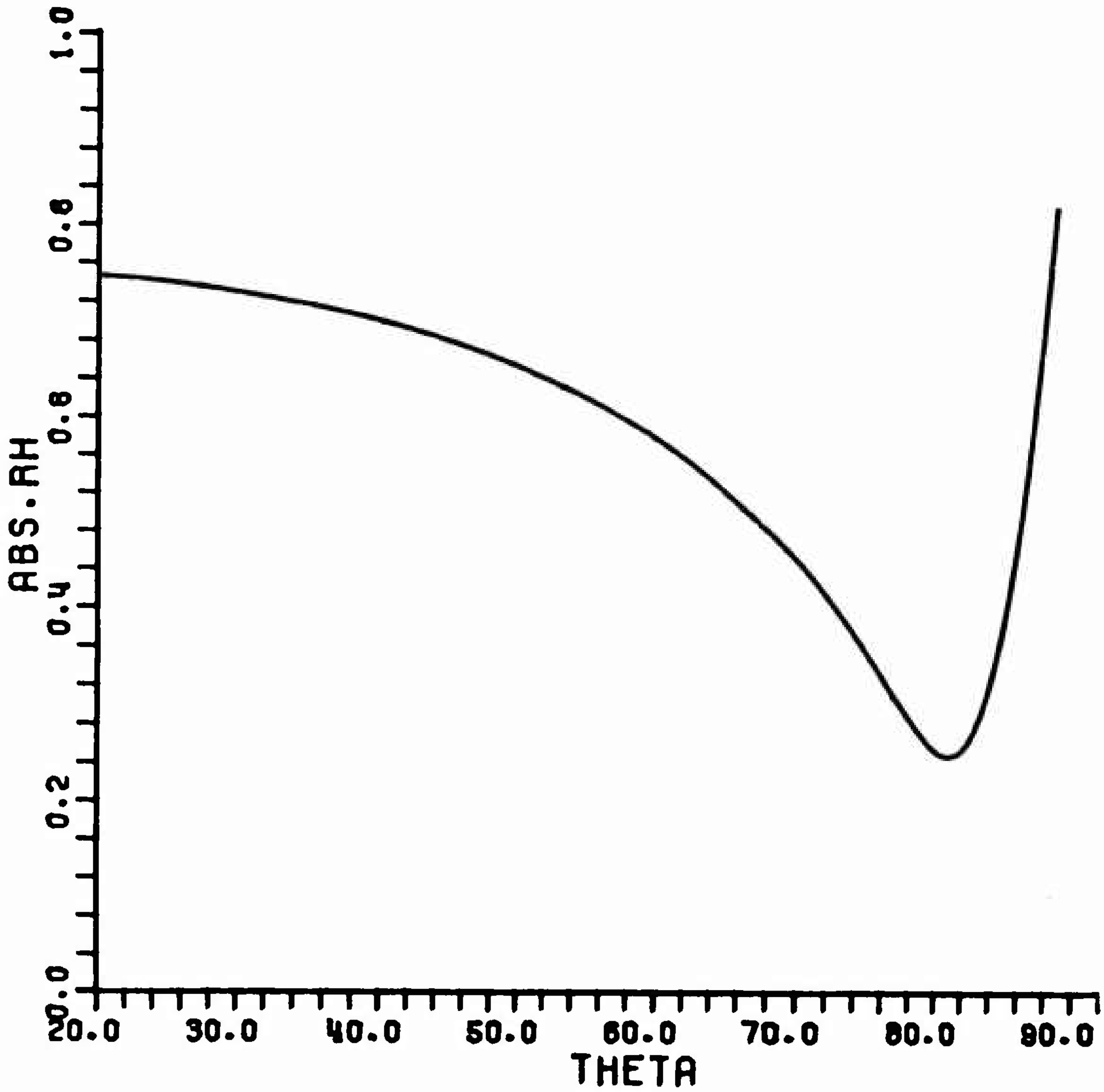

Fig. (14a). $|R_h|$ vs θ^i at f = 16 GHz.

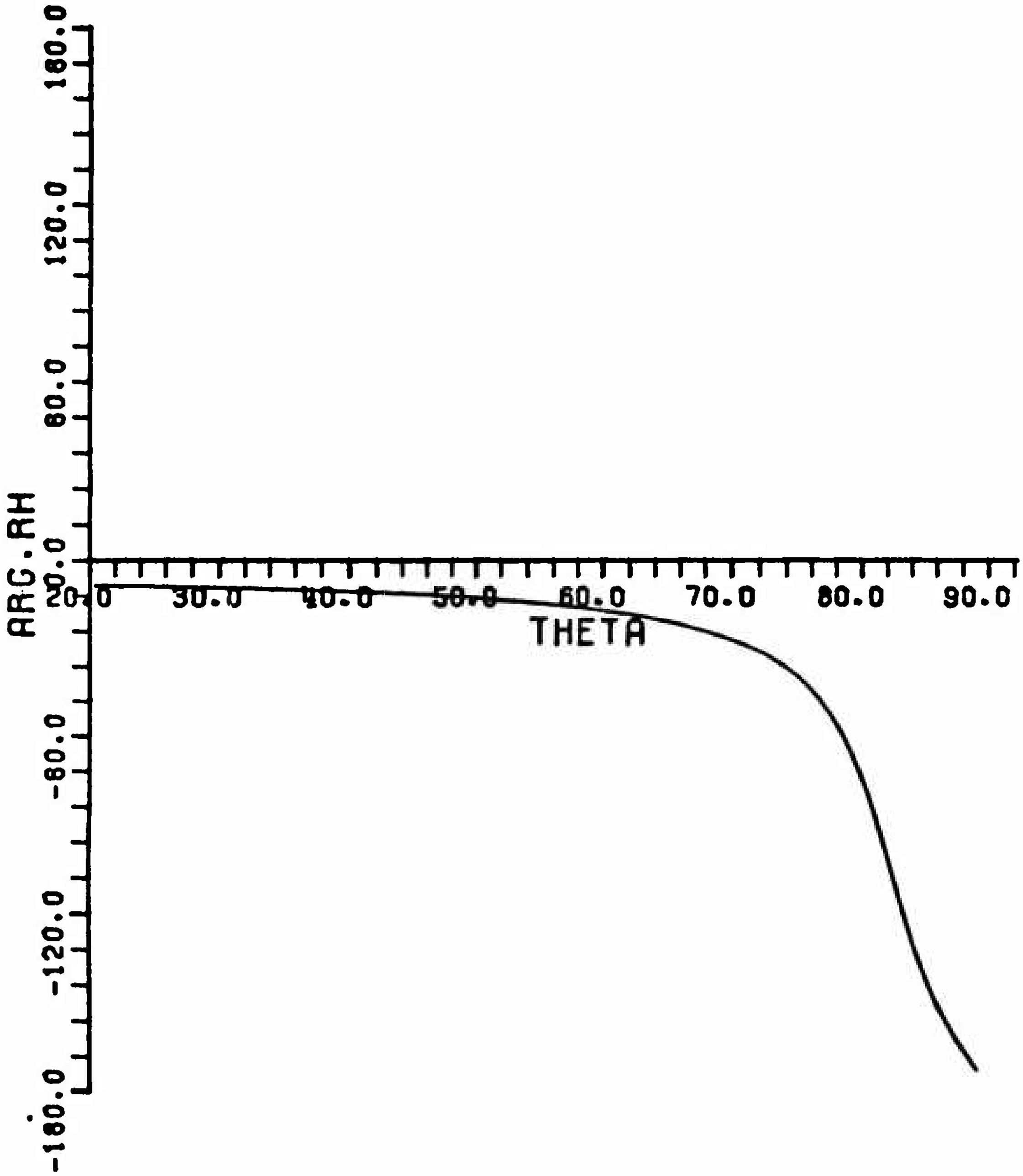

Fig. (14b). Arg R_h vs θ^i at f = 16 GHz.

ρ are the ray and caustic distances, respectively. Hence, s could be s_1, s_2 or s_3; and ρ could be ρ_{el}, ρ_c or ρ_r, etc. The $D_{s \atop h}$ in (13) is taken from reference [3] to be:

$$\text{(14)} \qquad D_{s \atop h}(\phi_1,\phi_1') = \frac{e^{-i\frac{\pi}{4}}}{\sqrt{2\pi k}} \left[\frac{\frac{1}{n}\sin\frac{\pi}{n} \cdot F[kL^i a(\phi_1-\phi_1')]}{\cos\frac{\pi}{n} - \cos\frac{\phi_1-\phi_1'}{n}} \right.$$

$$\pm \frac{1}{2n}\left\{\cot\left(\frac{\pi+(\phi_1+\phi_1')}{2n}\right) F\left[kL^{rn}a^+(\phi_1+\phi_1')\right]\right.$$

$$\left.\left. + \cot\left(\frac{\pi-(\phi_1+\phi_1')}{2n}\right) F\left[kL^{ro}a(\phi_1+\phi_1')\right]\right\}\right] ,$$

with

$$\text{(15a; 15b)} \qquad a^+(\beta) = 2\cos^2\frac{2\pi n-\beta}{2} \quad ; \quad a(\beta) = 2\cos^2\frac{\beta}{2} ,$$

and $n = 3/2$ as before for a local right angle wedge at Q_1. In the present problem, $F[kL^i a(\phi_1-\phi_1')]$ and $F[kL^{rn}a^+(\phi_1+\phi_1')]$ may be replaced by unity since $kL^i a(\phi_1-\phi_1')$ and $kL^{rn}a^+(\phi_1+\phi_1')$ are much larger than 10 due to the fact that the backscatter direction is not only far from the incident shadow boundary but the incident and reflection shadow boundaries are sufficiently far apart. One notes that $F(\chi)$ essentially becomes unity when $\chi > 10$; when all $F(\chi)$ terms become unity, the $D_{s \atop h}$ of (14) reduces to the Keller form of 6(a). From reference [3], L^{ro} is given by

$$L^{ro} = \frac{s_1'(\rho_c+s_1')(\rho_1^r)(\rho_2^r)}{\rho_c(\rho_1^r+s_1')(\rho_2^r+s_1')} .$$

In our problem, $\rho_1^r \to \infty$, $\rho_2^r = \rho_r$, and $\rho_c = \rho_r = \dfrac{a}{2\sin\theta^i}$, so that

$$\text{(16)} \qquad L^{ro} = s_1' .$$

Let $\phi_1 = \pi - \theta^i - \varepsilon$ where ε is a positive number however small. $\phi_1' = \theta^i$ as indicated previously. Then $D_{\substack{s\\h}}$ of (14) becomes

$$(17) \qquad D_{\substack{s\\h}}(\phi_1,\phi_1') \approx \frac{e^{-i\frac{\pi}{4}}}{\sqrt{2\pi k}} \left[\frac{\frac{1}{n}\sin\frac{\pi}{n}}{\cos\frac{\pi}{n} - \cos\left(\frac{\pi - 2\theta^i - \varepsilon}{n}\right)} \pm \frac{1}{2n}\left\{\cot\frac{\pi}{n} + \frac{2n}{\varepsilon} F\left[kL^{ro}a(\phi_1+\phi_1')\right]\right\} \right] .$$

with

$$(18) \qquad F\left[kL^{ro}a(\phi_1+\phi_1')\right] \approx \left\{\left|\sqrt{\pi kL^{ro}a(\phi_1+\phi_1')}\right| - 2\left[kL^{ro}a(\phi_1+\phi_1')\, e^{i\frac{\pi}{4}}\right]\right\} e^{i\frac{\pi}{4} + ikL^{ro}a(\phi_1+\phi_1')}$$

and

$$(19) \qquad a(\phi_1+\phi_1') = a(\pi-\varepsilon) = 2\cos^2\frac{\pi-\varepsilon}{2} \approx \frac{\varepsilon^2}{2} .$$

Therefore,

$$(20) \qquad F\left[kL^{ro}a(\phi_1+\phi_1')\right] \approx \left[\sqrt{\frac{\pi k s_1'}{2}}\,\varepsilon\, e^{i\frac{\pi}{4}} - i\, k s_1'\, \varepsilon^2\right] .$$

Also,

$$(21) \qquad s_1'\,\varepsilon \approx \ell \sin\theta^i$$

so that

$$D_{\substack{s\\h}}(\phi_1,\phi_1') \approx \left[\frac{e^{-i\frac{\pi}{4}} \frac{1}{n} \sin\frac{\pi}{n}}{\sqrt{2\pi k}\left(\cos\frac{\pi}{n} - \cos\left[\frac{\pi - 2\theta^i}{n}\right]\right)} \right. \tag{22}$$

$$\left. \pm \frac{e^{-i\frac{\pi}{4}}}{2n\sqrt{2\pi k}} \cot\frac{\pi}{n} \pm \frac{\sqrt{s_1}}{2} \mp \frac{e^{i\frac{\pi}{4}}}{\sqrt{2\pi k}} k\ell \sin\theta^i \right] .$$

Incorporating (22) in (13) yields a near field value for $U_{\substack{s\\h}}^{rd}$; one could similarly obtain a near field expression for $U_{\substack{s\\h}}^{dr}$ in terms of $D_{\substack{s\\h}}(\hat{\phi}_1,\hat{\phi}_1')$ where $\hat{\phi}_1' = \pi - \theta^i$ and $\hat{\phi}_1$ is chosen to be $\theta^i - \varepsilon$. The choice of $\phi_1 = \pi - \theta^i - \varepsilon$ and $\hat{\phi}_1 = \theta^i - \varepsilon$ ensures that the near field point where $U_{\substack{s\\h}}^{rd} + U_{\substack{s\\h}}^{dr}$ is evaluated is indeed in the region where the doubly reflected field $U_{\substack{s\\h}}^{rr}$ exists. Consequently, the total field within this region (which collapses to a line in the far zone as $s_1 \to \infty$) for the interactions in Figs. 2a and 2b is the far zone limit of

$$U_{\substack{s\\h}}^{dr} + U_{\substack{s\\h}}^{rd} + U_{\substack{s\\h}}^{rr} .$$

When $D_{\substack{s\\h}}(\hat{\phi}_1,\hat{\phi}_1')$ is simplified in the manner that $D_{\substack{s\\h}}(\phi_1,\phi_1')$ of (14) is simplified to obtain the expression in (22), and ε is allowed to approach zero as $s_1 \to \infty$ (far zone), the following far zone result for $U_{\substack{s\\h}}^{dr} + U_{\substack{s\\h}}^{rd} + U_{\substack{s\\h}}^{rr}$ is obtained:

$$(23)\qquad U^{rr}_{\substack{s\\h}} + \left(U^{dr}_{\substack{s\\h}} + U^{rd}_{\substack{s\\h}}\right) \sim \mp A_{\substack{s\\h}}\, R_{\substack{s\\h}}(Q_R)\, e^{i2ka\sin\theta^i}\, e^{i\frac{\pi}{4}} \sqrt{\frac{ka\sin\theta^i}{\pi}}\; \ell\; \frac{e^{-ikR}}{R}$$

$$+ 2 A_{\substack{s\\h}}\, R_{\substack{s\\h}}(Q_R)\, e^{i2ka\sin\theta^i}\, \frac{e^{i\frac{\pi}{4}}}{2\pi k} \left[\frac{\frac{1}{n}\sin\frac{\pi}{n}}{\cos\frac{\pi}{n} - \cos\frac{\pi - 2\theta^i}{n}} \right.$$

$$\left. \pm \frac{1}{2n}\, \frac{\cos\frac{\pi}{n}}{\sin\frac{\pi}{n}} \right] \cdot \sqrt{\frac{a}{2\sin\theta^i}} \cdot \frac{e^{-ikR}}{R}$$

Similarly, the far zone results for $U^{d1}_{\substack{s\\h}}$, $U^{d2}_{\substack{s\\h}}$ and $U^{rdr}_{\substack{s\\h}}$ in (2), (3), and (7) yield:

$$(24)\qquad U^{d1}_{\substack{s\\h}} + U^{d2}_{\substack{s\\h}} + U^{rdr}_{\substack{s\\h}} \sim \left[A_{\substack{s\\h}}\, e^{i2k[a\sin\theta^i + \ell\cos\theta^i]} D_{\substack{s\\h}}(\phi_1,\phi_1) \sqrt{\frac{a}{2\sin\theta^i}} \right.$$

$$+ A_{\substack{s\\h}}\, e^{i2k[-a\sin\theta^i + \ell\cos\theta^i]} D_{\substack{s\\h}}(\phi_2,\phi_2)\; i \sqrt{\frac{a}{2\sin\theta^i}}$$

$$\left. + A_{\substack{s\\h}} \left[R_{\substack{s\\h}}(Q_R)\right]^2 e^{i2k[a\sin\theta^i - \ell\cos\theta^i]} D_{\substack{s\\h}}(\theta^i,\theta^i) \sqrt{\frac{a}{2\sin\theta^i}} \right]$$

$$\cdot \frac{e^{-ikR}}{R} \quad .$$

The following relationships have also been employed in obtaining (23) and (24); these relationships are obtained purely from geometrical considerations which are valid in the far zone.

$$U^i_{\substack{s\\h}}(Q_1)\,\frac{e^{-iks_1}}{s_1} \sim A_{\substack{s\\h}}\,e^{2ik[a\sin\theta^i + \ell\cos\theta^i]}\,\frac{e^{-ikR}}{R}$$

$$U^i_{\substack{s\\h}}(Q_2)\,\frac{e^{-iks_2}}{s_2} \sim A_{\substack{s\\h}}\,e^{2ik[-a\sin\theta^i + \ell\cos\theta^i]}\,\frac{e^{-ikR}}{R}$$

$$\tilde{U}^i_{\substack{s\\h}}(Q_1)\,\frac{e^{-iks_3}}{s_3} \sim A_{\substack{s\\h}}\,e^{2ik[a\sin\theta^i - \ell\cos\theta^i]}\,\frac{e^{-ikR}}{R}$$

$$\tilde{U}^i_{\substack{s\\h}}(Q_1)\,\frac{e^{-iks_1}}{s_1} \sim A_{\substack{s\\h}}\,e^{2ika\sin\theta^i}\,\frac{e^{-ikR}}{R}\quad .$$

The distance R which occurs in the above expressions is shown in Fig. 3.

The RCS is given by $\sigma_{\substack{s\\h}}$, where

$$(25)\qquad \sigma_{\substack{s\\h}} = \lim_{R\to\infty} 4\pi R^2 \left|\left[U^{d1}_{\substack{s\\h}} + U^{d2}_{\substack{s\\h}} + U^{rdr}_{\substack{s\\h}} + U^{rr}_{\substack{s\\h}} + U^{dr}_{\substack{s\\h}} + U^{rd}_{\substack{s\\h}}\right]\right|^2 \Bigg/ \left|A_{\substack{s\\h}}\right|^2 .$$

The various field contributions to $\sigma_{\substack{s\\h}}$ which appear on the RHS of (25) are given in (23) and (24).

Since we would like to compare $\sigma_{\substack{s\\h}}$ with the RCS of the same diameter cylinder of length 2ℓ in the absence of Z_s, the problem of Fig. 15 which corresponds to the latter case is trivially analyzed. Thus, denoting the RCS for the finite length ($= 2\ell$) cylinder in free space by $\tilde{\sigma}_{\substack{s\\h}}$, we express $\tilde{\sigma}_{\substack{s\\h}}$ in terms of the backscattered ray fields as:

$$(26) \qquad \tilde{\sigma}_{\substack{s\\h}} = \lim_{P\to\infty} 4\,\pi R^2 \left| \left[U^{d1}_{\substack{s\\h}} + U^{d2}_{\substack{s\\h}} + U^{d3}_{\substack{s\\h}} \right] \right|^2 \Big/ \left| A_{\substack{s\\h}} \right|^2 .$$

$U^{d1}_{\substack{s\\h}}$ and $U^{d2}_{\substack{s\\h}}$ in (26) correspond to the edge diffracted fields emanating from Q_1 and Q_2, respectively; they are identical to $U^{d1,2}_{\substack{s\\h}}$ in (2) and (3). The field $U^{d3}_{\substack{s\\h}}$ which is the field diffracted from Q_3 is similarly given by:

$$(27) \qquad U^{d3}_{\substack{s\\h}} \sim U^{i}_{\substack{s\\h}}(Q_3)\; D_{\substack{s\\h}}(\phi_3,\phi_3) \sqrt{\frac{\rho_{e3}}{s_3(\rho_{e3} + s_3)}}\; e^{-iks_3}$$

which in the far zone reduces to:

$$(28) \qquad U^{d3}_{\substack{s\\h}} \sim A_{\substack{s\\h}}\, e^{i2k[a \sin\theta^i - \ell \cos\theta^i]}\, D_{\substack{s\\h}}(\theta^i,\theta^i) \sqrt{\frac{a}{2\sin\theta^i}}\; \frac{e^{-ikR}}{R}$$

In deriving (28) from (27), the following far zone approximation is employed:

$$(29) \qquad U^{i}_{\substack{s\\h}}(Q_3) \sqrt{\frac{\rho_{e3}}{s_3(\rho_{e3}+s_3)}}\; e^{-iks_3} \approx A_{\substack{s\\h}}\, e^{i2k[a \sin\theta^i - \ell \cos\theta^i]}$$

$$\cdot \sqrt{\rho_{e3}}\; \frac{e^{-ikR}}{R}$$

where $\rho_{e3} = \dfrac{a}{2\sin\theta^i}$. Also, $\phi_3 = \theta^i$ in this case, and $D_{\substack{s\\h}}(\phi_3,\phi_3)$ is given in 6(a) with $\phi_3 = \theta^i$.

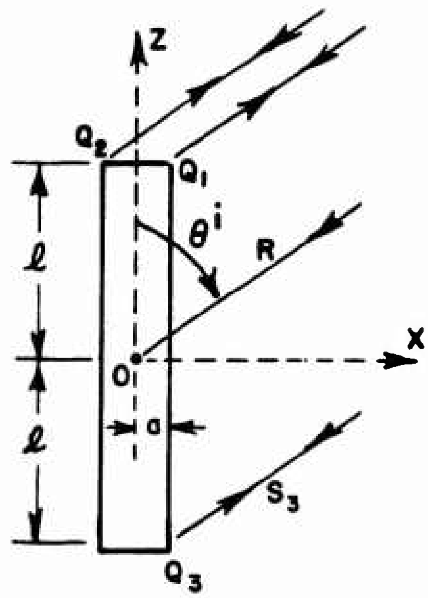

Fig. 15. Dominant rays for RCS calculation of a finite length cylinder in free-space.

III. NUMERICAL RESULTS AND DISCUSSION

In this section, numerical results are presented for the RCS of a circular cylinder on a uniform impedance surface (whose surface impedance = Z_S)as in Fig. 1. The RCS for the soft case (i.e., the case for which the incident electric field is parallel to the edge of the truncated cylinder in the x-z plane) is denoted by σ_s, whereas the RCS for the hard case (i.e., the case for which the incident electric field is perpendicular to the edge of the cylinder in the x-z plane) is denoted by σ_h. Both, σ_s and σ_h are presented as a function of the angle of arrival θ^i of the incident plane wave; the range of θ^i chosen in these calculations corresponds to $25° < \theta^i < 88°$. Numerical results for $\sigma_{\substack{s\\h}}$ are presented at selected frequencies, namely at 1, 2, 4, 8 and 16 GHz, respectively, in Figs. 16-25 for the case ℓ = 0.5 meter, and in Figs. 26-33 for the case ℓ = 1 meter; here ℓ = length of the cylinder. Furthermore, the values of $\sigma_{\substack{s\\h}}$ are compared against $\tilde{\sigma}_s$, where $\tilde{\sigma}_s$ and $\tilde{\sigma}_h$ are the RCS of the same diameter cylinder (as in $\sigma_{\substack{s\\h}}$ calculations) of length 2ℓ in free-space (see Fig. 15); the subscripts s and h in $\tilde{\sigma}_{\substack{s\\h}}$ have the same meaning as in $\sigma_{\substack{s\\h}}$. It is noted that the diameter of the cylinder in all the cases is fixed at the same value which is chosen to be $\frac{0.5}{\pi}$ meter. The "a" part of Figs. 16-33 indicate the values of σ_s or σ_h for the RCS of the cylinder on Z_S, whereas the "b" part of these figures indicate the values of $\tilde{\sigma}_s$ or $\tilde{\sigma}_h$

for the corresponding equivalent cylinder in free space. The units of $\sigma_{\substack{s\\h}}$ and $\tilde{\sigma}_{\substack{s\\h}}$ are dB/λ^2 in these plots. The values of the reflection coefficient $R_{\substack{s\\h}}$ associated with the impedance surface are given in Figs. 5-14 (in Section II) as a function of θ^i for the selected frequencies of interest; these values of $R_{\substack{s\\h}}$ are employed in calculating $\sigma_{\substack{s\\h}}$.

Certain observations concerning the behavior of $\sigma_{\substack{s\\h}}$ and $\tilde{\sigma}_{\substack{s\\h}}$ can be be made from Figs. 16-33. It is noted in general that $\sigma_{\substack{s\\h}}$ is much higher than $\tilde{\sigma}_{\substack{s\\h}}$; thus, it is concluded that the presence of the surface impedance Z_s is to effectively increase the RCS of the cylinder over that of the "equivalent" cylinder in free space. It is also noted that $\tilde{\sigma}_h$ is generally higher than $\tilde{\sigma}_s$; in contrast, σ_s is in general very slightly higher than σ_h except near $\theta^i = 90°$. Furthermore, the behavior of $\sigma_{\substack{s\\h}}$ is very strongly governed by the behavior of the impedance surface reflection coefficient $R_{\substack{s\\h}}$. For example, R_h in Figs. 10-13 indicates a suddent dip in amplitude around $\theta^i = 85°$; this effect is also manifested in the plots of σ_h which show a significant dip near $\theta^i = 85°$. Of course, σ_h increases on either side of this dip (near $\theta^i = 85°$). On the other hand, σ_s is generally very slightly higher than σ_h except for θ^i near 90° where σ_s decreases significantly. Since the value of σ_s is calculated over $25° < \theta^i < 88°$, the significant decrease in σ_s for θ^i near 90° is not apparent in the present plots for the higher frequencies; it is believed that this is due to the fact that at these higher frequencies σ_s decreases significantly only for θ^i extremely close to 90°, i.e., in the range $88° < \theta^i < 90°$ which is excluded in the present calculations. The values of σ_s and σ_h in general show a rapid, but very small size fluctuation at the higher frequencies; in fact, σ_s and σ_h tend to be fairly constant over $25° < \theta^i < 88°$ at the higher frequencies except near $\theta^i = 85°$ for σ_h and near $\theta^i = 90°$ for σ_s, respectively. In contrast, $\tilde{\sigma}_{\substack{s\\h}}$ indicates higher size fluctuations which of course become more rapid at the higher frequencies as one might expect from GTD considerations. Finally, the levels of σ_s, σ_h, $\tilde{\sigma}_s$ and $\tilde{\sigma}_h$ increase with increase in frequency in each case, since the electrical surface area of the scatterer effectively increases with increase in frequency of the incident plane wave.

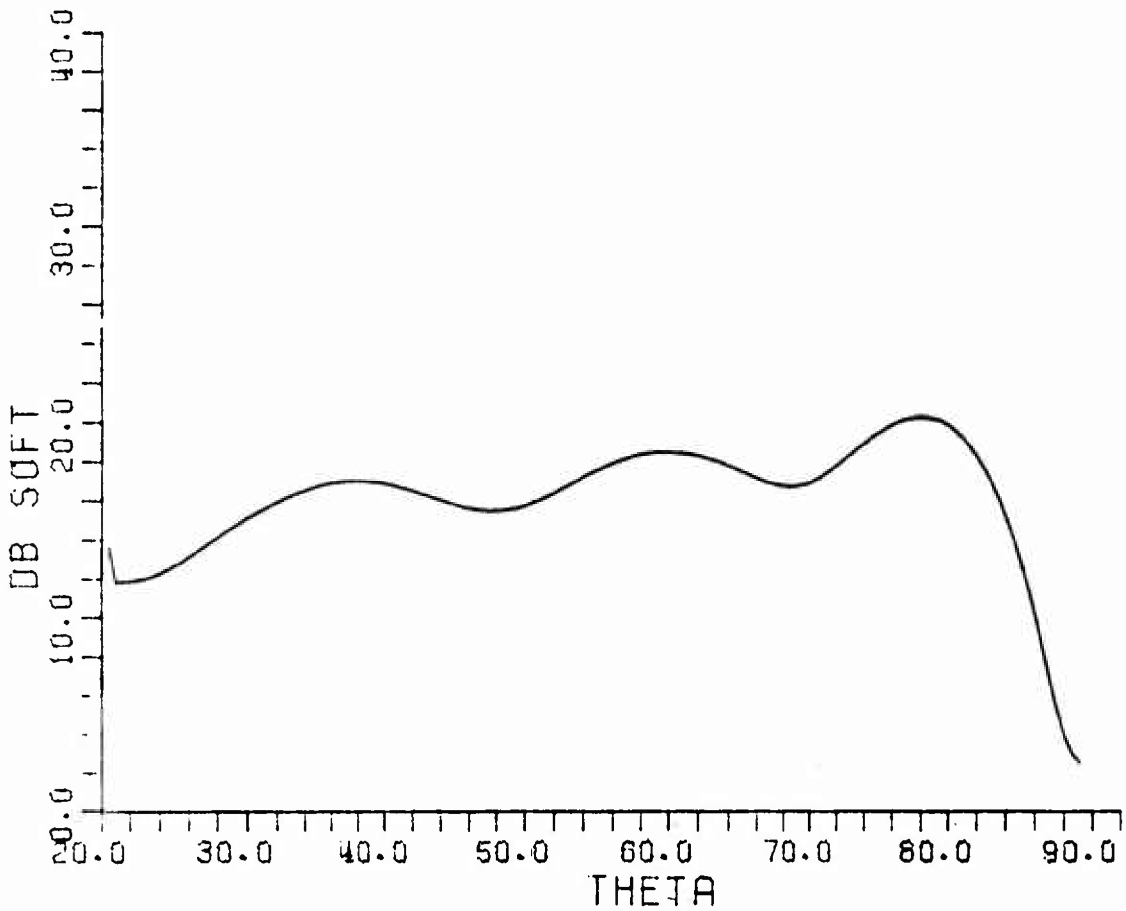

Fig. (16a). (σ_s/λ^2) in dB vs θ^i = THETA in degrees at f = 1 GHz, and ℓ = .5 m.

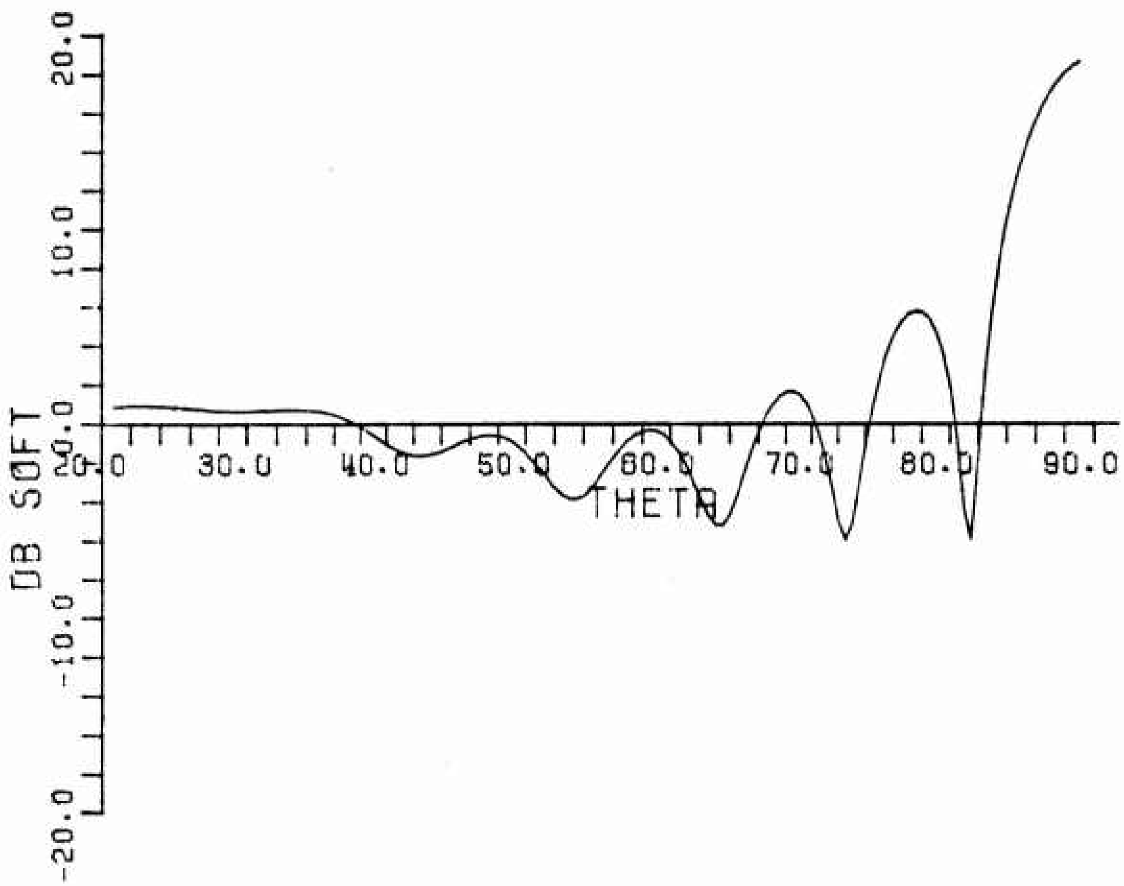

Fig. (16b). $(\tilde{\sigma}_s/\lambda^2)$ in dB vs θ^i = THETA in degrees at f = 1 GHz, and ℓ = .5 m.

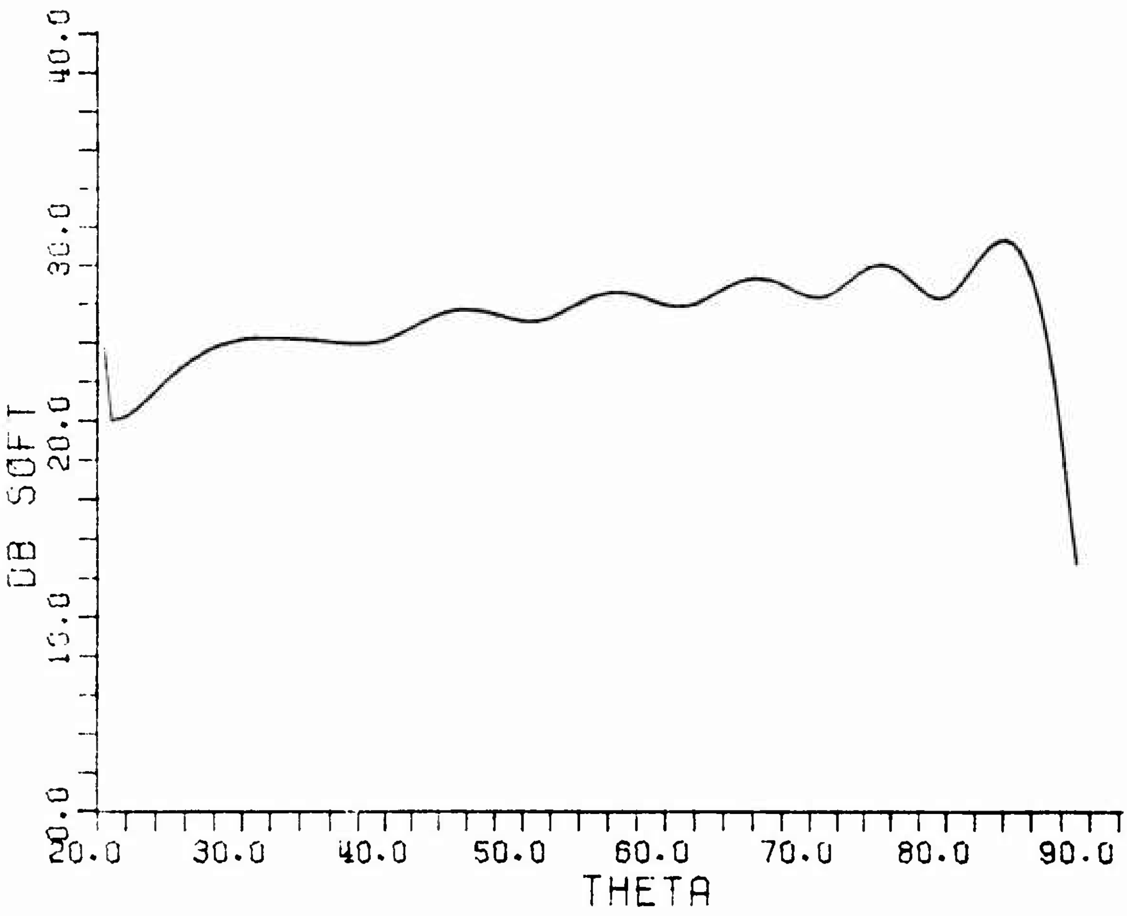

Fig. (17a). (σ_S/λ^2) in dB vs θ^i at f = 2 GHz, and ℓ = .5 m.

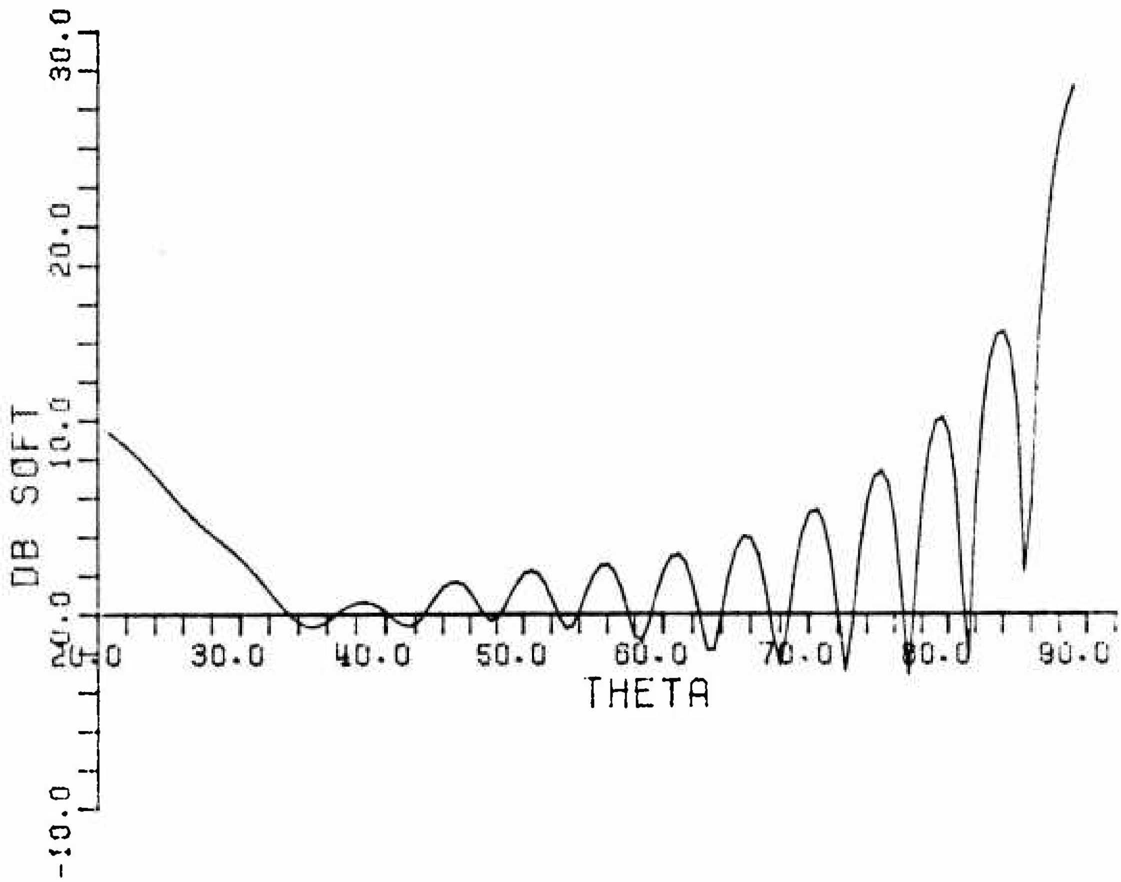

Fig. (17b). (σ_s/λ^2) in dB vs θ^i at f = 2 GHz, and λ = .5 m.

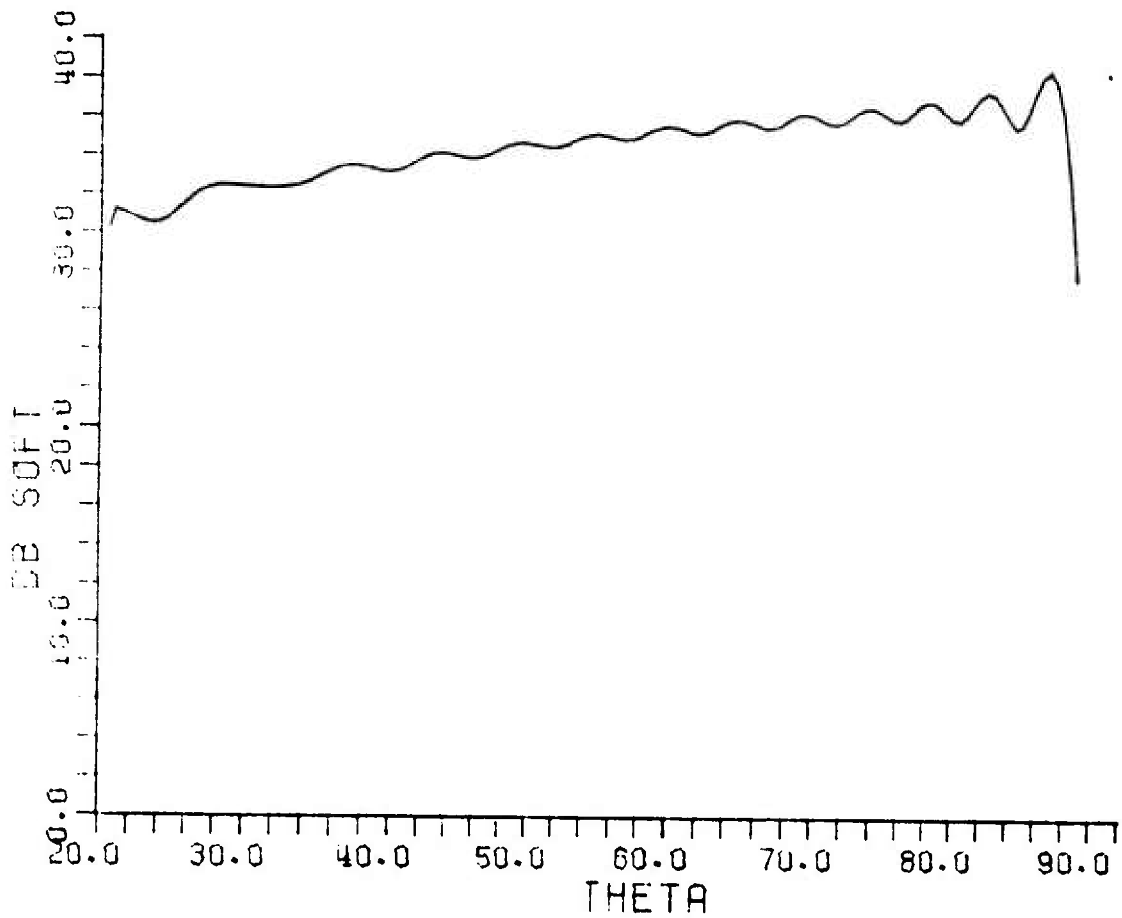

Fig. (18a). (σ_s/λ^2) in dB vs θ^i at f = 4 GHz, and ℓ = .5 m.

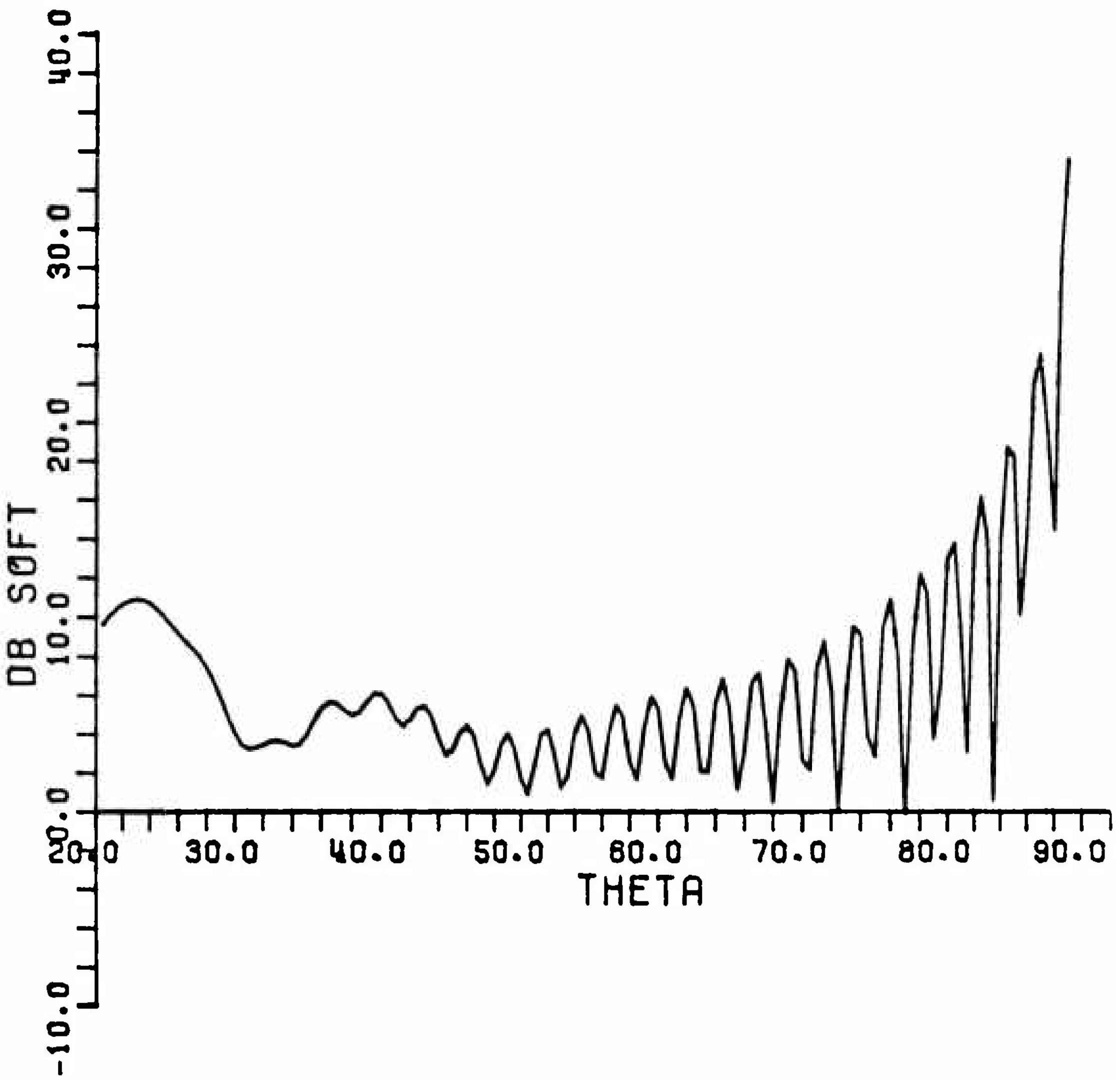

Fig. (18b). (σ_s/λ^2) in dB vs θ^i at f = 4 GHz, and ℓ = .5 m.

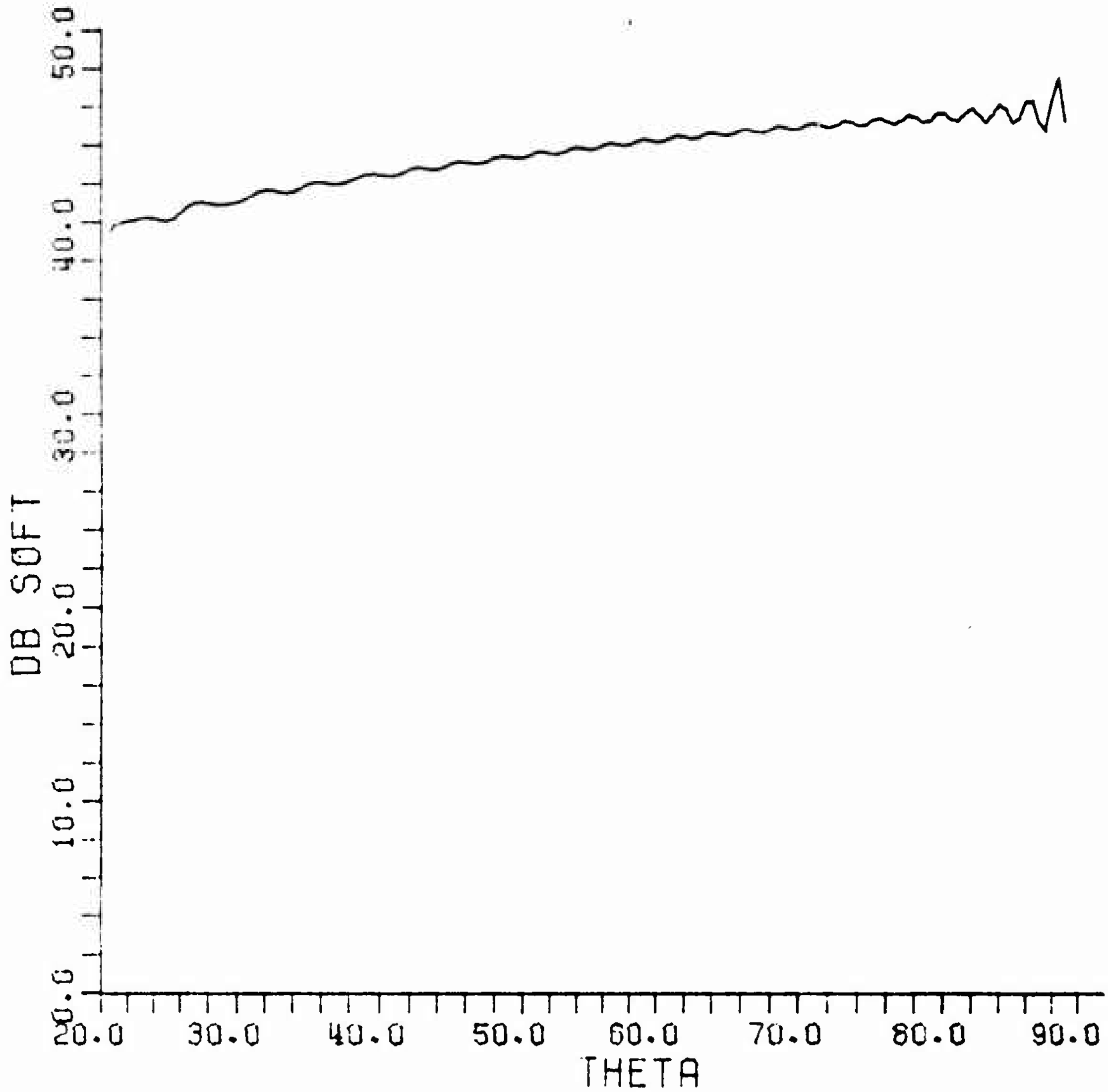

Fig. (19a). (σ_s/λ^2) in dB vs θ^i at f = 8 GHz,
and ℓ = .5 m.

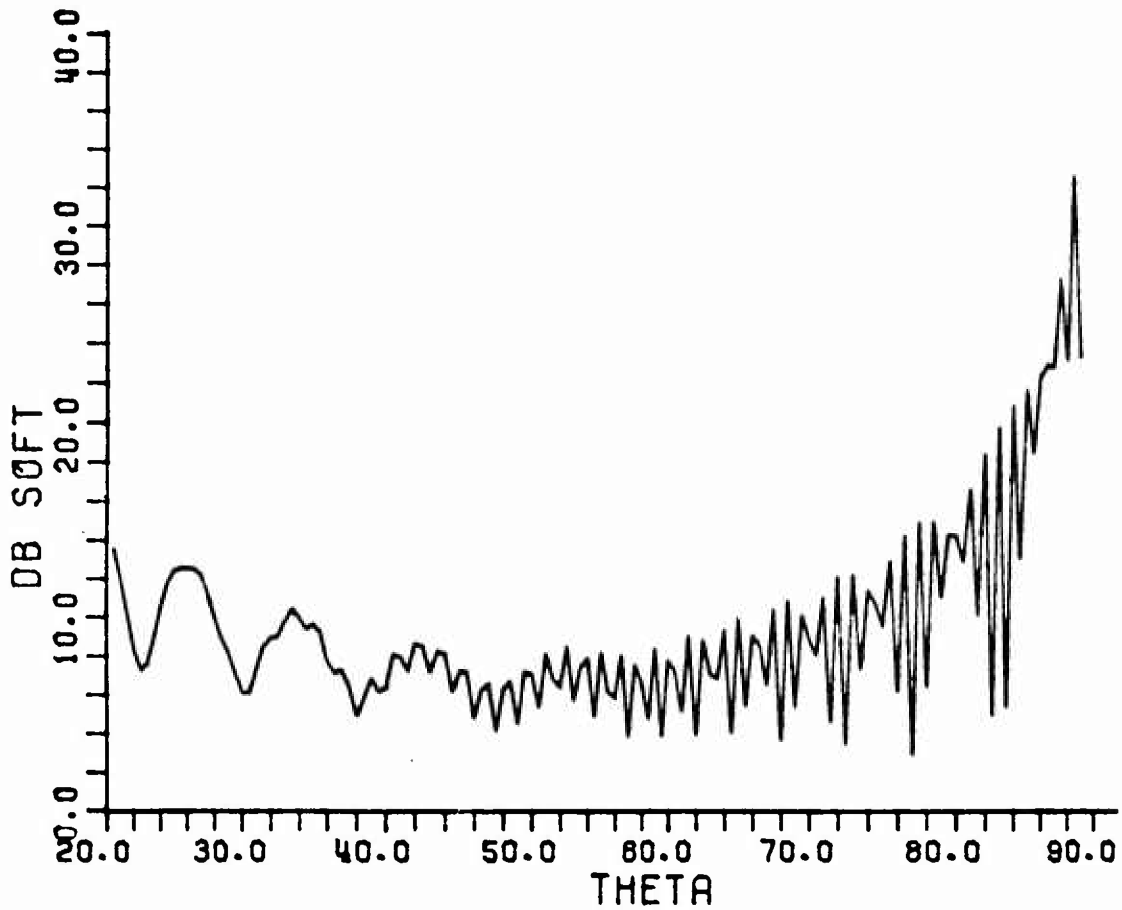

Fig. (19b). $(\tilde{\sigma}_s/\lambda^2)$ in dB vs θ^i at f = 8 GHz, and ℓ = .5 m.

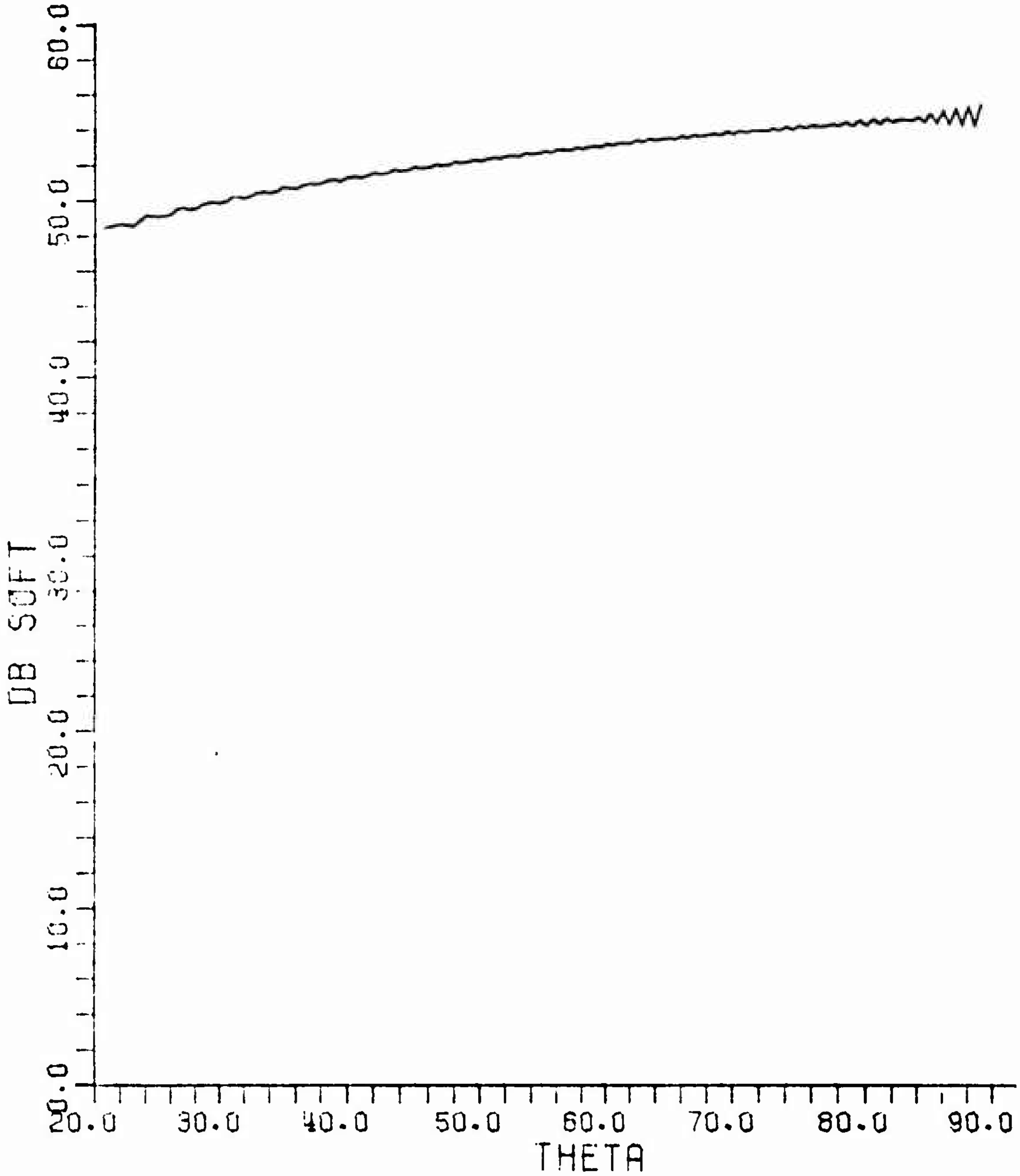

Fig. (20a). (σ_s/λ^2) in dB vs θ^i at f = 16 GHz, and ℓ = .5 m.

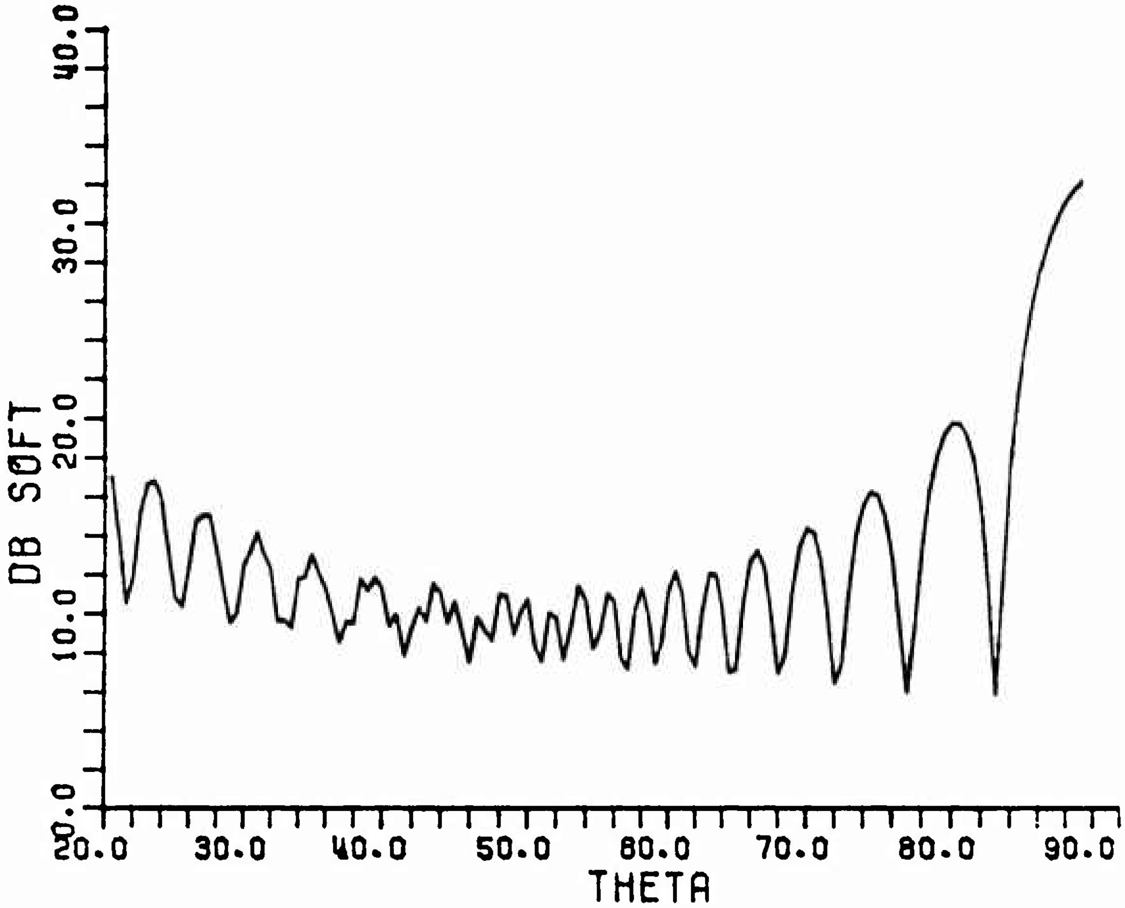

Fig. (20b). $(\tilde{\sigma}_s/\lambda^2)$ in dB vs θ^i at f = 16 GHz, and ℓ = .5 m.

(Note: only the average level but not the detail are to be inferred from this curve since the sampling interval chosen for θ^i is not small enough for indicating detailed variations in σ_s at 16 GHz.)

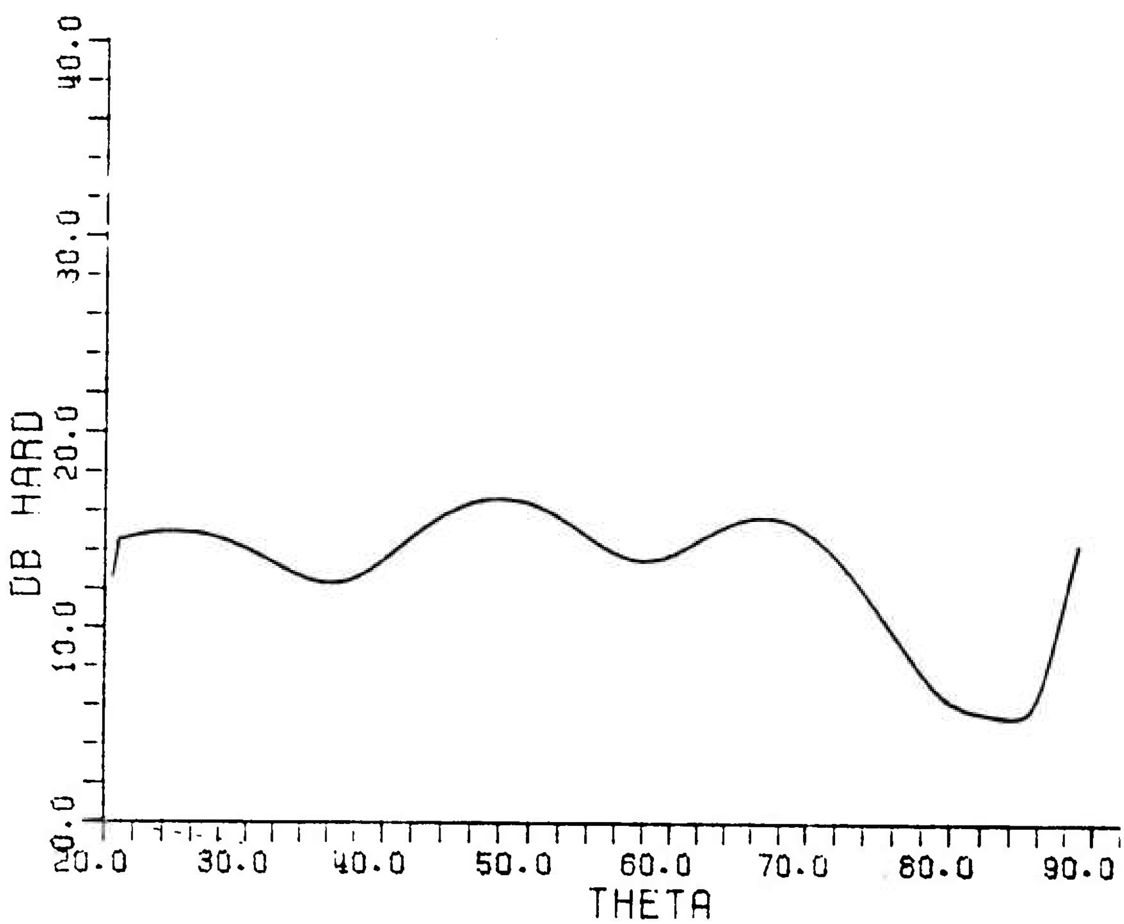

Fig. (21a). (σ_h/λ^2) in dB vs θ^i = THETA in degrees at f = 1 GHz, and ℓ = .5 m.

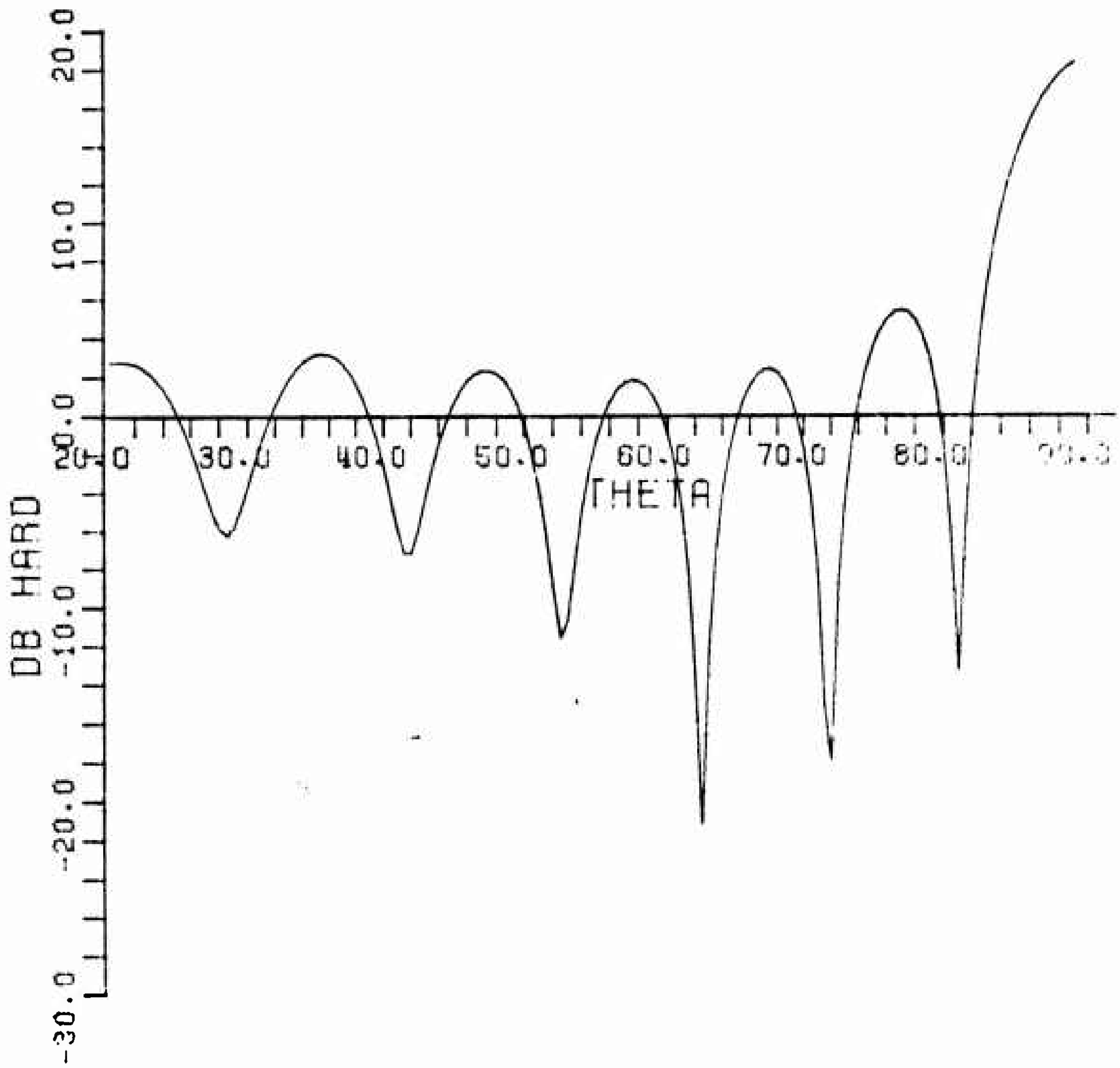

Fig. (21b). $(\tilde{\sigma}_h/\lambda^2)$ in dB vs θ^i = THETA in degrees at $f = 1$ GHz and $\ell = .5$ m.

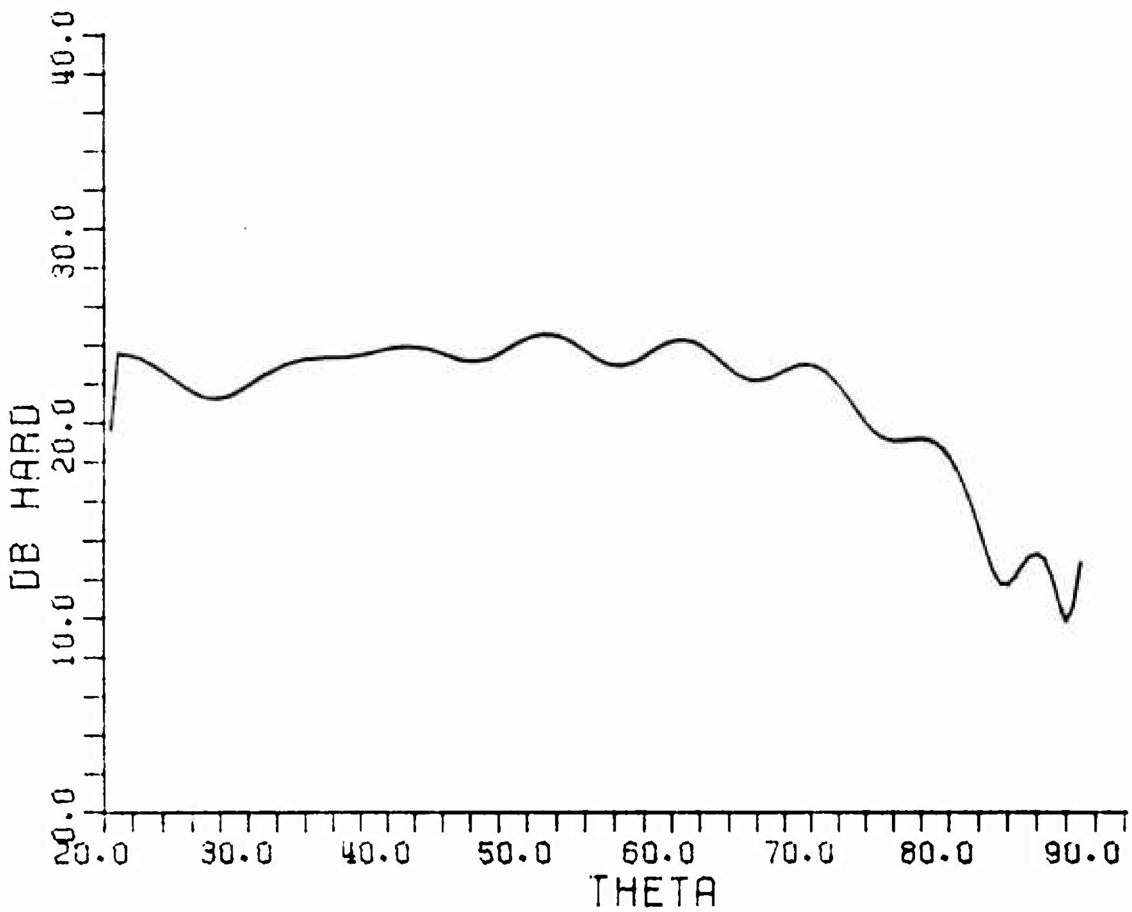

Fig. (22a). (σ_h/λ^2) in dB vs θ^i at f = 2 GHz, and ℓ = .5 m.

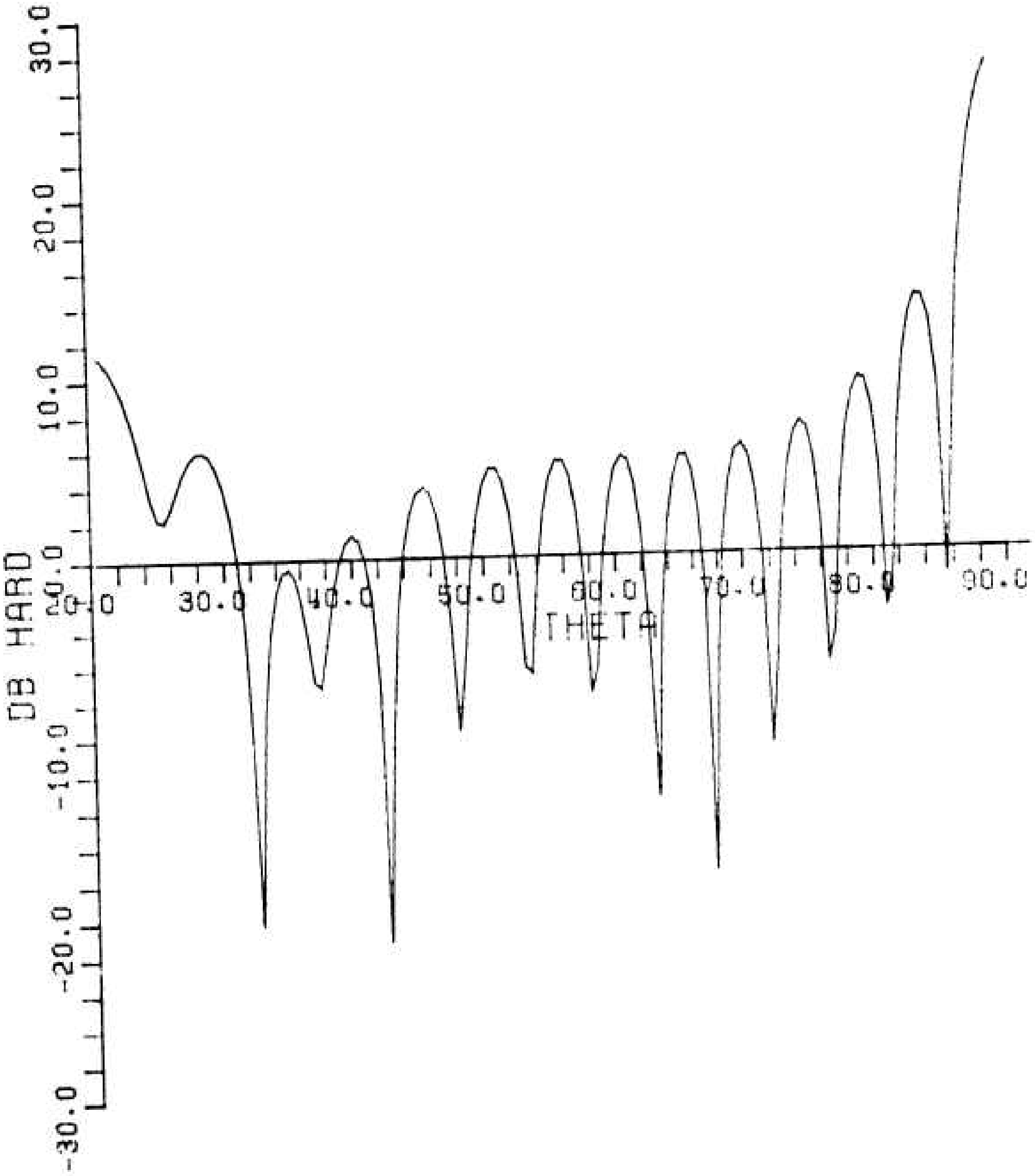

Fig. (22b). $(\tilde{\sigma}_h/\lambda^2)$ in dB vs θ^i at f = 2 GHz, and ℓ = .5 m.

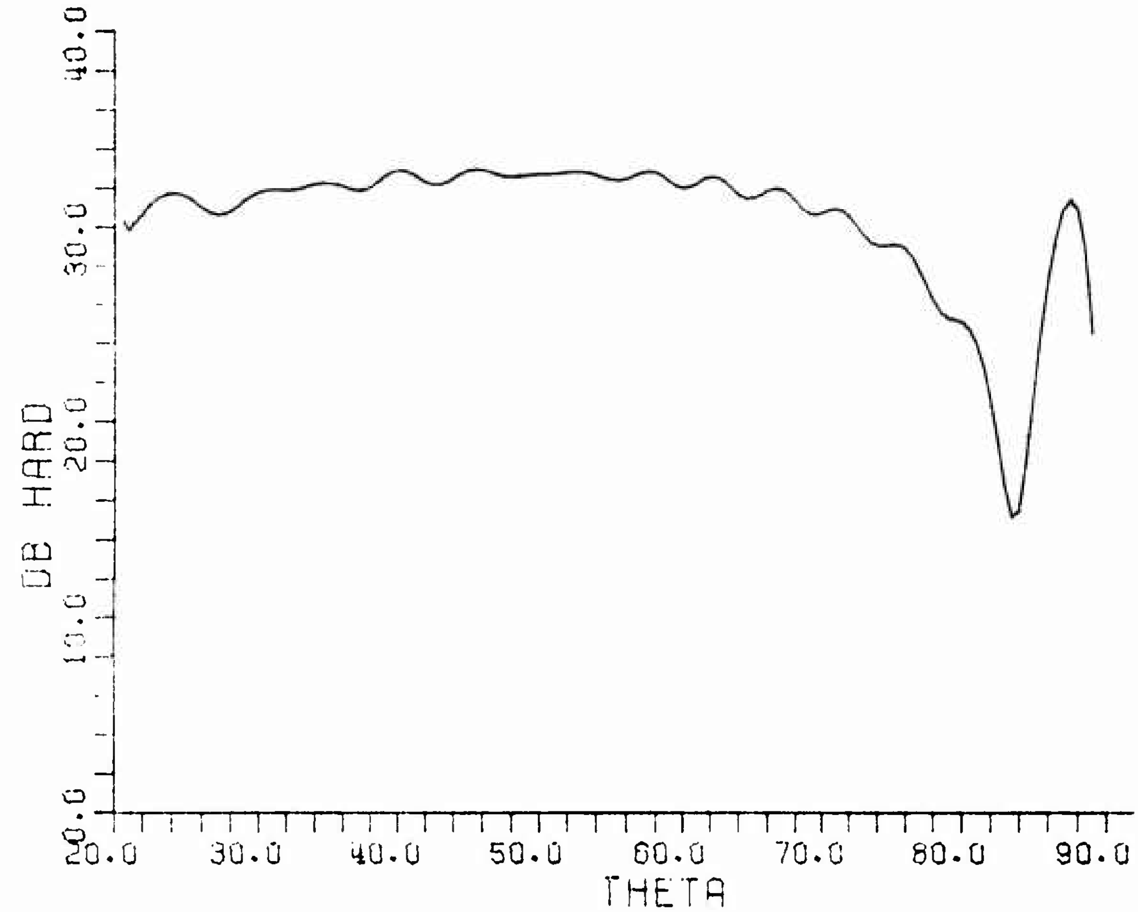

Fig. (23a). (σ_h/λ^2) in dB vs θ^i at f = 4 GHz, and ℓ = .5 m.

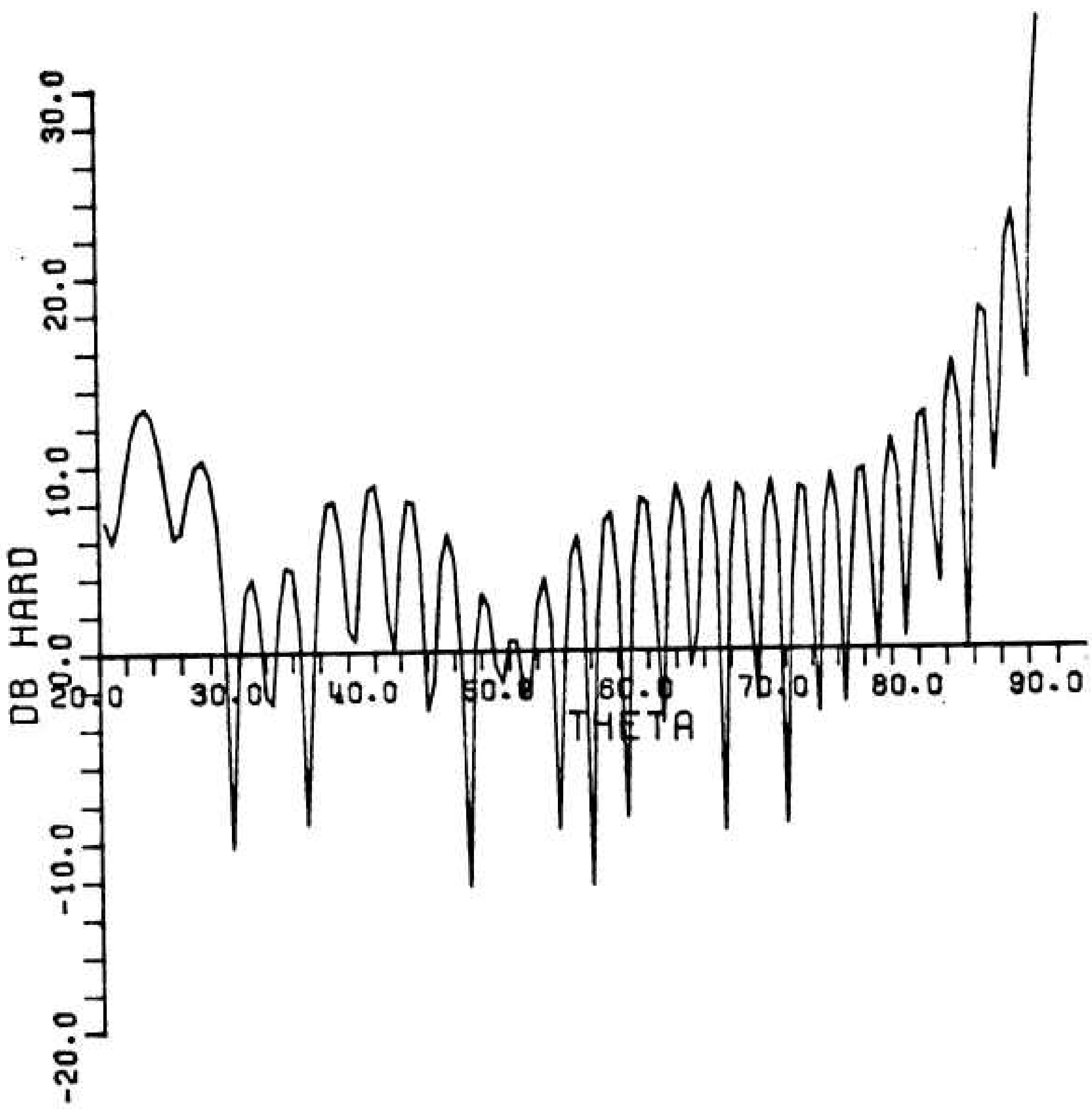

Fig. (23b). $(\tilde{\sigma}_h/\lambda^2)$ in dB vs θ^i at f = 4 GHz, and ℓ = .5 m.

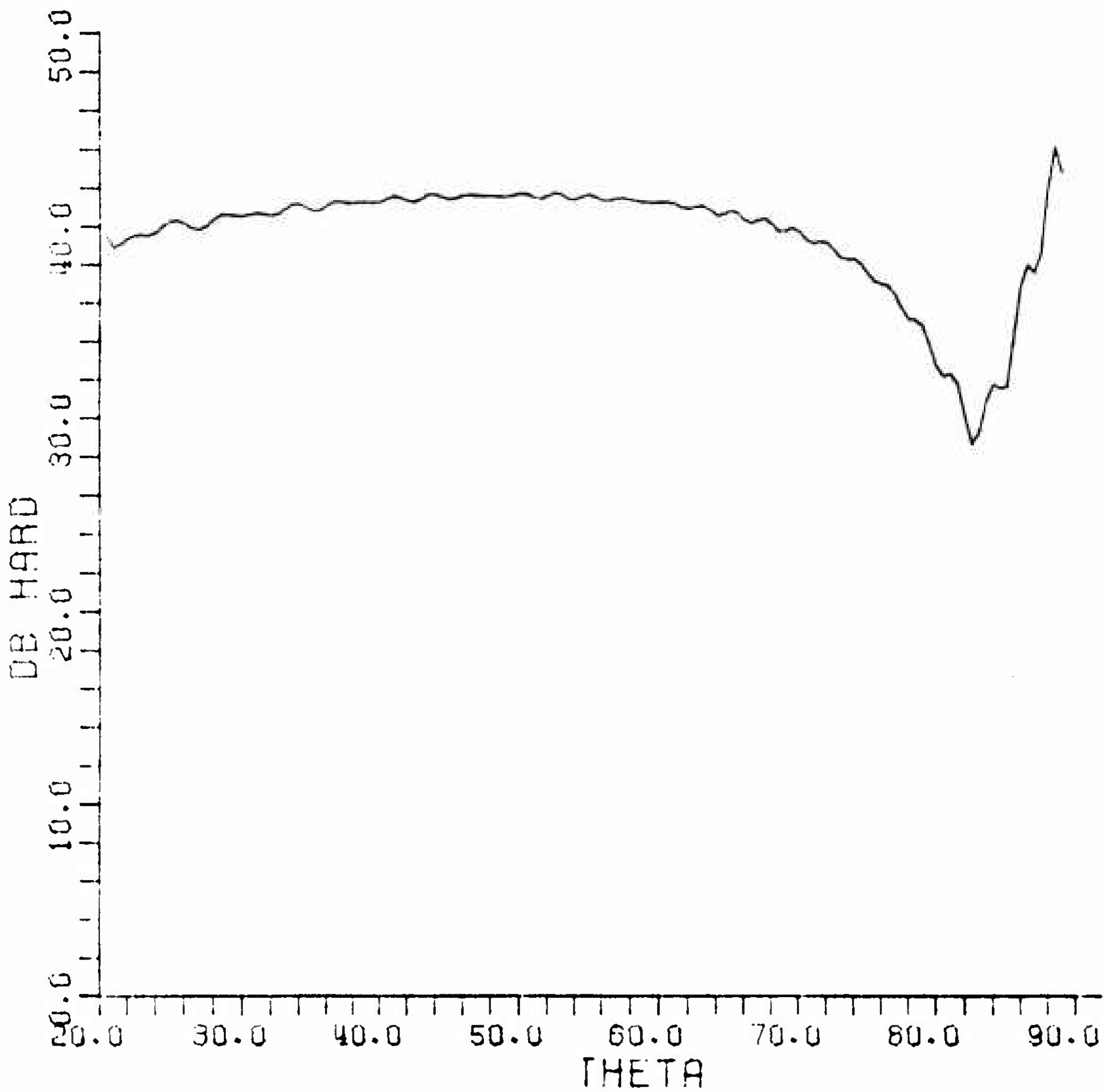

Fig. (24a). (σ_h/λ^2) in dB vs θ^i at f = 8 GHz and ℓ = .5 m.

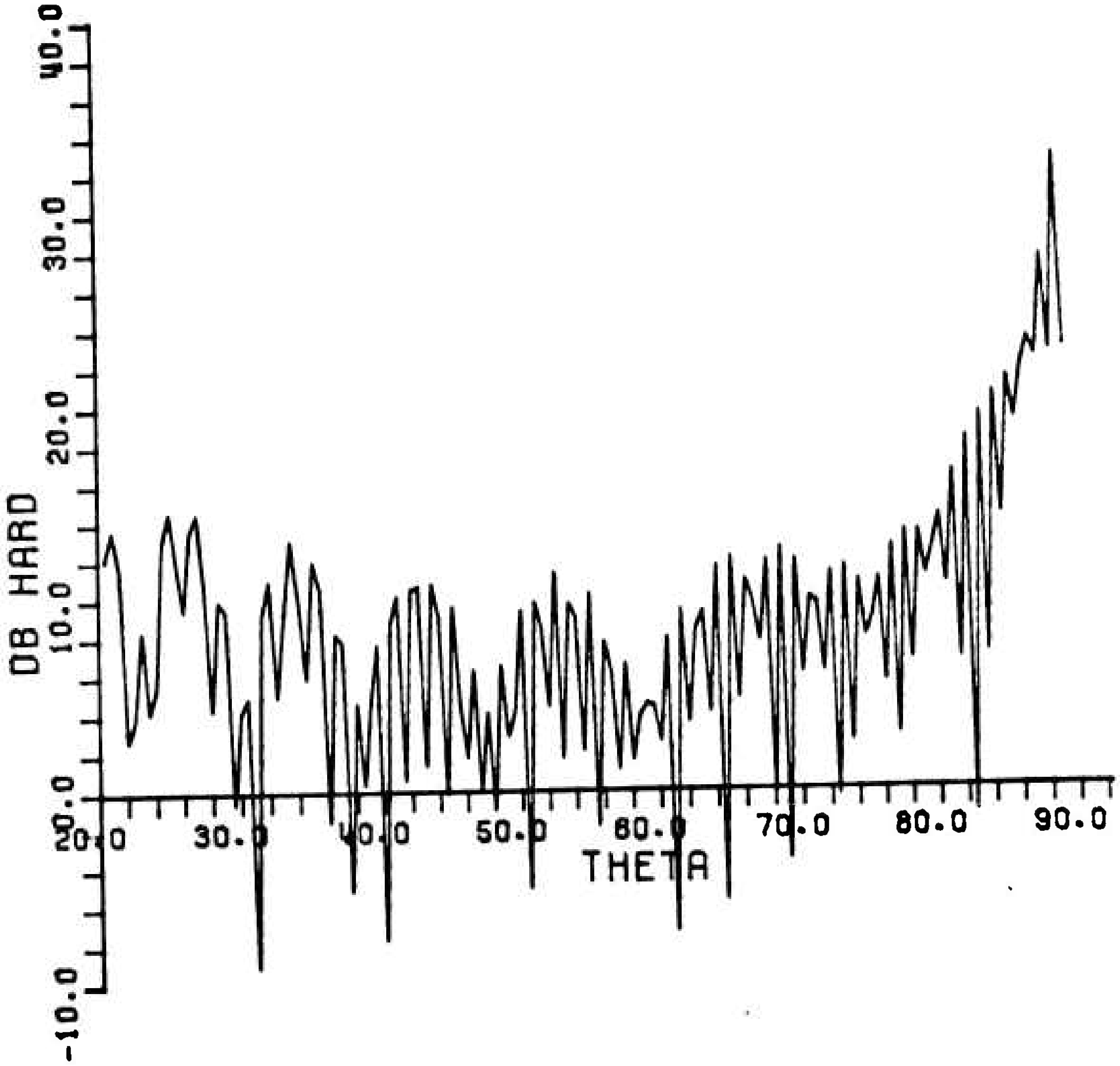

Fig. (24b). $(\tilde{\sigma}_h/\lambda^2)$ in dB vs θ^i at f = 8 GHz, and ℓ = .5 m.

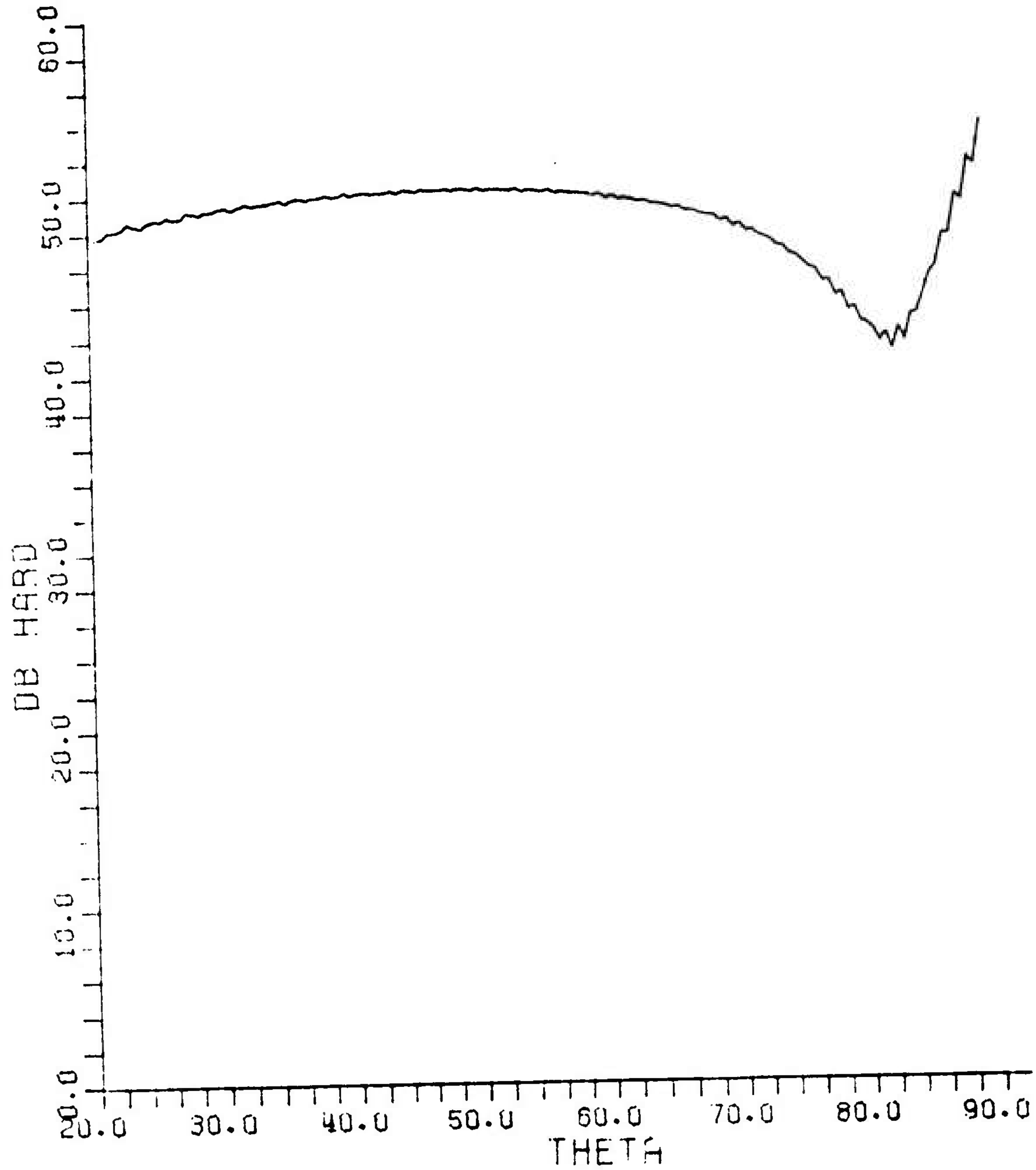

Fig. (25a). (σ_h/λ^2) in dB vs θ^i at f = 16 GHz, and ℓ = .5 m.

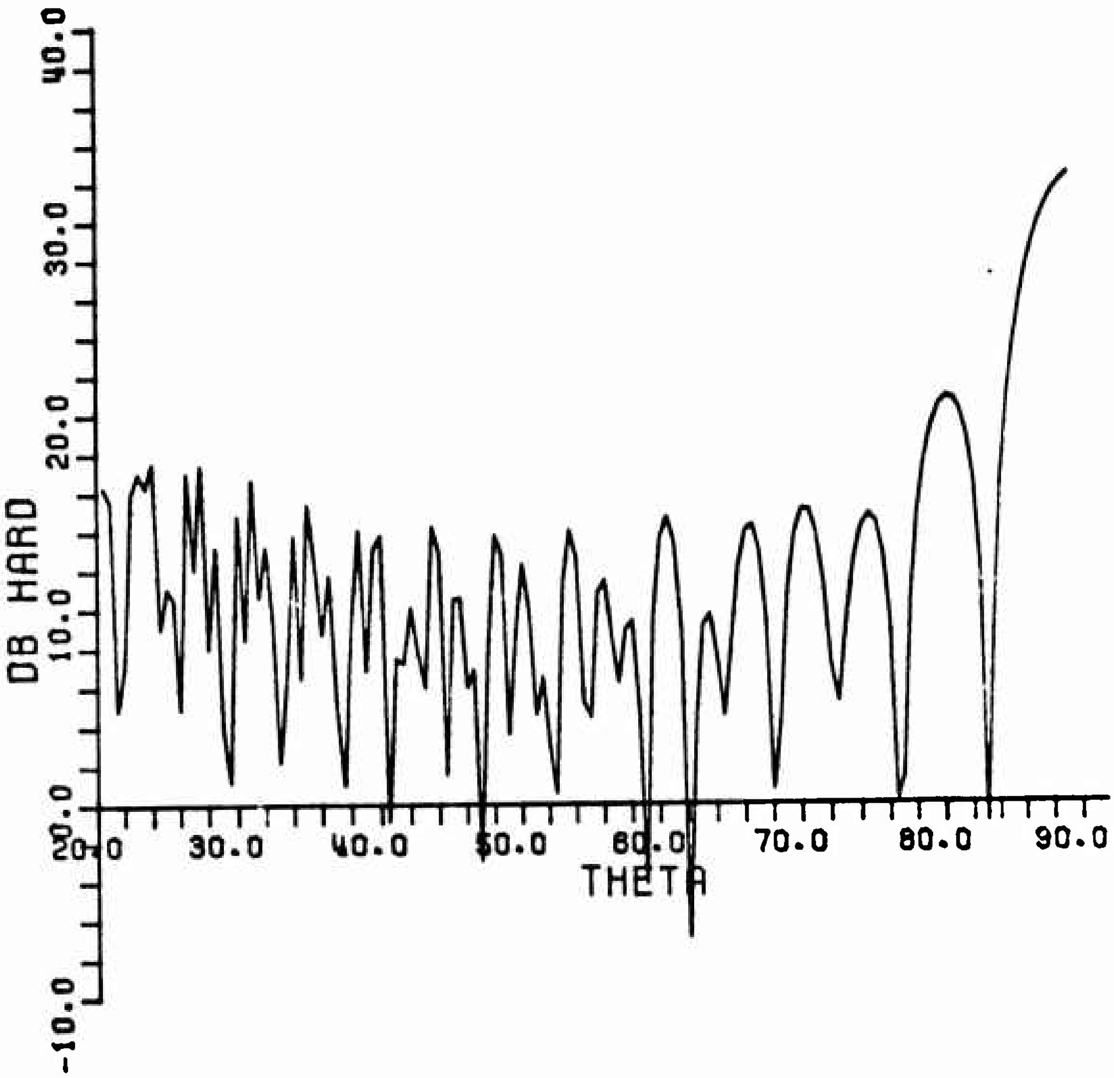

Fig. (25b). $(\tilde{\sigma}_h/\lambda^2)$ in dB vs θ^i at f = 16 GHz, and ℓ = .5 m.

(Note: only the average level but not the detail are to be inferred from this curve since the sampling interval chosen for θ^i is not small enough for indicating detailed variation in $\tilde{\sigma}_h$ at 16 GHz.)

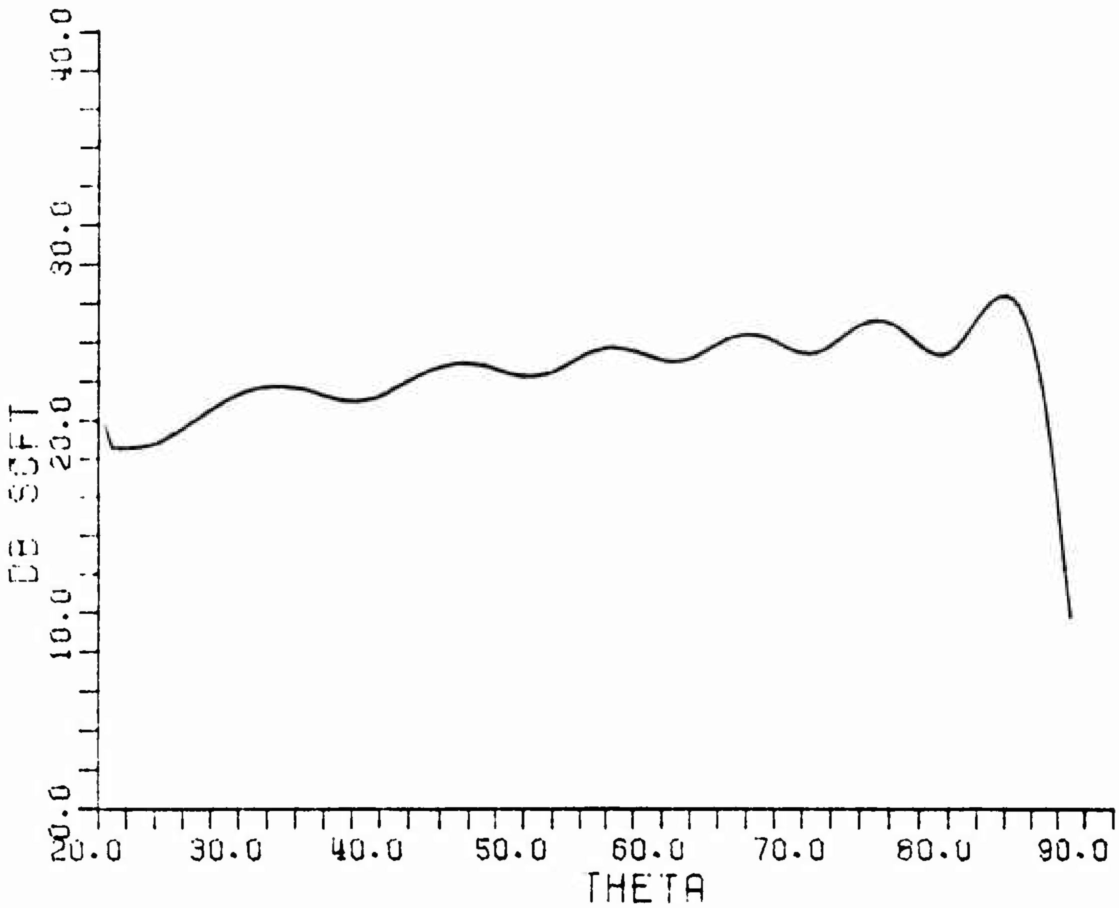

Fig. (26a). (σ_s/λ^2) in dB vs θ^i at f = 1 GHz and ℓ = 1 m.

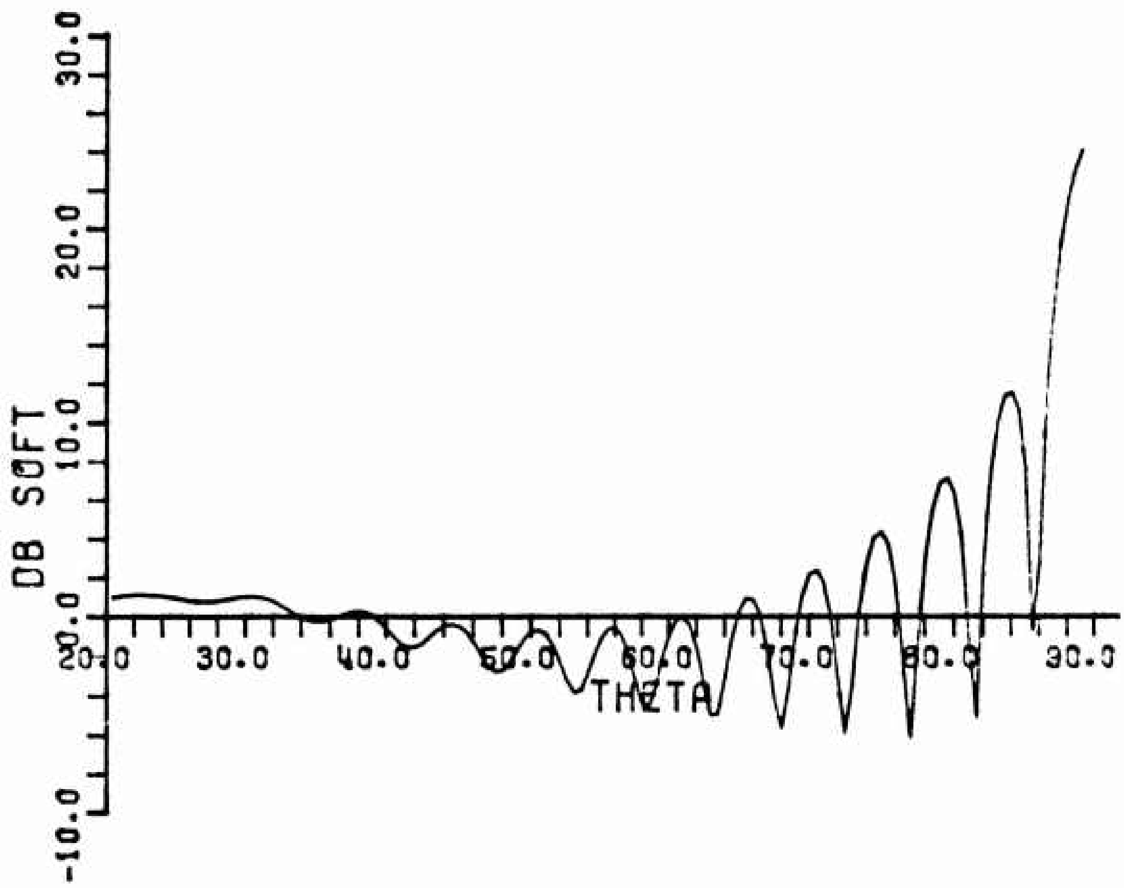

Fig. (26b). $(\tilde{\sigma}_S/\lambda^2)$ in dB vs θ^i at f = 1 GHz and ℓ = 1 m.

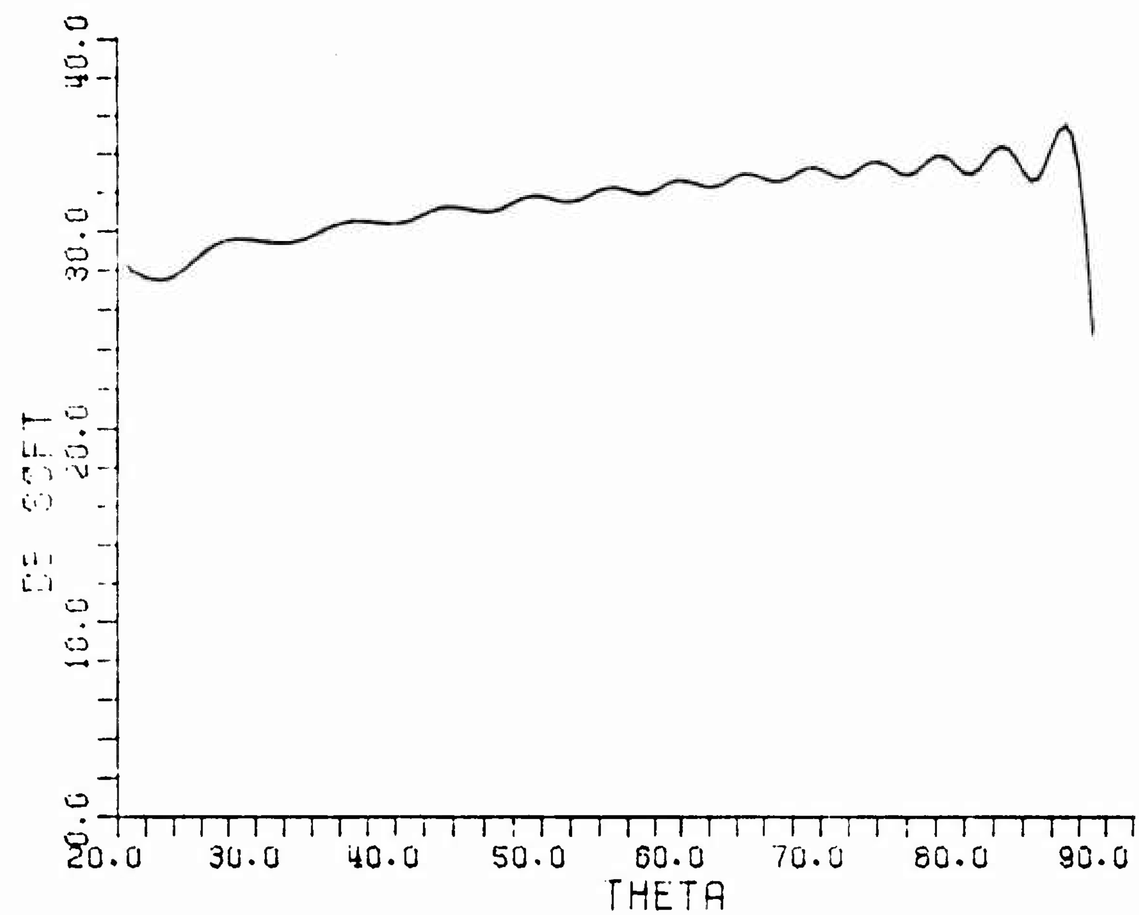

Fig. (27a). (σ_s/λ^2) in dB vs θ^i at f = 2 GHz, and ℓ = 1 m.

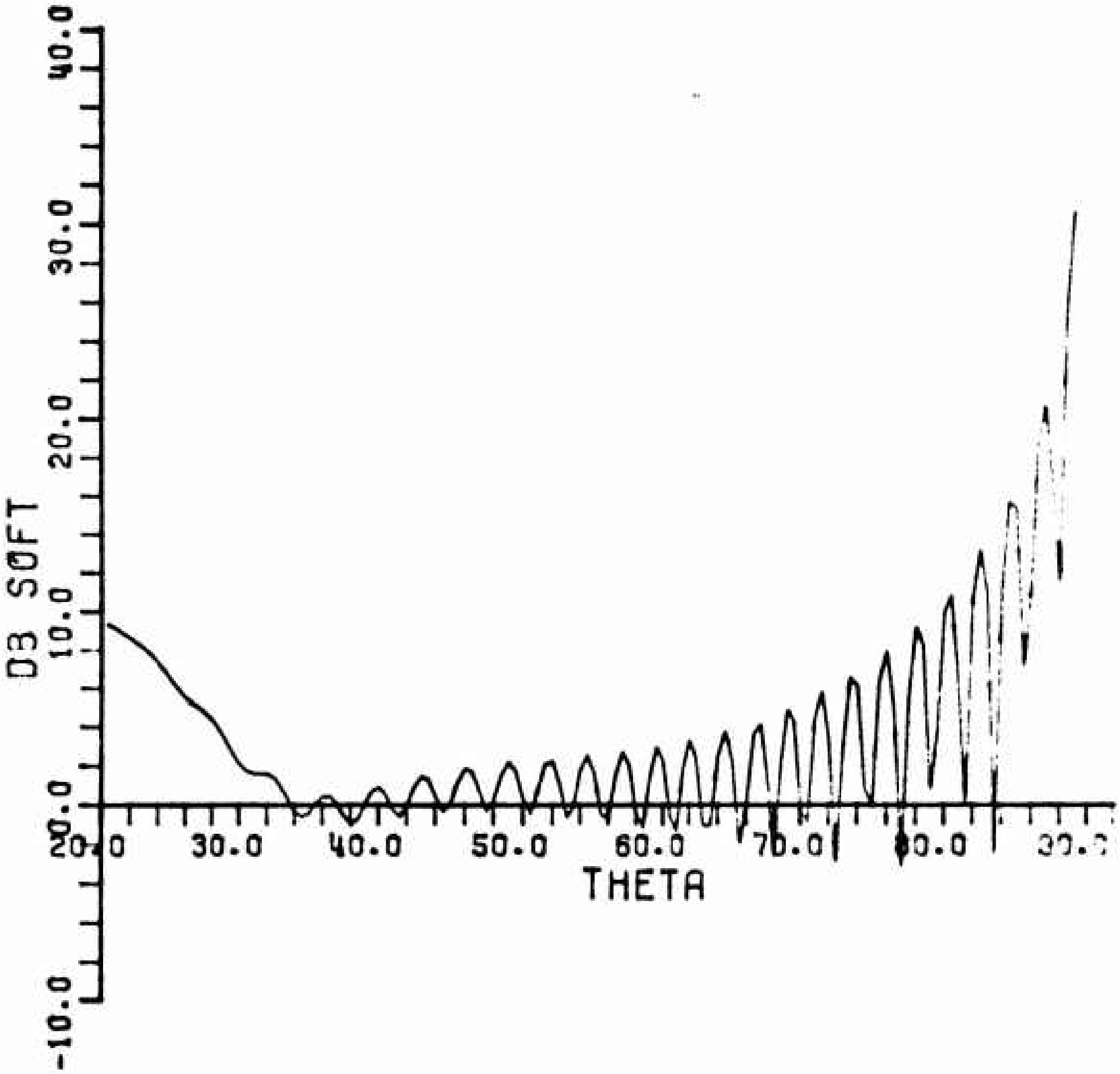

Fig. (27b). $(\tilde{\sigma}_s/\lambda^2)$ in dB vs θ^i at f = 2 GHz, and ℓ = 1 m.

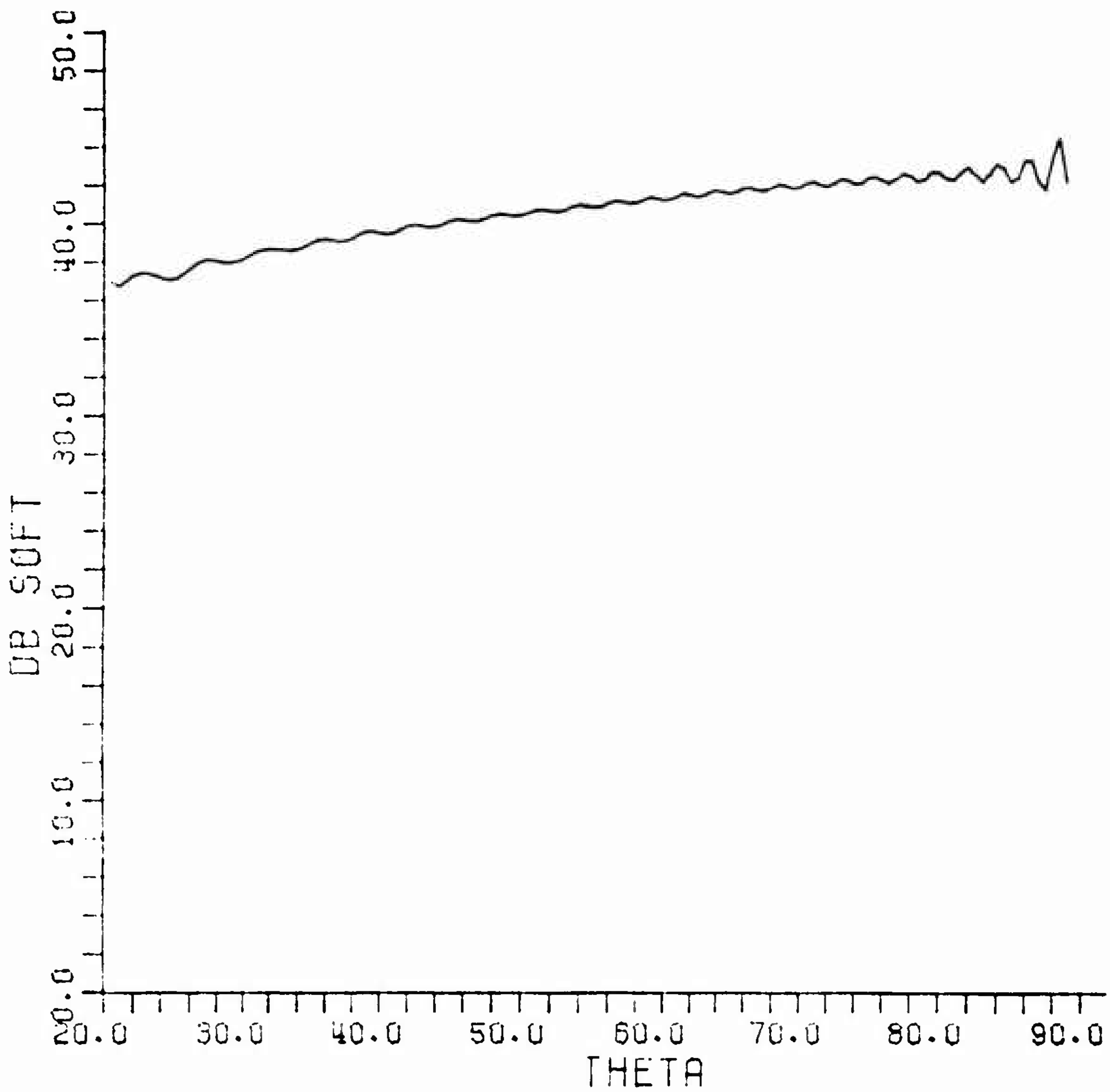

Fig. (28a). (σ_s/λ^2) in dB vs θ^i at f = 4 GHz, and ℓ = 1 m.

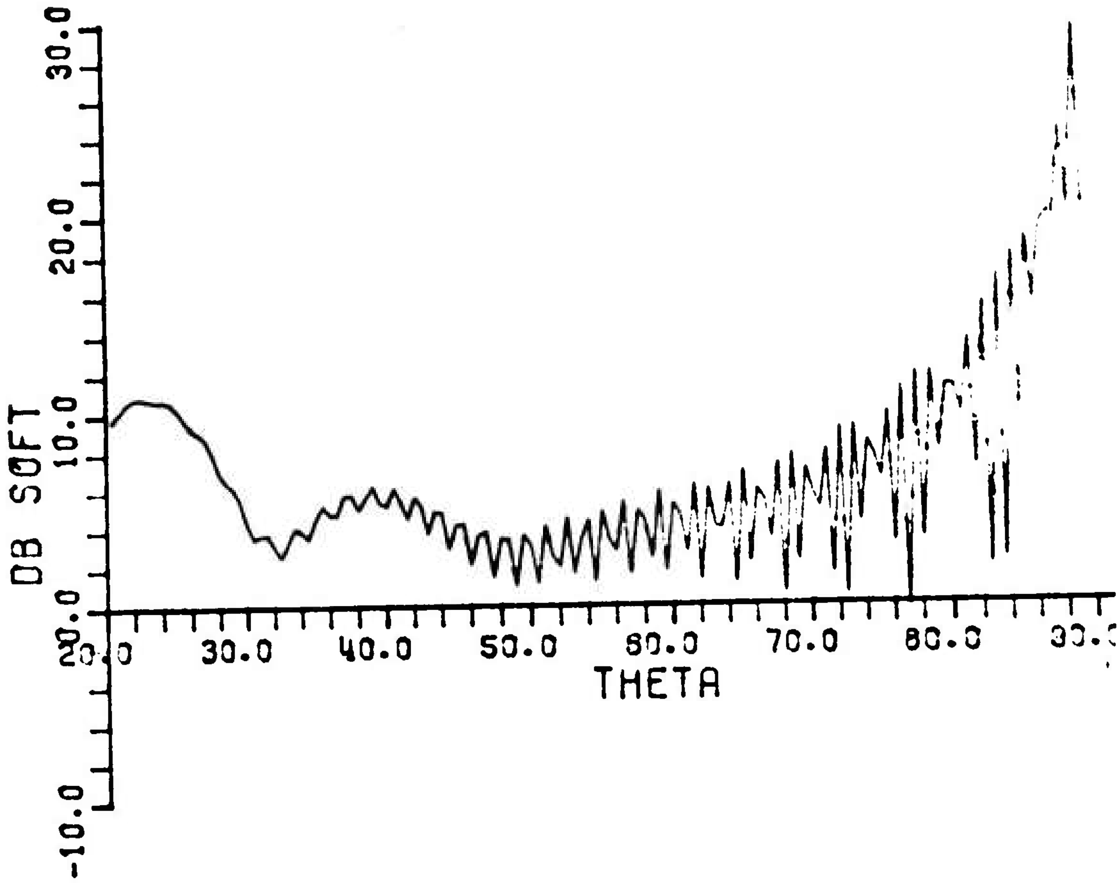

Fig. (28b). $(\tilde{\sigma}_s/\lambda^2)$ in dB vs θ^i at f = 4 GHz, and ℓ = 1 m.

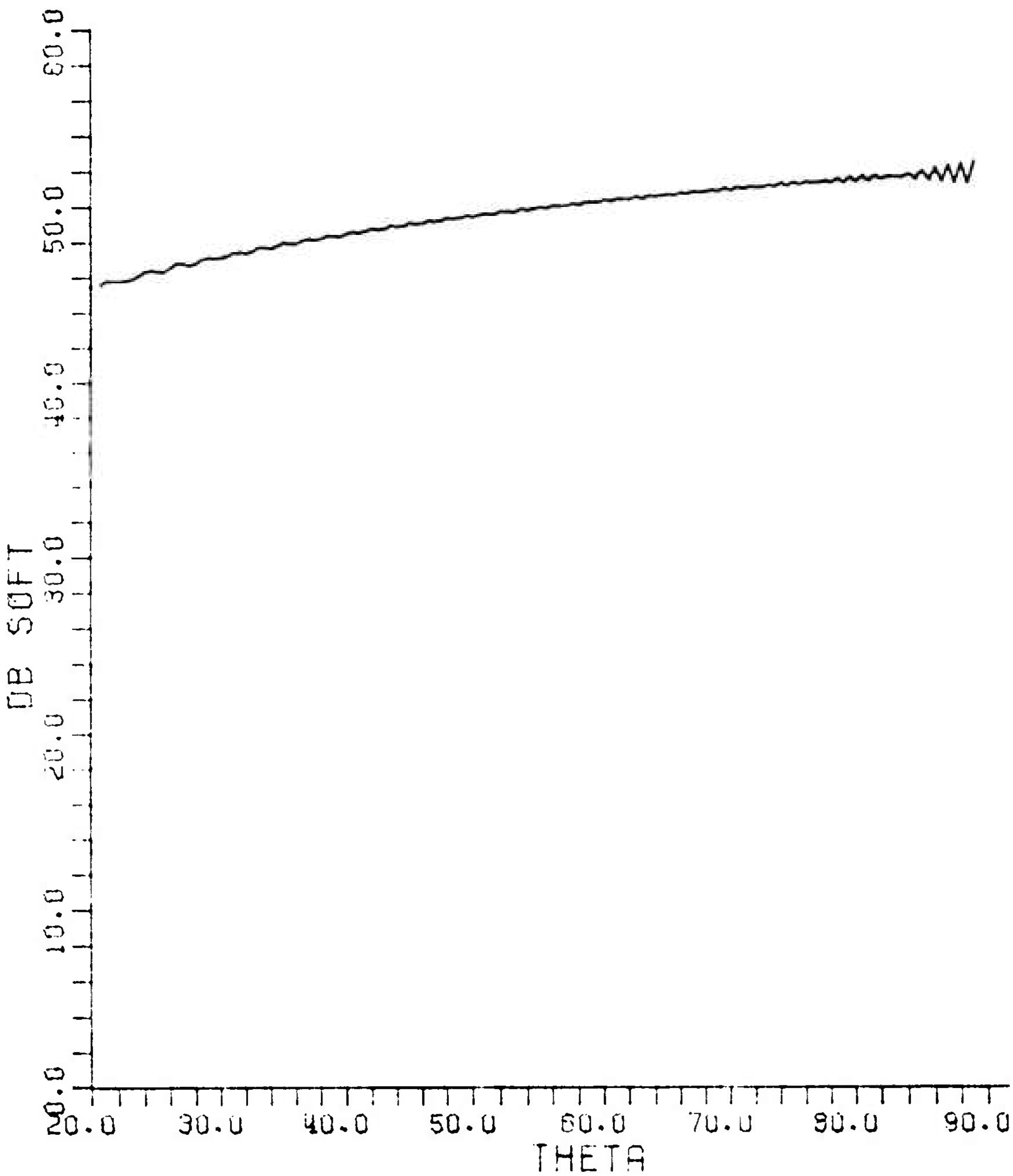

Fig. (29). (σ_S/λ^2) in dB vs θ^i at f = 8 GHz, and ℓ = 1 m.

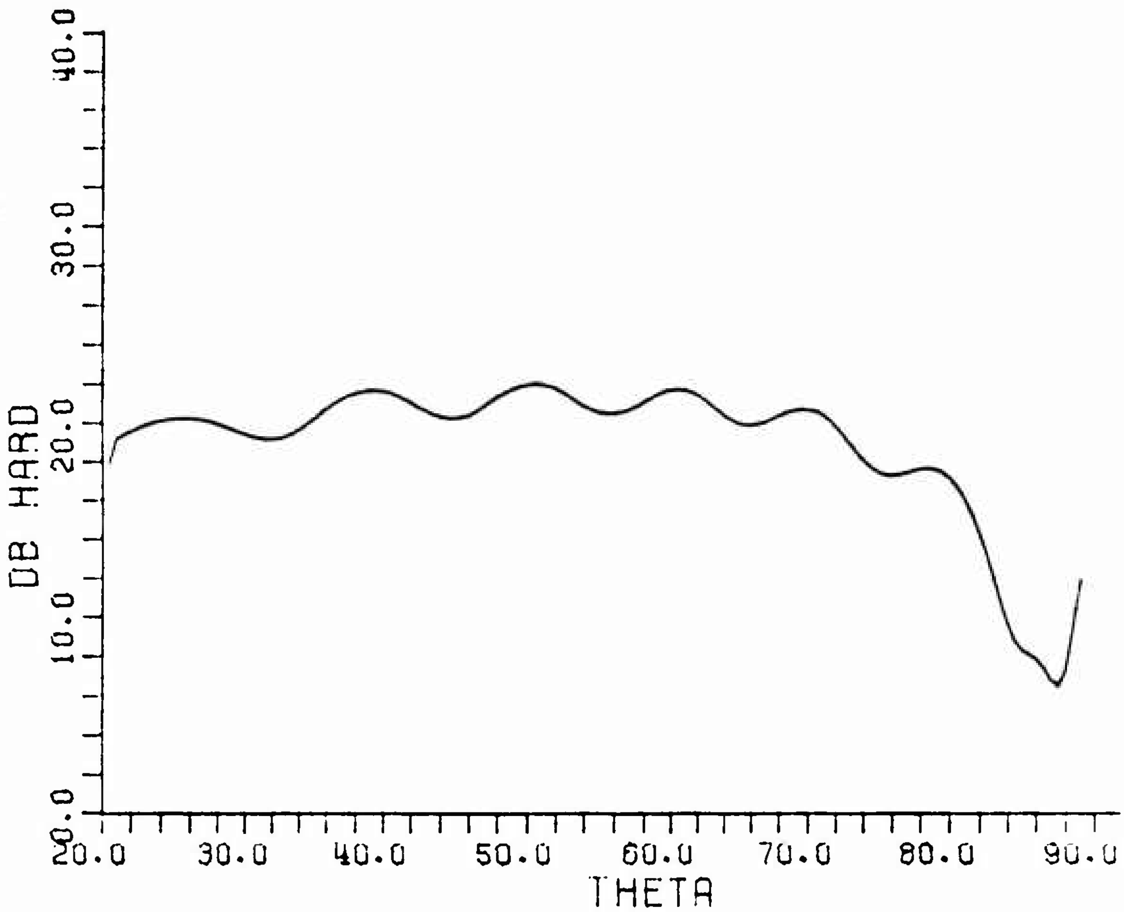

Fig. (30a). (σ_h/λ^2) in dB vs θ^i at f = 1 GHz, and ℓ = 1 m.

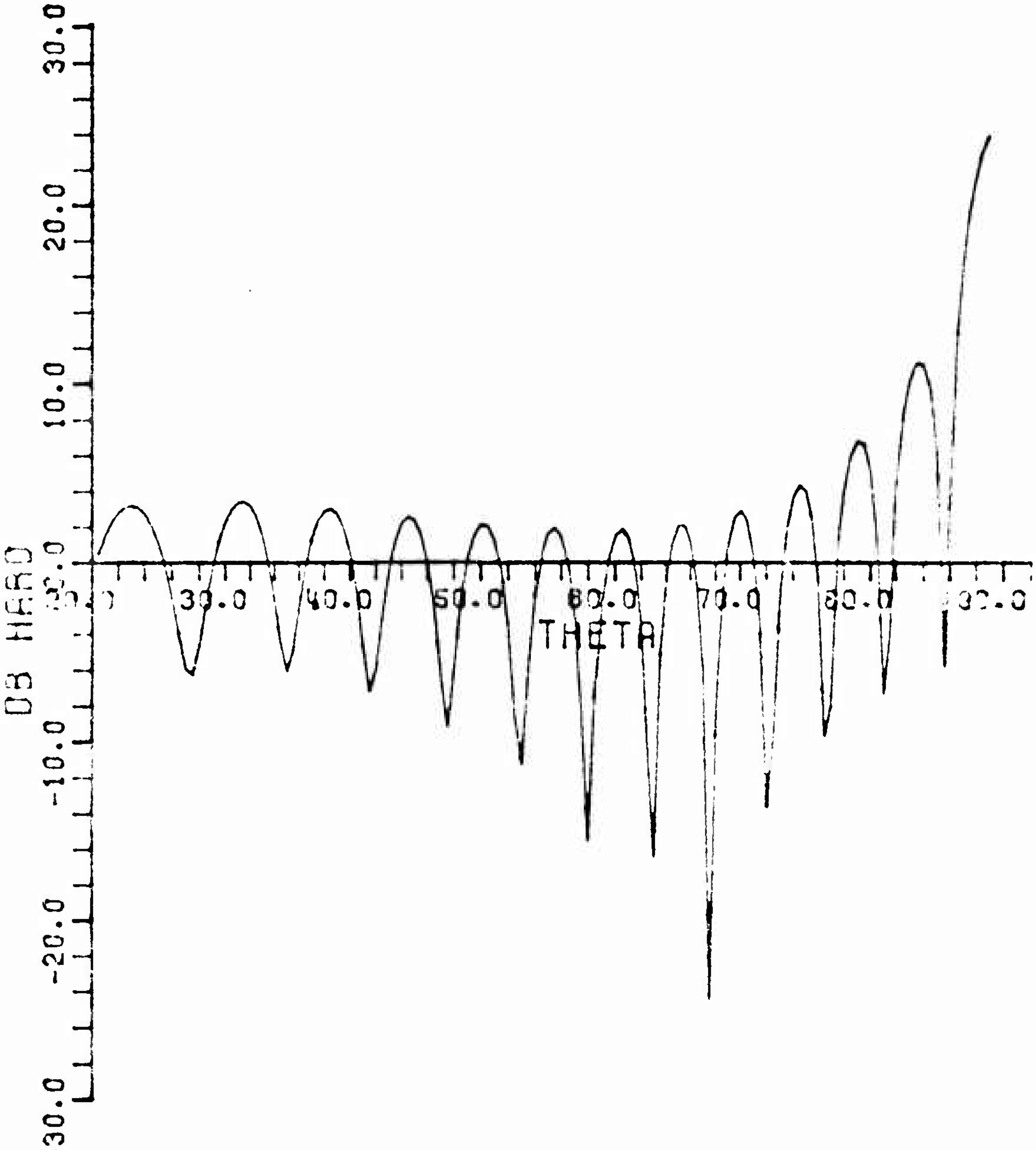

Fig. (30b). (σ_h/λ^2) in dB vs θ^i at f = 1 GHz, and ℓ = 1 m.

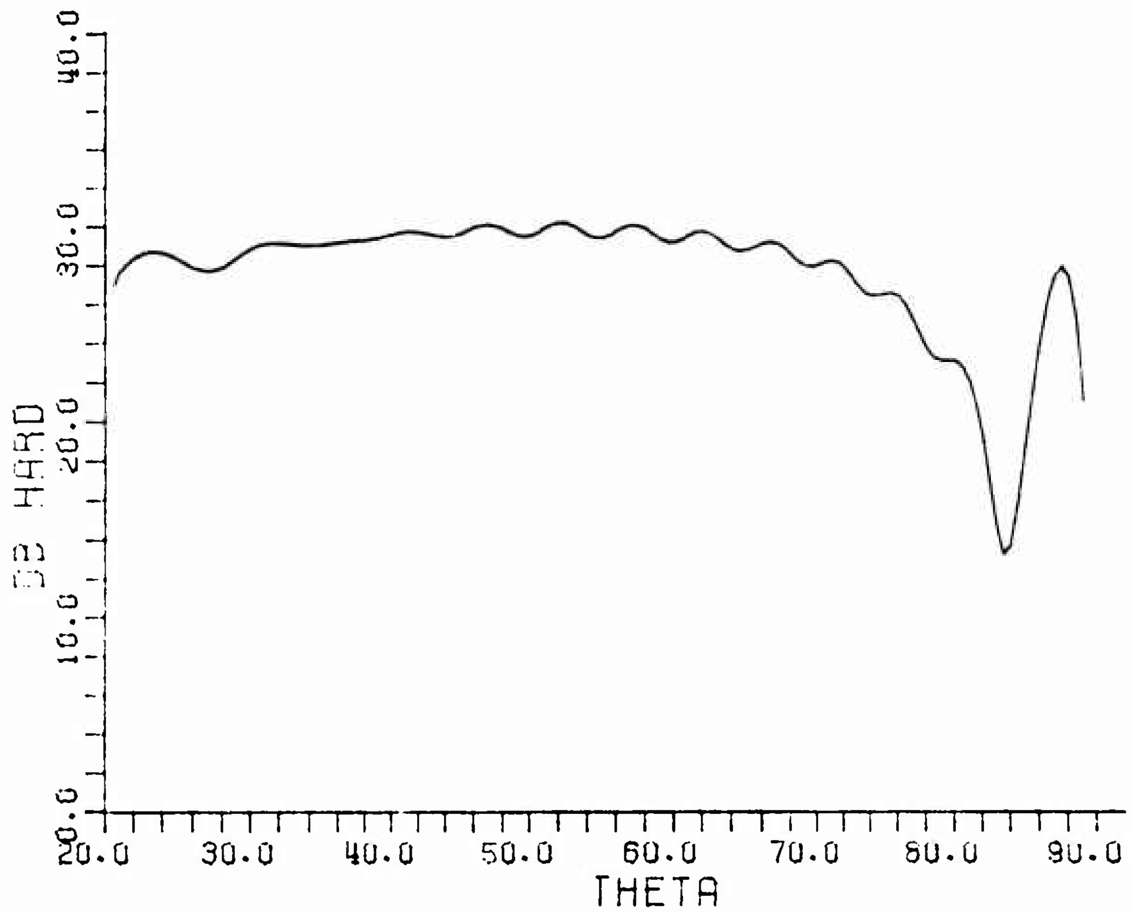

Fig. (31a). (σ_h/λ^2) in dB vs θ^i at f = 2 GHz, and ℓ = 1 m.

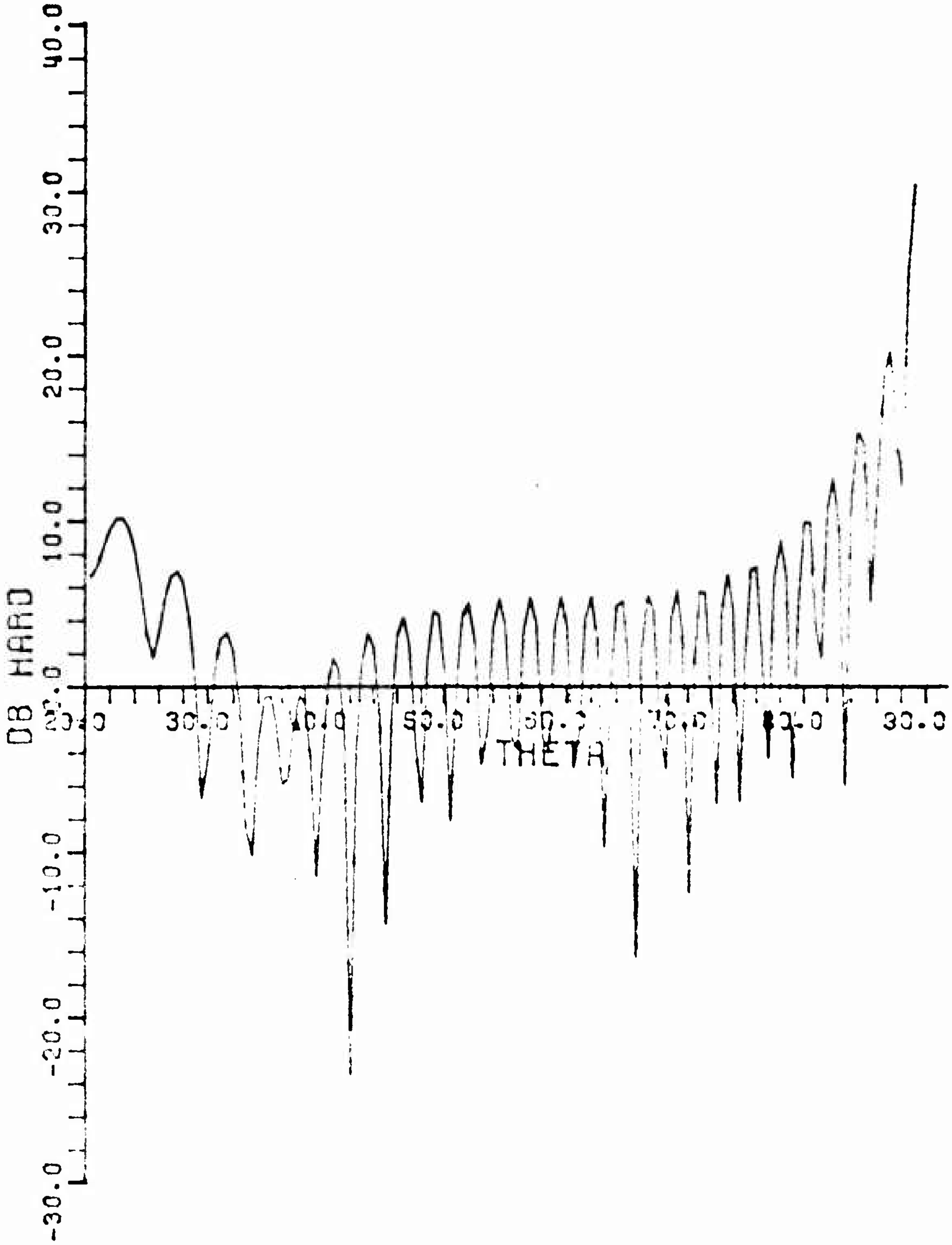

Fig. (31b). (σ_h/λ^2) in dB vs θ^i at f = 2 GHz,
and a = 1 m.

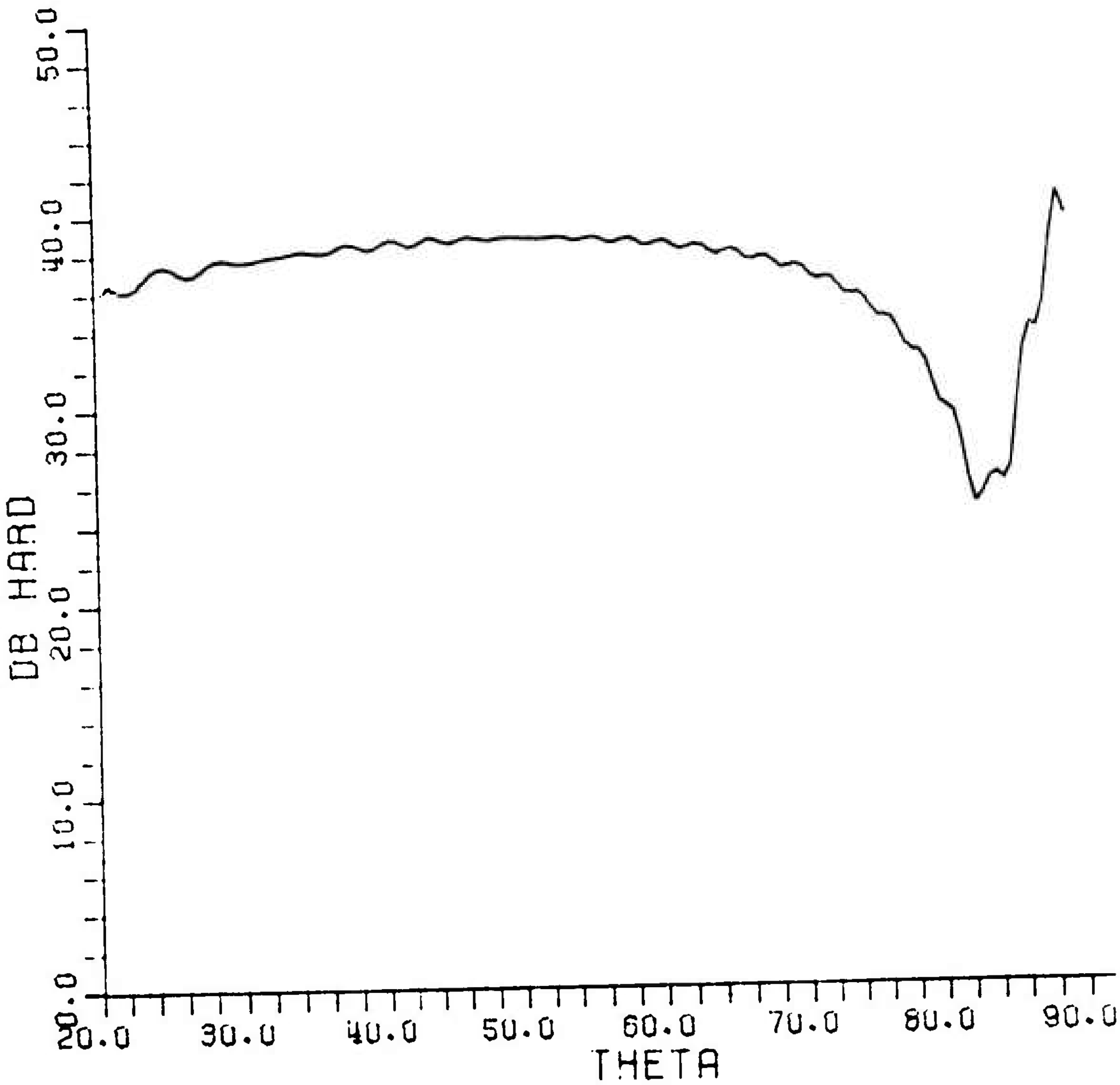

Fig. (32a). (σ_h/λ^2) in dB vs θ^i at f = 4 GHz, and ℓ = 1 m.

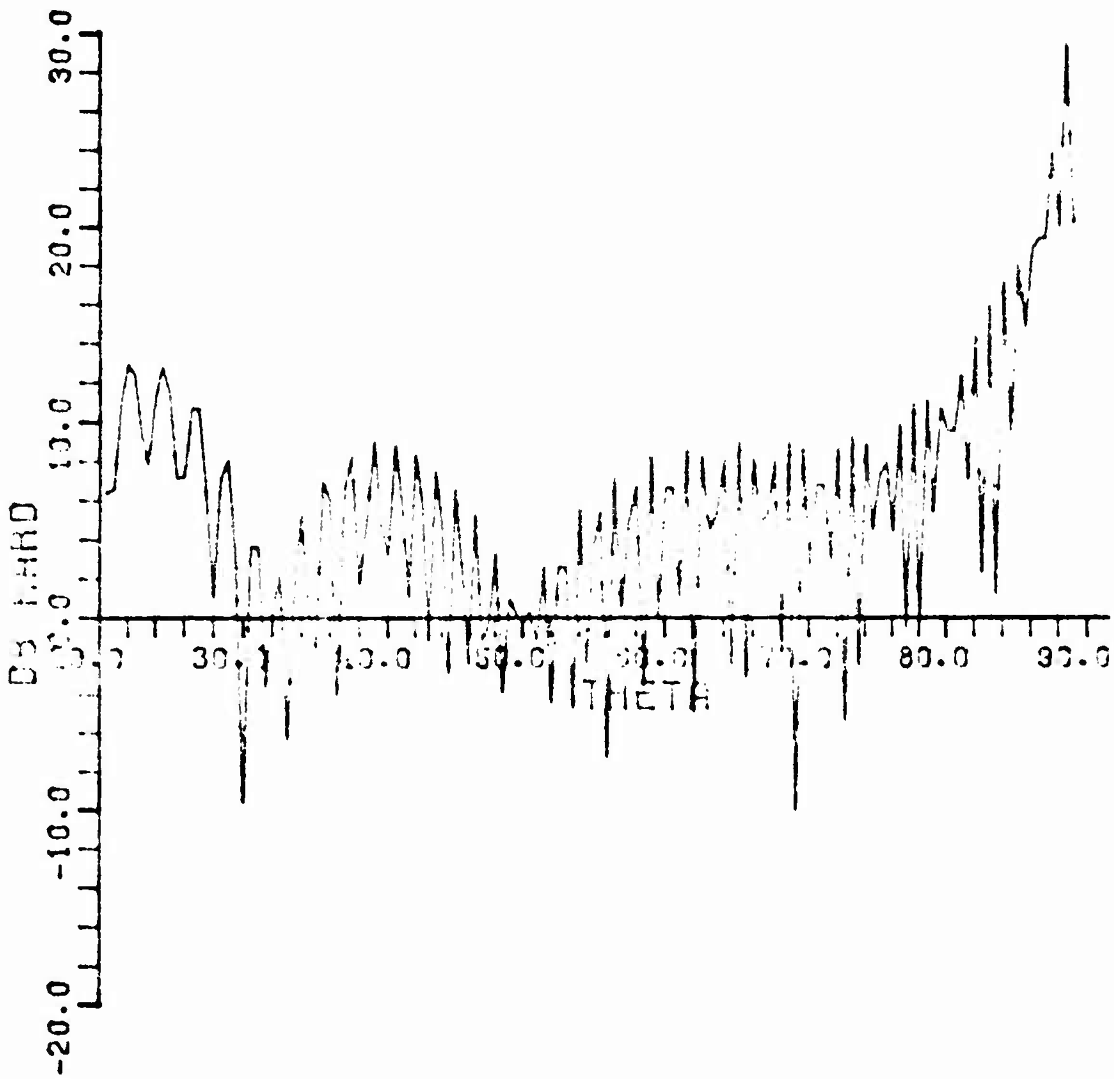

Fig. (32b). ($\tilde{\sigma}_h/\lambda^2$) in dB vs θ^i at f = 4 GHz, and ℓ = 1 m.

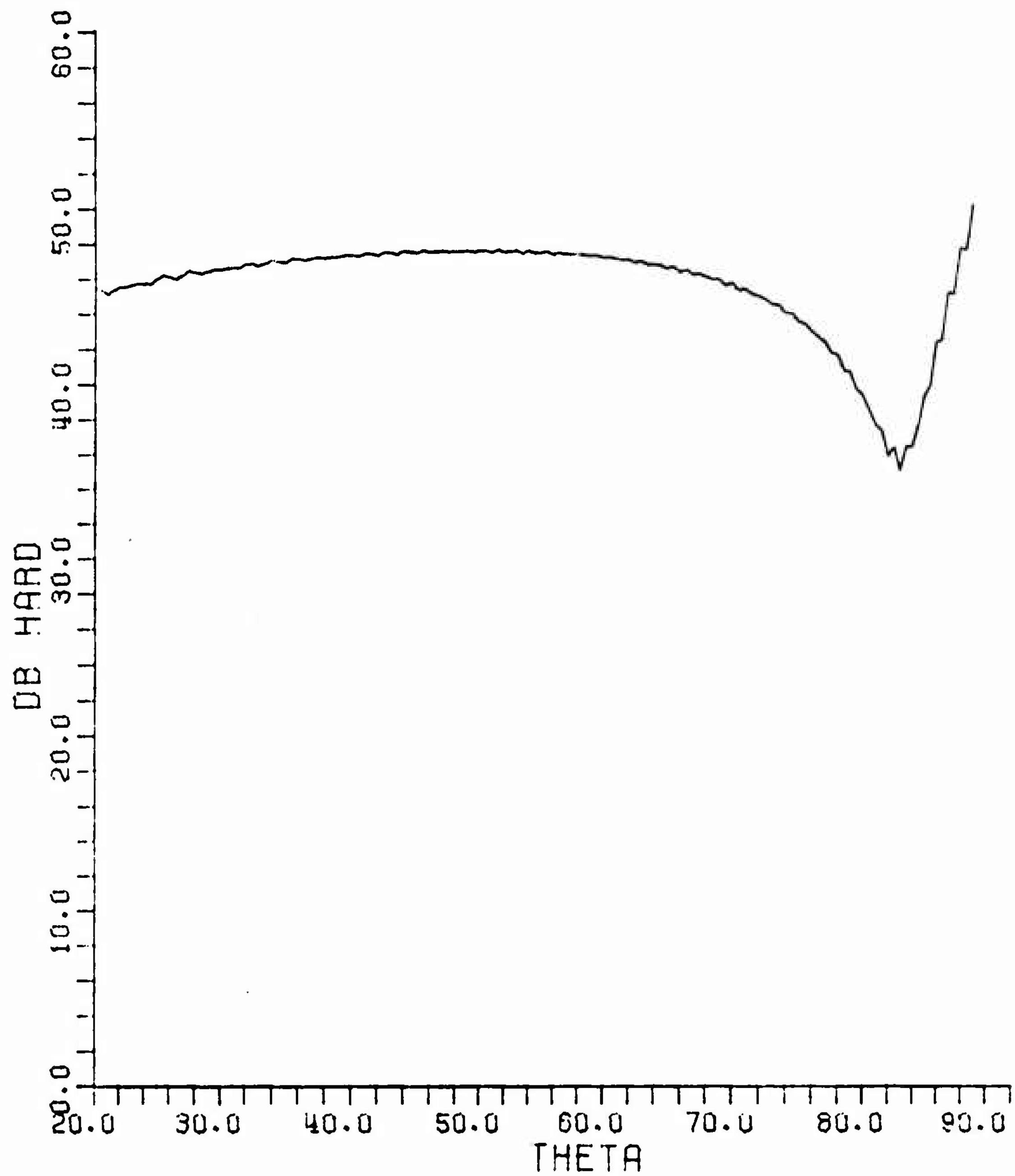

Fig. (33). (σ_h/λ^2) in dB vs θ^i at f = 8 GHz, and ℓ = 1 m.

IV. RECOMMENDATIONS FOR FUTURE WORK

It is seen from the present work that the RCS of the cylinder in Fig. 1 is strongly dependent on the surface impedance Z_s through its associated reflection coefficient. Consequently, it would be worth looking into the effects of a periodically modulated impedance surface rather than a planar impedance surface. The effect of the periodically modulated impedance surface may be taken into consideration via the Floquet solution for the scattering from such a surface (e.g., the Floquet solution for the sinusoidally modulated surface is available in the literature); the scattered field may be represented as a set of plane waves with different weightings, and different angles of incidence. The effects of each plane wave component of the scattered field upon the truncated cylinder may then be analyzed approximately via GTD. This analysis would of course be more difficult than the one performed in the present report; however, it does not appear to be intractable.

It is seen that the double reflection interaction (i.e., reflections between the surface impedance boundary and the cylinder of Fig. 1) together with the edge diffraction and surface reflection interactions illustrated in Figs. 2(a) and 2(b), respectively, provide the dominant contribution to the backscattered field. It would be worth looking into ways to control the backscattered field and hence the RCS due to these interactions by coating the cylinder with a lossy dielectric or an absorber; also, the diffraction from the top edges of the cylinder could be controlled by incorporating appropriately oriented slots in the neighborhood of this cylinder end cap edge. In order to deduce the diffraction coefficient for an edge with a thin dielectric coating, and with a slot in its immediate vicinity, a new canonical problem must be solved; however, such a problem may not be amenable to a simple analytical solution. But, one could resort to a hybrid GTD-moment method technique to numerically deduce the appropriate diffraction coefficient for different angles of incidence; while this numerical solution is also more complex than the one treated in the present report, it is still feasible.

REFERENCES

1. Felsen, L. B., and Marcuvitz, N.: Radiation and Scattering of Waves; Prentice-Hall, Inc., Englewood Cliffs, N.J., 1973 (see p. 554).

2. Keller, J. B.: "Geometrical Theory of Diffraction," J. Opt. Soc. Amer., vol. 52, pp. 116-130, 1962.

3. Kouyoumjian, R. G., and Pathak, P. H.: "A Uniform Geometrical Theory of Diffraction for an Edge in a Perfectly Conducting Surface," Proc. IEEE, vol. 62, pp. 1448-1461, Nov. 1974.

4. Crispin, J. W., Jr., and Maffett, A. L.: "Radar Cross Section Estimation for Simple Shapes," Proc. IEEE, vol. 53, pp. 833-848.